UNIVERSITY OF CALIFORNIA, MERCED

# Characterization of magnetic levitation with a microwave cavity

A Dissertation submitted in partial fulfillment of the
requirements for the degree of
Doctor of Philosophy

in
Physics

by
Nabin Kumar Raut
April 2022


Committee in charge:

Associate Prof. Chih-Chun Chien, Chair

Associate Prof. Michael Scheibner

Prof. Emeritus Raymond Chiao

The dissertation of Nabin Kumar Raut, titled ‘Characterization of magnetic levitation within a microwave cavity’, is approved, and it is acceptable in quality and form for publication.

Associate Prof. Jay E. Sharping, Advisor Date

Associate Prof. Chih-Chun Chien, Committee Chair Date

Associate Prof. Michael Scheibner, Committee Member Date

Prof. Emeritus Raymond Chiao, Committee Member Date

University of California, Merced
2022

# Dedicated to

This work is dedicated to my late father Birkha Raj Raut for your love, kindness, and hard work. To my mother Durga Maya Raut for all reasons in the world, brother Manoj Raut (Birali), and sisters Sarmila Raut and Sharada Raut for their adoration and support.

# Acknowledgments

Starts with my advisor Prof. Jay Sharping. I am grateful and humbled to you for your help, generosity, and patience. You gave me space in your lab in the most challenging time of my life. I appreciate the freedom in the research and the opportunity for exploration. Importantly, I want to thank you for grooming me over the years as a graduate student.

I also want to appreciate all the help I got from my co-advisor Raymond Chiao. Your enthusiasm always motivated me. Thank you goes to members of my dissertation committee Prof. Chih-Chun Chien and Prof. Michael Scheibner, for all suggestions, comments, and help.

I am thankful to all of my friends, especially Prabin, Yogesh, and Sam bhai, for their friendship. Yogesh and Prabin, we came same time here in Merced and went through highs and lows in the last six years. See together where we reached today. I enjoyed hiking this part of life trail with you two. Isn't the view breathtaking from here! Thank you goes to Deepak and Jiba dai for help settling in Merced. Shout out to Merced Nepali family for your love. The get-togethers, picnics, parties, celebrations, failebrations, and all that we have done together were the sweet memories, thank you.

In the top list of my acknowledgments are my lab mates Jeffery Miller, Jake Pate, Luis Martinez, Deepak Sapkota, Alisson Huff, Alessandro Castelli, and all for all you help and support. Jake, thank you for helping me learn the operation of dilution refrigerators and SRF instruments. I appreciate your guidance, collaboration, and carrier advice, Luis. Especial thanks goes to my lab mate and colleague Jeff for anytime and anywhere support in and outside of the lab. Cheers to our collaboration on the projects! The acknowledge list will be incomplete without putting the name of my mentee Amanda Tan. Thank you for all your support, especially for your guidance during the toughest time here in Spring 2017.

Last but not least, my sincere appreciation goes to the United States of America for giving me a chance to find the best of myself. Importantly, the University of California Merced in that regard. Moreover, I want to remember graduate coordinate Amanda Sargent & Paul Roberts and Becky Mirza & Lacey Long-Vejar from the international office. Thank you, Prof. Linda Hirst, for waiving my application fee, without which I could not have applied here. All the clubs on the campus for their warm welcome.

**Nabin Kumar Raut**
Graduate student of Physics

School of Natural Sciences

University of California

5200 N. Lake Rd.

Merced, CA 95343

Tel: (209) 421-1653 *nraut@ucmerced.edu*

---

## EDUCATION

- **Ph.D.** Physics, University of California, Merced, advanced to candidacy
  Title: "Characterization of magnetic levitation within a microwave cavity"

  Advisor: Ass. Prof. Jay Sharping

- **M.Sc.** Physics, Central department of Physics, Nepal, July 2015
  Thesis: "Computational study of vibrational properties of different family of Quinone molecules"

  Advisor: Ass. Prof. Hari Prasad Lamichhane

- **B.Sc.** Physics, Tri-Chandra Multiple campus, Nepal, August 2010

## Professional service

Referee for: (a) Optics and Laser Technology, Elsevier.

(b) ASC2020 Special Issue of the IEEE Transactions on Applied Superconductivity.

## Publication list

1. **Nabin Raut**, Jeffery Miller, Raymond Chaio, Jay Sharping. *Magnet strength dependence of levitated magnets within a microwave cavity*. IEEE Transactions on Instrumentation and Measurement-In Review.
2. **Nabin Raut**, Jeffery Miller, Jacob Pate, Raymond Chaio, Jay Sharping. *Field-cooled magnetic levitation of a neodymium magnet within a superconducting radio frequency cavity*. IEEE Transactions on Applied Superconductivity, January 16, 2021.
3. **Nabin K. Raut**, Jeffery Miller, Jay E. Sharping. *Progress in optoelectronic oscillator*. Journal of Institute of Science and Technology, 24 (1): 26-33, 2019
4. **Nabin K. Raut**, Hari P. Lamichhane. *Sequential substitution of methyl side group in naphthoquinone and anthraquinone to investigate sensitivity of the carbonyl band*. Journal of Institute of science and technology, 22 (1): 137-146, 2017

5. **Nabin K. Raut**, Hari P. Lamichhane. *Effect of additional side groups on the vibrational frequencies of benzoquinone molecules*. Bibechana, 14: 66-76, 2017

**Presentations**

- Oral presentation: **Nabin Raut**, Jeffery Miller, Harrold Hart, Raymond Chaio, Jay Sharping. *Controlled Meissner Levitation*. Applied Superconductivity Conference, October 23-28, 2022-Submitted.
- Oral presentation: **Nabin Raut**, Jeffery Miller, Raymond Chaio, Jay Sharping. *Characterization of magnetic levitation within a microwave cavity*. APS March Meeting, March 14-18, 2022
- Oral presentation: **Nabin Raut**, Jeffery Miller, Raymond Chaio, Jay Sharping. L*evitation of a neodymium magnet within a superconducting radio frequency cavity*. APS March Meeting, March 15-19, 2021
- Oral presentation: **Nabin Raut**, Jeffery Miller, Jacob Pate, Raymond Chaio, Jay Sharping. *Field-cooled magnetic levitation of a neodymium magnet within a superconducting radio frequency cavity*. Applied Superconductivity Conference, October 24- November 7, 2020
- Poster presentation: **Nabin Raut**, Jeffery Miller, Jacob Pate, Raymond Chaio, Jay Sharping. L*evitation of a neodymium magnet in a superconducting radio frequency cavity*. Research week 2020, March 2-6, UC Merced
- Oral presentation: Jeffery Miller, **Nabin Raut**, Jay Sharping. *Optoelectronic oscillator locked to a high-Q SRF cavity*. Applied Superconductivity Conference, Seattle, WA, Oct 31-Nov2, 2018
- Poster presentation: Jeffery Miller, **Nabin Raut**, Jay Sharping. *Optoelectric microwave oscillator*. APS annual far west meeting, UC MERCED, CA, November 3-4, 2017
- Oral presentation: **Nabin Raut**. *Effect of additional methyl groups on the carbonyl bands of naphthoquinone family*. 33$^{rd}$ convention of Nepal physical society, Nepal, 2016

**Fellowships/Awards**

- Graduate Dean's Dissertation Fellowship, University of California Merced, Spring 2022
- GradEXCEL Peer Mentors Fellowship, University of California Merced, 2021-2022
- GSA Travel Awards, Graduate Student Association, University of California Merced, 2021
- Physics Graduate Student Summer Fellowship, University of California Merced, 2018-2020

**Professional development**

- Programming experience in MATLAB, Python, COMSOL Multiphysics, LabVIEW, and LaTeX
- Machine shop training, University of California, Merced, December 19-21, 2016. The shop on campus is used for (>3 years) the new cavity design.

- Winter dissertation boot camp, Graduate division, University of California, Merced, January 7- 11, 2019
- Teaching Matters Series I (April 23, 2018), II (September 19, 2018), III (February 20 & 22, 2018)
- COMSOL Multiphysics Intensive Training (2 Days), June 19-20, 2018

**Teaching and mentoring experience**

- Physics Graduate Representative, Graduate Visitation Weekend Panel, February 25, 2022, University of California, Merced.
- Special Mentor, Initiatives for Girls in Physics (IGP), Nepal.
- Graduate Student Researcher, School of Natural Sciences, Spring & Summer 2021, University of California, Merced.
- Teaching assistant, Math 11 (Fall 2016, Spring 2017, Fall 2017, Fall 2018), Math 22 (Summer 2017, Fall 2019), Math 12 (Spring 2018), Math 21 (Spring 2019), Physics 18 (Spring 2020), Physics 19 (Fall 2020), University of California, Merced.
- Instructor, 2004-2006, Kantipur Academy, Dynamic Education Center, Biratnagar, Nepal.

Course: Calculus and Physics

- Instructor, 2006-2008, Multi-Training and Language Center, Dharan, Nepal.

Course: Mathematics

- Instructor, 2008-2009, Marvellous English Boarding School, Kathmandu, Nepal.

Course: Mathematics and Science

- Instructor, 2009-2012, Oxford Educational Center, Kathmandu, Nepal.

Course: Mathematics and Science

**Professional memberships**

- American Physical Society (APS)
- Association of Nepal Physicists in America (ANPA)
- BloodSource
- UNICEF

**REFERENCE**

*Available on request*

## Abstract

Levitating, controlling, and detecting the motion of mesoscopic objects is useful for inertial sensing and fundamental studies in quantum physics. We report the first experimental measurements of Meissner-effect levitation for a sequence of identical millimeter-scale neodymium magnets having varying strengths within a cm-scale superconducting aluminum coaxial quarter-wave stub cavity. We experimentally, theoretically, and analytically characterized Meissner-effect levitation within a 10 GHz superconducting aluminum coaxial quarter-wave stub cavity for a sequence of identically shaped millimeter-scale neodymium magnets having varying strengths (1.22-1.47 T). Magnet levitation within the cavity is accompanied by both gradual and abrupt shifts in the resonance frequency (with a height sensitivity as large as 400 MHz/mm) as well as changes in the total quality factor (8%-17%) as a function of temperature during the superconducting transition of the aluminum cavity. The experimental observation is confirmed with a cylindrical and spherical magnet. The controlled heating and cooling of the cavity show hysteresis in the frequency shift. Furthermore, the experimental observation has shown excellent agreement with finite element simulations, room temperature measurements, and a lumped element model.

# Contents

# List of Figures

# List of Tables

# List of Symbols

| Symbol | Meaning |
|---|---|
| $\epsilon_0$ | Absolute permittivity |
| $\mu_0$ | Absolute permeability |
| $T_C$ | Transition temperature of superconductor |
| $\chi$ | Magnetic susceptibility |
| $\omega$ | Angular frequency |
| $\vec{J}$ | dc current density |
| $\lambda_L$ | London penetration depth |
| $n_s$ | superconductor electron density |
| $\xi_0$ | Pippard coherence length |
| $2\Delta$ | Energy gap of superconductor |
| $\varepsilon_F$ | Fermi energy |
| $\omega_D$ | Debye frequency |
| $(k\uparrow, -k\downarrow)$ | State of a Cooper pair |
| $B_r$ | Remanence of a magnet |
| $\rho$ | Density |
| $L_0$ | Inductance of a bare cavity |
| $C_0$ | Capacitance of a bare cavity |
| $\vec{m}$ | Magnetic moment |

# Chapter 1
# Introduction

"*Do not judge me by my successes, judge me by how many times I fell down and got back up again*."-Nelson Mandela

A magnet placed above a superconductor induces supercurrent on the surface of the superconductor, screening the magnetic flux from its core [1]. This supercurrent produces an opposing magnetic field inside the superconductor which gives rise to a force called a diamagnetic force. When the strength of the diamagnetic force is large enough to balance the force due to gravity, the magnet will levitate above the superconductor. The phenomenon is called magnetic levitation.

The magnetic levitated system has been used for the development of the transportation system. For example, the levitated system is implemented in the high-speed train known as the bullet train and in the much-awaited transportation development called the hyperloop. The energy loss is low in such a freely floating system. There is no loss due to clamping and thermal contact. Moreover, the superconducting magnetic levitation further minimizes the losses. There are no losses, as in the optical levitation, due to photon recoil and heating in the superconducting magnetic levitation.

In this thesis, we have demonstrated, for the first time, magnetic levitation within a superconducting microwave cavity. The cavity is made from 6061 grade aluminum which is a type-I superconductor. The critical temperature of aluminum is 1.2 K. A permanent neodymium magnet is placed within the microwave cavity. When the entire cavity goes into the superconducting transition, the magnet is lifted from the surface of the superconductor due to the Meissner effect. Before discussing potential applications of our levitated system, the following paragraphs discuss why we choose the microwave cavity for magnetic levitation.

## I. Why Microwave Cavity?

A coaxial quarter wave microwave cavities can localize electric or magnetic fields in a small area (see Figure 1.1) [2--4]. The electric field is localized on the stub and the magnetic field on the bottom of the cavity. Such concentration of the energy in a small volume increases the mode volume of the cavity. This causes a reduction in energy dissipated due to the conductive and dielectric losses at surfaces and interfaces [5]. The quality factor (Q) of the cavity is the ratio of total energy it can store to its total losses. To have a high value of Q indicates a lower energy dissipation, meaning a photon recycles multiple times inside the cavity before dying out. Such a narrow mode of the cavity provides unique opportunities to couple other objects and systems [6,7]. For instance, cavities with higher values of Q are applied to detect rare gravitational wave events [8], dark matter detection [9--13], mechanical coupling, and perturbation [14]. A detailed discussion about microwave cavities is included in chapter 2.

The superconducting microwave cavities are fabricated from materials such as aluminum, niobium, etc. Cavities made up such materials go into the superconducting phase transition at the transition temperature. For example, the cavity we are using in our experiment goes into superconducting state at 1.2 K. Large numbers of Cooper pairs are formed during this phase change. The Cooper pairs are special pairs of electrons whose interaction is mediated by the phonon. They exhibit attractive interaction, thereby reducing the total energy of the system. The reduction of energy brings more stability in the system (see Chapter 3). The superconducting microwave cavities have about five orders of magnitude lower losses than normal conducting cavities [15].

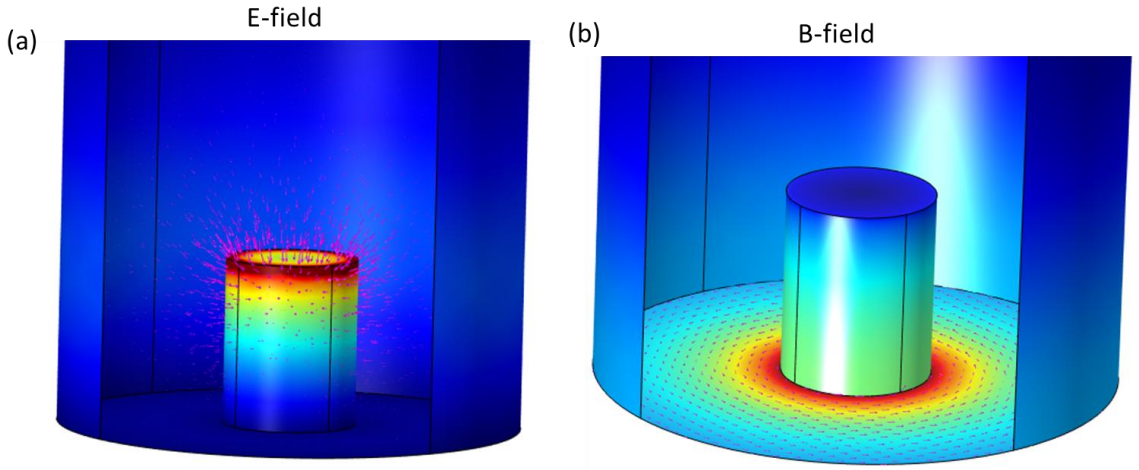


Figure 1.1: A coaxial quarter wave microwave cavity. (a) the electric field is localized around the rim of the stub, (b) the magnetic field stored on the bottom of the cavity.

## II. Applications of Microwave Cavities

### A. Cavity Optomechanics

One important application of such a high-Q cavity would be to couple it with another oscillator. The coupling here refers to the energy transfer between the two systems. This field of study is commonly known as cavity optomechanics. It studies the dynamics between two coupled harmonic oscillators: a cavity mode and a normal mechanical mode [16]. The field was studied early on theoretically by Braginsky in 1967 [17]. As shown in Figure 1.2, the circulating field inside the cavity with frequency $\omega$ and damping K generates high power. The enhancement in a photon's momentum can modify the dynamics of the mechanical element [18]. Depending upon the strength of the coupling, rich physics can be explored from semi-classical to novel physics.

Edward Mills Purcell, in 1940s, studied the effect of coupling between the two harmonic oscillators. He observed that the spontaneous emission rate of the quantum system can be enhanced linearly by the quality factor of the cavity. The effect is known as the Purcell effect [19]. Motional cooldown of the classical system to its ground state energy can be achieved with the strong coupling between the two systems. In the quantum mechanics, the least energy state with energy $\frac{1}{2}\hbar\omega$ is called the ground state energy. The ground state cooldown leads to the study of the macroscopic quantum mechanics. In the deep-strong

coupling regime the exchange of energy between the light and the matter is faster compared to their losses. Faster exchange of energy caused splitting in the energy level [14].

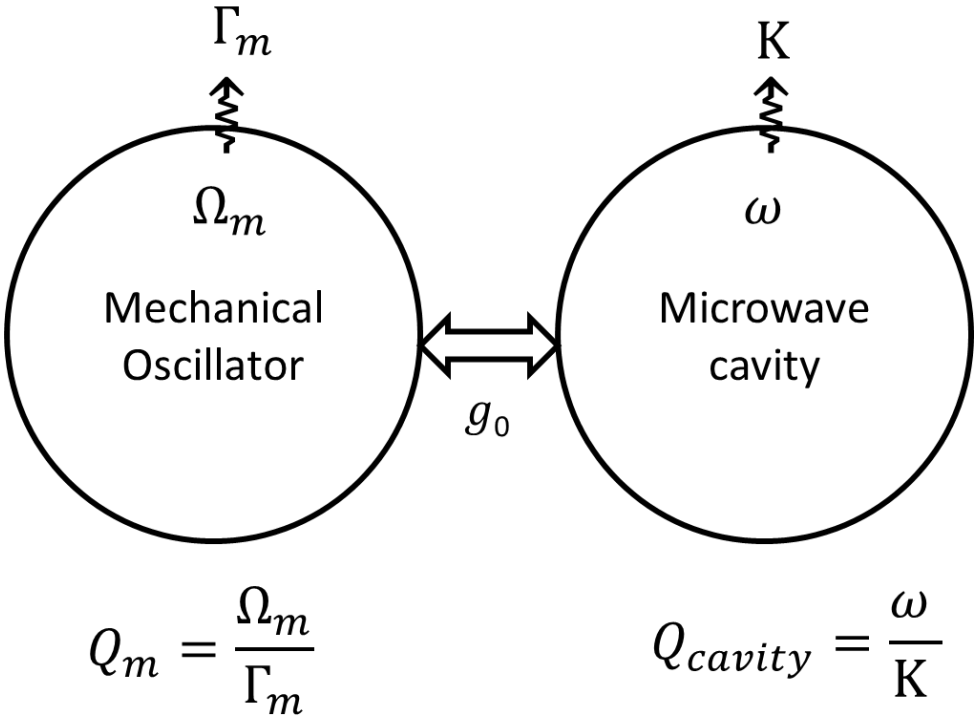


Figure 1.2: Schematic of a cavity optomechanical system. Here, a mechanical degree of freedom is coupled to the resonance mode of a microwave cavity. The strength of coupling between two systems is represented by $g_0$. The frequency and damping of the microwave cavity are $\omega$ and K, respectively. Similarly, the mechanical system has the frequency of $\Omega_m$ and the damping of $\Gamma_m$. The quality factor of the mechanical oscillator and the microwave cavity are denoted, respectively, by $Q_m$ and $Q_{cavity}$.

B. Quantum Memory

The superconducting microwave cavity is also used for the quantum memory. The cavity mode can be used for the control, store, and readout of the quantum states [20]. Figure 1.3 shows an example of a microwave cavity mode coupling with a qubit mode. When there is no coupling between the modes, the one mode's dynamics do not affect the other mode's dynamics. However, when the coupling between the modes is strong, the degeneracy in the qubit energy level lifts up. The amount of energy splitting depends directly on the strength of the coupling. Such splitting allows the excitation of the qubit to live for a longer time [21]. Here, dissipation of the qubit is recycled trough the cavity mode. Recently, a novel microwave photon counting technique for the detection of low mass bosonic dark matter candidate was developed by using a dispersively coupled superconducting cavity-qubit system [22].

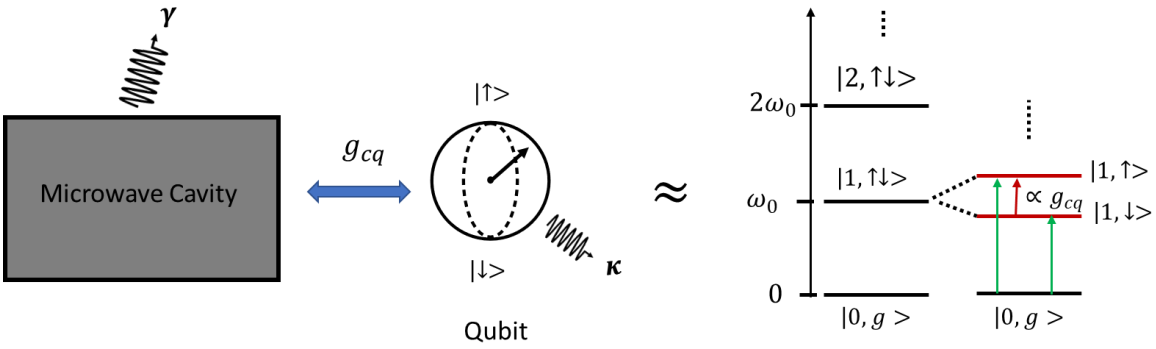


Figure 1.3: A high-Q microwave cavity is strongly coupled to a qubit. The strong coupling between the microwave mode and qubit mode results in energy splitting. Here, $\gamma$ and $\kappa$ are the microwave and qubit dissipations, respectively. $g_{cq}$ represents the coupling between the two modes.

### C. Recent Works

Furthermore, interesting results by coupling a mechanical system with the highly localized field of the cavity has been reported. An experimental demonstration of the Casimir spring effect within a superconducting reentrant microwave cavity system was published [23]. This cavity is similar to the cavity design we are using in our experiment. The difference being this cavity has a small gap between the stub and the open end of the cavity. Moreover, a strong coupling between a magnon with the highly concentrated RF magnetic field of a cavity has been demonstrated [24,25].

## III. Meissner Levitation

As discussed above, there are promising developments in coupling mechanical oscillators to the superconducting microwave cavity mode [26]. The common feature of all of those perturbations and couplings is they are somehow clamped and are in thermal contact with the other object. This introduces additional loss in the system. Levitated systems are free from those losses. There are significant developments in optical levitation. One main challenge in this type of levitation is the loss associated with the photon recoil and heating [27--29].

A promising alternative to optical levitation is to use passive levitation techniques involving magnets and superconductors. In the passive levitation, a magnet is levitated due to the Meissner effect. In this levitation, there are no losses due to clamping, thermal contact, and photon recoil. However, in this technique, it is important to distinguish between Type-I and Type-II superconductors. In the meantime, it is also important to distinguish whether the experiment is performed in a zero-field cooled, or non-zero-field cooled condition. When a Type-II superconductor is cooled below its critical temperature in the presence of a non-zero magnetic field, magnetic flux is trapped by vortices within the material. The trapped flux then freezes the motion of the magnet. In the non-zero-field

cooling condition, the Type-II superconductor is cooled in the absence of magnetic fields. The permanent magnet is then inserted after cooling.

In the recent research, magnetic levitation above a type-II superconductor has been realized as a novel mechanical transduction for the individual spin qubit in the nitrogen-vacancy center [31]. Furthermore, the Meissner has been proposed for the study of modified gravitational wave detection [32].

In comparison, when a Type-I material makes the superconducting transition, the superconductor exhibits a perfectly diamagnetic response as long as the magnetic field is less than some critical value. Supercurrents build up on the surface of the superconductor which fully screen the magnetic flux from its interior [30]. The Meissner-force is always repulsive and can be large enough to lift macroscopic objects to some equilibrium height where the net force of the interaction combined with that due to gravity is zero.

## IV. Meissner Levitation within the microwave cavity

This thesis is driven by the curiosity of developing a novel perturbation of a permanent magnet with the superconducting microwave cavity mode. Our novel cavity-magnet system could be used as a versatile research platform for tests of fundamental and new physics. First, such an electromechanical system may be useful as a means to couple the low-frequency mechanical motion of the magnet with other quantum objects, such as magnons and transmons, which are used for quantum information processing. The development of sensors based on levitated magnets within high-Q cavities is an interesting alternative for detecting gravitational waves and dark matter. Such a system can be used to prepare, control, store, and measure arbitrary quantum states. Finally, it may be possible to achieve strong coupling to and ground-state cooling of a mechanical resonator. The main goal of this thesis is to levitate and characterize permanent magnets within a microwave cavity successfully.

# Chapter 2

# Microwave Cavities

*"Live as if you were to die tomorrow, learn as if you were to live forever."*-Mahatma Gandi

In our research, a permanent magnet is levitated within a microwave cavity. This chapter starts with a brief analysis of the electromagnetic wave propagation modes within the cylindrical and circular waveguide. Furthermore, the discussion about the fundamental mode and quality factor of a coaxial quarter-wave cylindrical cavity is also presented in the chapter. Studies of modes of cavities in this chapter help identify the most sensitive region in our magnetic levitation experiment.

## 2.1 Cylindrical Cavity

A cylindrical cavity supports a different mode of propagation of the electromagnetic wave (em). A simplified sketch of the cylindrical cavity is shown in Figure 2.1. Here, Maxwell's equations are solved to get the transverse components of the electric and magnetic fields. Those components are then used to calculate the transverse electric (TE) and transverse magnetic (TM) mode of propagation. The derivation in this section is adapted from the Microwave engineering book by David Pozar [33].

Let us consider time-harmonic field with an $e^{i\omega t}$ dependent and an electromagnetic field propagating along the $z$-direction. The general equations for an electric field and a magnetic field in that direction are given by the relations:

$$\vec{\mathrm{E}}(x,y,z) = (\vec{e}(x,y) + \vec{z}e_z(x,y))e^{-i\beta z}, \tag{2.1}$$

$$\vec{\mathrm{H}}(x,y,z) = (\vec{h}(x,y) + \vec{z}h_z(x,y))e^{-i\beta z}, \tag{2.2}$$

Where, $\vec{e}(x,y)$ & $\vec{h}(x,y)$ represents transverse electric and magnetic field components, $e_z$ & $h_z$ represents longitudinal electric and magnetic field components, and $\beta$ is propagation constant. Now, Maxwell's equations in the source-free region ($\Delta \cdot \mathrm{E} = 0$) can be written as:

$$\Delta \times \vec{\mathrm{E}} = -i\omega\mu\vec{\mathrm{H}}, \tag{2.3}$$

$$\Delta \times \vec{\mathrm{H}} = i\omega\epsilon\vec{\mathrm{E}}, \tag{2.4}$$

Solving the above four equations will give components of the electric and magnetic field along $x$- and $y$- direction, which is given by the equations:

$$\vec{\mathrm{H}}_x = \frac{i}{k_c^2}\left(\omega\epsilon\frac{\partial\vec{\mathrm{E}}_z}{\partial y} - \beta\frac{\partial\vec{\mathrm{H}}_z}{\partial x}\right), \tag{2.5}$$

$$\vec{\mathrm{H}}_y = \frac{-i}{k_c^2}\left(\omega\epsilon\frac{\partial\vec{\mathrm{E}}_z}{\partial x} + \beta\frac{\partial\vec{\mathrm{H}}_z}{\partial y}\right), \tag{2.6}$$

$$\vec{\mathrm{E}}_x = \frac{-i}{k_c^2}\left(\beta\frac{\partial\vec{\mathrm{E}}_z}{\partial x} + \omega\mu\frac{\partial\vec{\mathrm{H}}_z}{\partial y}\right), \tag{2.7}$$

$$\vec{\mathrm{E}}_y = \frac{i}{k_c^2}\left(-\beta\frac{\partial\vec{\mathrm{E}}_z}{\partial y} + \omega\mu\frac{\partial\vec{\mathrm{H}}_z}{\partial x}\right), \tag{2.8}$$

Here, $k_c^2 = k^2 - \beta^2$=cutoff wavenumber, $k = \omega\sqrt{\mu\epsilon} = \frac{2\pi}{\lambda}$ = wavenumber of the material filling in the resonator region.

I. Cutoff frequency:

The cutoff frequency is the frequency beyond which there will be no wave propagation. The frequency is given by the relation $f_{mnl} = \frac{\omega_c}{2\pi} = \frac{k_c c}{2\pi} = \frac{k_c}{2\pi\sqrt{\mu\epsilon}}$. It depends on the cut-off wavenumber and the nature of the filling material.

II. Power flows down in the resonator:

It is important to know about the energy storage capacity of the resonator. The total power flow inside the volume of the resonator towards z-direction is given by:

$$P_0 = \frac{1}{2}Re\oiint S.\hat{n}ds$$

$S$ =poynting vector= $\vec{\mathrm{E}} \times \vec{\mathrm{H}}^*$

Here, the integration is taken across the surface of the resonator.

III. Power lost on the surface of the resonator:

There are mainly two types of losses in the resonator: dielectric and conducting loss. The former loss can be address by making permittivity ($\epsilon$) complex by including loss tangent ($tan\delta$) of the material. Whereas the conducting loss can be calculated by using the perturbation method. The power lost per unit length of a resonator can be calculated as:

$$P_{loss(l)} = \frac{R_s}{2}\oint |\vec{\boldsymbol{J}}_s|^2 dl$$

Where, $R_s = \sqrt{\frac{\omega\mu_0}{2\sigma}}$=Surface resistivity of conducting wall

$\sigma$ = Surface conductivity of conducting surface

Equations (2.5)-(2.8) are useful in finding the different modes of propagations within the cylindrical cavity. In sections 2.1.1 and 2.1.2, those equations will be used to calculate the TE and TM propagation mode within the cylindrical cavity.

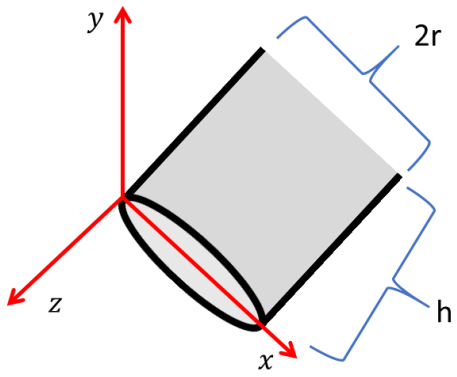


Figure 2.1: Sketch of a cylindrical waveguide. The waveguide has a radius of $r$ and a height of $h$.

### 2.1.1 Transverse Electrical (TE) Waves

In the TE wave, an electrical field will be zero along with the propagation of the electromagnetic wave ($\vec{E}_z = 0$). However, a magnetic field will be non-zero ($\vec{H}_z \neq 0$). In this case, equations (2.5)-(2.8) can be re-written as:

$$\vec{H}_x = -\frac{i\beta}{k_c^2}\frac{\partial \vec{H}_z}{\partial x}, \tag{2.9}$$

$$\vec{H}_y = -\frac{i\beta}{k_c^2}\frac{\partial \vec{H}_z}{\partial y}, \tag{2.10}$$

$$\vec{E}_x = -\frac{i\omega\mu}{k_c^2}\frac{\partial \vec{H}_z}{\partial y}, \tag{2.11}$$

$$\vec{E}_y = \frac{i\omega\mu}{k_c^2}\frac{\partial \vec{H}_z}{\partial x}, \tag{2.12}$$

Using Helmholtz wave equation for the magnetic field in the z-direction ($\vec{H}_z$) $\left[\left(\frac{\partial^2}{\partial x^2}+\frac{\partial^2}{\partial y^2}+\frac{\partial^2}{\partial z^2}\right)\vec{H}_z = 0\right]$ and putting the value of $\vec{H}_z$ results,

$$\left(\frac{\partial^2}{\partial x^2}+\frac{\partial^2}{\partial y^2}+k_c^2\right)h_z(x,y) = 0, \tag{2.13}$$

By using boundary conditions, $\vec{E}_t = 0$ and $\vec{H}_n = 0$ and the geometry of the cylindrical cavity shown in Figure 2.1, equation (13) can be used to solve to get $H_z$. Using similar steps, the resonant frequency of $TE_{nml}$ mode of the coaxial cylindrical cavity is calculated as $f_{mnl} = \frac{c}{2\pi\sqrt{\mu_r\epsilon_r}}\sqrt{(\frac{p_{mn}}{r})^2 + (\frac{l\pi}{h})^2}$, where $r$ is the radius, $h$ is the height of the cylinder and $p_{mn}$=$n^{th}$ root of Bessel function of first kind $J_m(k_c\rho)$. The dominant TE mode for the cylindrical cavity is the $TE_{111}$ mode. Although the $TE_{111}$ mode is the lowest and dominant mode, the $TE_{011}$ the mode has significantly higher Q. The reason is that it confines the field inside the cavity volume by avoiding losses introduced by seems and boundaries [33].

### 2.1.2 Transverse Magnetic (TM) Waves

For the case of the TM mode, there is no propagation of the magnetic field along with the direction of the propagation of the em wave. That means $\vec{\mathrm{H}}_z = 0$ and $\vec{\mathrm{E}}_z \neq 0$. Hence, equations (2.5)-(2.8) can be re-written as:

$$\vec{\mathrm{H}}_x = \frac{i\omega\epsilon}{k_c^2}\frac{\partial \vec{E}_z}{\partial y}, \tag{2.14}$$

$$\vec{\mathrm{H}}_y = -\frac{i\omega\epsilon}{k_c^2}\frac{\partial \vec{E}_z}{\partial x}, \tag{2.15}$$

$$\vec{\mathrm{E}}_x = -\frac{i\beta}{k_c^2}\frac{\partial \vec{E}_z}{\partial x}, \tag{2.16}$$

$$\vec{\mathrm{E}}_y = -\frac{i\beta}{k_c^2}\frac{\partial \vec{E}_z}{\partial y}, \tag{2.17}$$

Using Helmholtz wave equation for the electric field in the z-direction ($\vec{\mathrm{E}}_z$) $\left[\left(\frac{\partial^2}{\partial x^2}+\frac{\partial^2}{\partial y^2}+\frac{\partial^2}{\partial z^2}\right)\vec{\mathrm{E}}_z = 0\right]$ and putting the value of $\vec{\mathrm{E}}_z$ gives,

$$\left(\frac{\partial^2}{\partial x^2}+\frac{\partial^2}{\partial y^2}+k_c^2\right)e_z(x,y) = 0, \tag{2.18}$$

The geometry of the cavity determines similar boundary conditions, and steps can be taken as in the case of the TE mode to get more information about the mode.

## 2.2 Circular Waveguide

In this section, the discussion is about a hollow circular waveguide. This type of hollow waveguide also supports the different modes of propagation (TE & TM) that are discussed in the above section. For simplicity, the cylindrical coordinates are implemented for the analysis of this waveguide. Here, $\rho, \emptyset, z$ represents, respectively, radial, azimuthal, and axial coordinate of the waveguide. The equations (2.5)- (2.8) can be written in the cylindrical coordinates as:

$$\vec{\mathrm{H}}_\rho = \frac{i}{k_c^2}\left(\frac{\omega\epsilon}{\rho}\frac{\partial \vec{\mathrm{E}}_z}{\partial \emptyset} - \beta\frac{\partial \vec{\mathrm{H}}_z}{\partial \rho}\right), \tag{2.19}$$

$$\vec{\mathrm{H}}_\emptyset = \frac{-i}{k_c^2}\left(\omega\epsilon\frac{\partial \vec{\mathrm{E}}_z}{\partial \rho} + \frac{\beta}{\rho}\frac{\partial \vec{\mathrm{H}}_z}{\partial \emptyset}\right), \tag{2.20}$$

$$\vec{\mathrm{E}}_\rho = \frac{-i}{k_c^2}\left(\beta\frac{\partial \vec{\mathrm{E}}_z}{\partial \rho} + \frac{\omega\mu}{\rho}\frac{\partial \vec{\mathrm{H}}_z}{\partial \emptyset}\right), \tag{2.21}$$

$$\vec{\mathrm{E}}_\emptyset = \frac{i}{k_c^2}\left(-\frac{\beta}{\rho}\frac{\partial \vec{\mathrm{E}}_z}{\partial \emptyset} + \omega\mu\frac{\partial \vec{\mathrm{H}}_z}{\partial \rho}\right), \tag{2.22}$$

### 2.2.1 TE Mode

For the TE mode, the longitudinal component of the electric field is zero ($\vec{\mathrm{E}}_z = 0$). In this mode, $\vec{\mathrm{H}}_z \neq 0$. The $\vec{\mathrm{H}}_z$ component will be used to solve the wave equation. The transverse

components of the electric and the magnetic fields are given by (the detail derivation is skipped here, see Ref. [33] for the detail):

$$h_z(\rho, \emptyset) = [Asin(n\emptyset) + Bcos(n\emptyset))]J_n(\kappa_c \rho) \quad (2.22)$$

$$E_\emptyset(\rho, \emptyset, z) = [Asin(n\emptyset) + Bcos(n\emptyset))]J_n{}'(\kappa_c \rho) \quad (2.23)$$

Where, $A$ & $B$ are constants, ${\kappa_c}^2 = \kappa^2 - \beta^2$ is the cut off wave number, $n$ is an integer, $J_n(K_c\rho)$ is Bessel function of the first kind, $J_n{}'(\kappa_c\rho)$ is the derivative of $J_n$ with respect to its argument.

For the TE mode $\vec{\mathrm{E}}_z = 0$, which means $E_\emptyset(\rho, \emptyset) = 0$ at $\rho = a$ (radius of the waveguide).This gives $J_n{}'(\kappa_c a) = 0$. If we suppose $P_{nm}{}'$ as roots of $J_n{}'(x)$ so that $J_n{}'(P_{nm}{}') = 0$, where $P_{nm}{}'$ is the $m^{\text{th}}$ root of the $J_n{}'$, then $\kappa_{c_{nm}} = \frac{P_{nm}{}'}{a}$. For example, the value of the $P_{nm}{}'$ for $n = 0$ and $m = 1$ is 3.832. Furthermore, the $TE_{nm}$ is then defined by the cut off wavenumber $\kappa_{c_{nm}} = \frac{P_{nm}{}'}{a}$, where $n$ represents the number of the circumferential ($\emptyset$) variation and $m$ represents the number of the radial ($\rho$) variations. Hence, the propagation constant of this mode is:

$$\beta_{nm} = \sqrt{\kappa^2 - {\kappa_c}^2} = \sqrt{(\frac{2\pi}{\lambda})^2 - (\frac{P_{nm}{}'}{a})^2} \quad (2.24)$$

And the cut off frequency is:

$$f_{nm} = \frac{\kappa_c}{2\pi\sqrt{\mu\epsilon}} = \frac{P_{nm}{}'}{2\pi a\sqrt{\mu\epsilon}} \quad (2.25)$$

### 2.2.2 TM Mode

In the TM mode, the z-component of the electric field is used to solve the wave equation. The detail calculation is skipped here. In this mode, the solution of the electric field can be expressed as:

$$e_z(\rho, \emptyset) = [Asin(n\emptyset) + Bcos(n\emptyset))]J_n(\kappa_c \rho) \quad (2.26)$$

Using the boundary condition, $E_z(\rho, \emptyset) = 0$ at $\rho = a$, we get $J_n(\kappa_c a) = 0$. This condition results in $\kappa_c = \frac{P_{nm}}{a}$, where $P_{nm}$ is the $m$th root of the $J_n(x)$ such that $J_n(P_{nm}) = 0$.

The propagation constant of the $TM_{nm}$is:

$$\beta_{nm} = \sqrt{\kappa^2 - {\kappa_c}^2} = \sqrt{(\frac{2\pi}{\lambda})^2 - (\frac{P_{nm}}{a})^2} \quad (2.27)$$

And the cut off frequency is:

$$f_{nm} = \frac{\kappa_c}{2\pi\sqrt{\mu\epsilon}} = \frac{P_{nm}}{2\pi a\sqrt{\mu\epsilon}} \quad (2.28)$$

The first $TM_{nm}$ mode to propagate in the circular waveguide is $TM_{01}$ with $P_{01} = 2.405$. Similarly, the lowest $TE_{nm}$ mode to propagate in the circular waveguide is $TE_{11}$ because ${P_{11}}'(= 1.841)$ has least value among the roots of the Bessel function for the mode. In the circular wave, the $TE_{11}$ mode is the dominant mode than the $TM_{01}$ because ${P_{11}}' < P_{01}$. Moreover, since $m \geq 1$, there will be no $TM_{10}$ mode.

## 2.3 Coaxial Quarter-Wave Cavity

The cavity configuration used in our study is a coaxial quarter-wave cylindrical cavity shown in Figure 2.2 (a). The cavity consists of a coaxial section and a cylindrical section. The outer cylinder of the cavity has a dimension of 7 mm of a radius and 55 mm of height. In the coaxial region, a stub of 2 mm radius, and 5 mm of a height is shorted with the one end of the cylinder. The other end of the stub is vacuum terminated in the cylindrical region [3]. The electromagnetic field is confined in the coaxial section. It decays exponentially along the axis of the cylindrical section as a function of the distance from the stub towards the open end of the cavity. The cylindrical section of the cavity is long enough to prevent leakage of the field.

### 2.3.1 Fundamental Mode

The exact analytical solution of this type of cavity is not known. The finite element calculations are done in COMSOL using Electromagnetic, frequency domain (emw) physics [34]. In these calculations, eigenfrequency is studied by solving wave equation, $\Delta \times \frac{\Delta \times E}{\mu_r} = {k_0}^2 \left(\epsilon_r - \frac{j\sigma}{\omega\epsilon_0}\right) E$, to find resonance frequency of the cavity and their associated eigenmode in the resonant cavity, where $\mu_r$ is relative permeability, $\epsilon_r$ relative permittivity, $k_0$ wave number ($\frac{2\pi}{\lambda_0}$), and $\sigma$ is conductivity of the material [35].

In the fundamental mode of the cavity electric field is highly localized around the tip of the stub (Figure 2.2 (a) and (b)). This non-Maxwellian mode can be approximated as $E_r \propto (E_0 e^{\beta r} + {E_0}' e^{-\beta z},\ r < r_{stub},\ \&\ \frac{E_0}{r}\cos(k_0 r),\ r \geq r_{stub})$, here $r$ is the radial distance and $r_{stub}$ is the radius of the stub [36,37]. Similarly, the axial electric field exponentially decays from the stub towards the open end of the cavity as $E_z \propto E_0\, e^{i(\omega t - kz)}$ [38]. Figure 2.2 (c) and (d) show COMSOL simulations of the radial and the vertical distribution of the electrical field. Most of the electric field of the cavity is concentrated in the region $1.5\ mm < x < 2.5\ mm$ & $0\ mm \leq z < 1\ mm$. The electric field can further be confined around the stub by changing its shape to the conical. Due to this unique feature, any external

perturbation in this region of the cavity results in a significant shift in the resonance frequency.

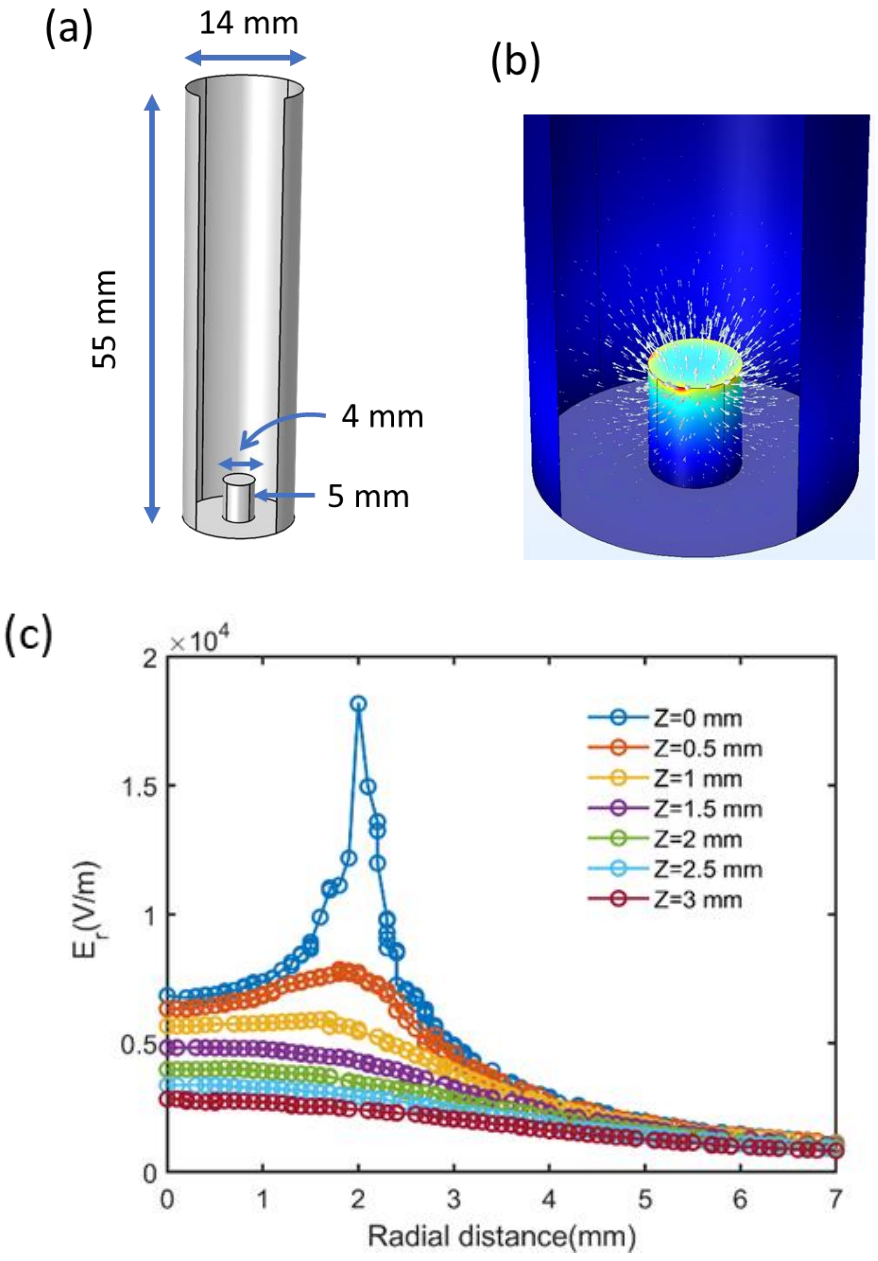

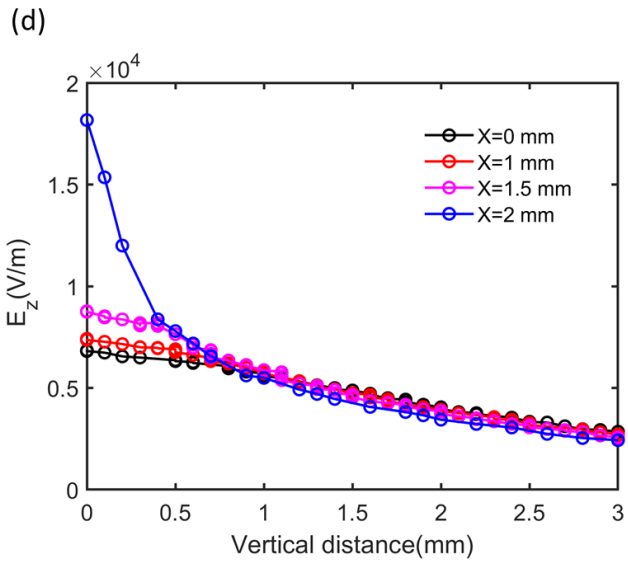


Figure 2.2: (a) Cavity configuration, (b) the electric field distribution within the cavity, (c) radial electric field is calculated at a different height from the stub, (d) axial electric field at different radial positions on the stub.

### 2.3.2 Quality Factor

The quality factor of a cavity can be expressed as $Q = 2\pi f \frac{Total\ enrgy\ stored\ (U)}{Power\ dissipation\ per\ cycle(W)}$ [39]. The higher value of Q means, the better the cavity for the energy storage. The intrinsic quality factor ($Q_{int}$) is quantified by the energy storage capacity of the cavity only. It does not include the effect of any external load on the system. For an under-coupled cavity, the losses in the cavity mode are mainly due to the losses in the surface screening currents, which expel the magnetic field from the bulk of the superconducting material. The intrinsic quality factor of the can be expressed as $Q_{int} = \frac{G}{R_s}$. Here, $G$ is the geometric factor, and $R_s$ is the surface resistance of the cavity.

The geometric factor (G-factor) only depends upon the mode of the cavity. It does not depend on the material of the cavity. It is calculated by finding the ratio of the magnetic field on the volume to the surface of the cavity and is expressed in the equation below [40]:

$$G = \frac{2\pi f \mu_0 \int_V |H|^2 dV}{\int_S |H|^2 dS} \tag{2.29}$$

Where $f$ is the frequency of the cavity, and $\mu_0$ is vacuum permeability. The G-factor for an empty cavity is found to be 110 Ω [41].

In this chapter, we learned about the mode of propagation of the electromagnetic wave in the different microwave cavity designs. In the next chapter, the discussion will be on the superconductor.

# Chapter 3

# Superconductor

"*Man is made by his belief. As he believes, so he is*."-Bhagavad Gita

Our experiment involves using cavity machined from 6061 Aluminum, which is a Type I superconductor. This chapter discusses different aspects of the superconductor. It includes the superconductor characteristics. In the penetration depth section, the London penetration depth will be derived and compared with the Pippard coherence length. Furthermore, Ginzburg-Landau's theory and types of superconductors will also be discussed. Finally, the BCS theory will be discussed in brief. Here, the ground state energy and the energy gap of the superconductor will be derived. The macroscopic and microscopic study of the superconductor makes a basis for our experiment on cavity cooling below superconducting transition without and with a magnet.

## 3.1. Characteristics of Superconductor

Superconductivity was discovered in 1911 by H. Kamerlingh Onnes [42]. The main finding of his observation was that many metals (like mercury, lid, and tin) phase transition into the zero-resistivity state below the transition temperature ($T_C$). This state is called the superconducting state. The phase transition temperature ($T_C$) is unique with the material. Table 3.1 lists some superconductors in the ascending order of the $T_C$. Among the material listed in table 1, aluminum has the least $T_C$ of 1.2 K, whereas YBCO becomes a superconductor at 92 K. Similarly, for each superconductor there is a unique limit of the amount of the external magnetic field it can let in. For example, aluminum has a maximum of 100 gauss limit of the external field.

Table 3.1: List of selected superconducting elements and compounds. The superconductors are listed in the ascending order of their transition temperature.

| Material (Type) | $T_C$(K) | $H_C$(T) |
|---|---|---|
| Al (I) | 1.2 | 0.01 |
| Sn (I) | 3.7 | 0.03 |
| Hg (I) | 4.1 | 0.04 |
| Pb (I) | 7.2 | 0.08 |
| Nb (II) | 9.3 | 0.82 |
| NbTi (II) | 10 | 15 |
| YBCO (II) | 92 | 120-150 |

A superconductor can be characterized as the perfect conductor (or zero resistivity). However, this description will be insufficient to describe all superconductors. The second fundamental characteristic of superconductivity is the perfect diamagnetism discovered by Meissner and Ochsenfeld in 1933 [43]. In this state, the superconductor excludes the external magnetic field completely from its interior. This phenomenon is called the Meissner effect [44]. A detailed discussion about the Meissner effect will be in the coming

sections. In the diamagnetic state, the magnetic susceptibility ($\chi$) of the material is equal to -1. Hence, $B = \mu_0 H(1+\chi) = \mu_0(H+M)$ becomes 0. In conclusion, no magnetic field is present within the interior of a diamagnetic material because the magnetization (M) opposes the magnetic field (H) by canceling it. This is the basis for magnetic levitation.

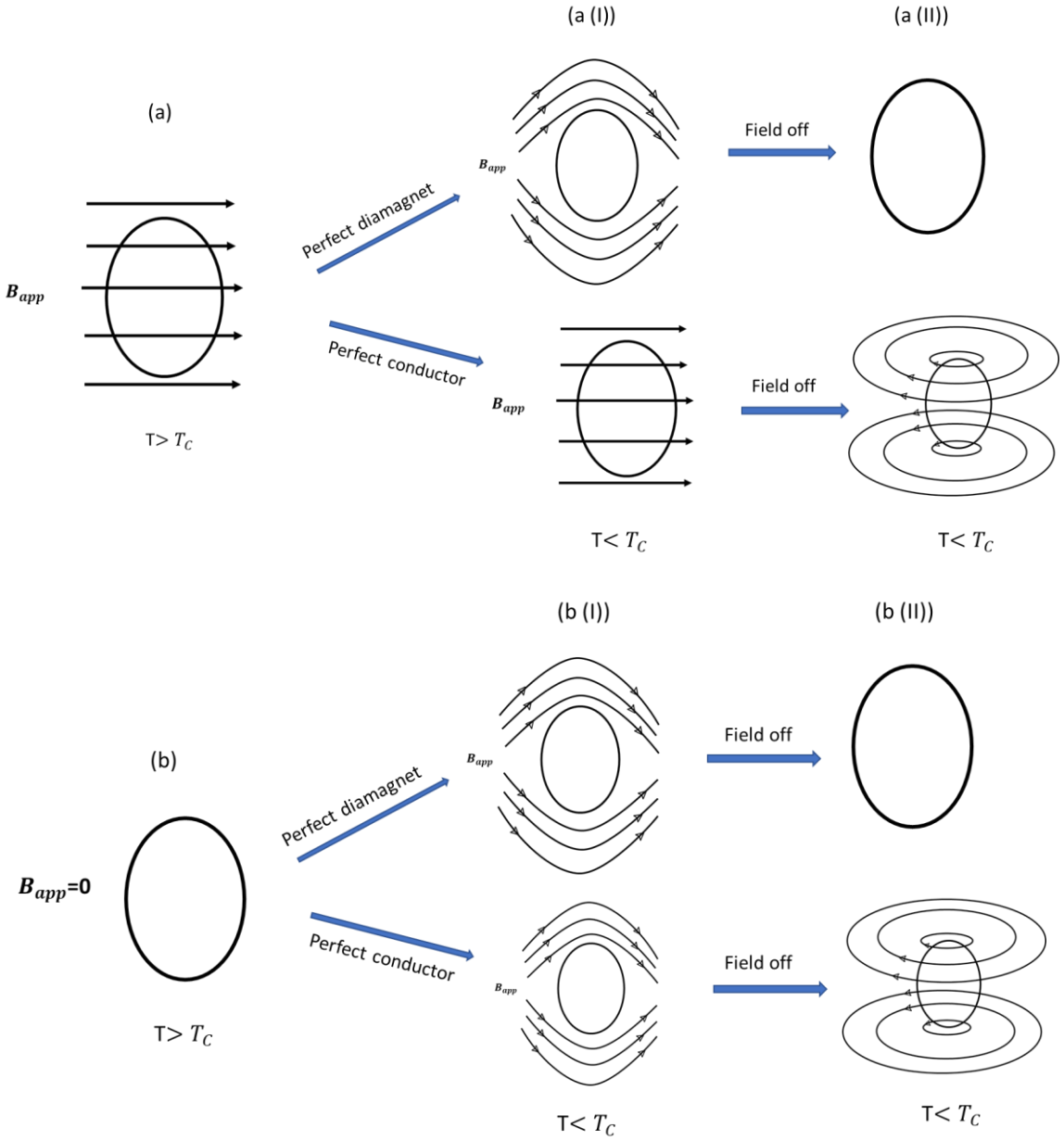


Figure 3.1: (a) Magnetic field is present in the metal above the transition temperature ($T_C$), (an (I)) when the perfect diamagnet is cooled below the $T_C$ the field is completely expelled from the superconductor. However, the perfect conductor allows flux to pass through it, (a(II)) comparing the behavior of the ideal conductor and diamagnet when the applied field

is turned off. There is no field within the perfect diamagnetic as soon as the field is off. In opposite, the perfect conductor retains the applied field in the opposite direction.

The main difference between the perfect conductor and the perfect diamagnet is illustrated in Figure 3.1. The important factor for their differences is the history of cooling. In Figure 3.1, two different cooling scenarios are presented. First, in the case of Figure 3.1 (a) cooling, the external magnetic field is present before the substance transition into the superconducting state. This type of cooling is called field cooling (FC). Whereas, in Figure 3.1 (b), no external magnetic field is present when the superconductor cooled through its transition temperature called zero-field cooling (ZFC). In the FC case, the perfect conducting state generates the persistent current due to the presence of the field (see 3.1 an (I)). Once the persistence current is set up in the superconductor state, it is unchanged irrespective of the condition of the external field (see 3.1 a(II)). However, in the diamagnetic state, there will be complete expulsion of the magnetic field from the interior of the superconductor (see 3.1 an (I)), and the field from the interior of the superconductor is off when the external field is off (see 3.1 a(II)). As shown in Figure 3.1 (b), both superconductors exhibit diamagnetic properties in the ZFC case.

## 3.2. Penetration depth

From the view of the macroscope scale, a weak magnetic field does not penetrate within the body of the superconductor. However, at the microscopic level, there will be a thin penetration layer of the magnetic field near the surface of the superconductor [44]. The length of the external magnetic field entering into the superconductor is called penetration depth. The first theory that describes the Meissner-Ochsenfeld effect and penetration depth was introduced by the London brothers (F. & H. London) in 1935. Their phenomenological theory, called the London equation, calculates the magnetic property of the superconductor. Here, I will derive the London equation, discuss the penetration depth, and compare it with the Pippard coherence length [45].

In the zero-frequency regime ($\omega = 0$), the static magnetic field ($\vec{B}$) relates with the DC density ($\vec{J}$) by the relation:

$$\Delta \times \vec{J} = -\frac{n_s e^2}{m_e}\vec{B} \tag{3.1}$$

Here,

$n_s$ =total superconducting electron density

$e$ =electronic charge

$m_e$ =bare electron mass in vacuum

According to Maxwell's equation, we can also write:

$$\Delta \times \vec{B} = \mu_0 \vec{J} \tag{3.2}$$

Using the cross product on both sides of (3.2), we get

$$\Delta \times (\Delta \times \vec{B}) = \mu_0 \Delta \times \vec{J} \tag{3.3}$$

Again, using Maxwell's equation $\Delta \cdot \vec{B} = 0$, equation (3.3) can be re-written as:

$$\Delta^2 \vec{B} = \frac{\mu_0 n_s e^2}{m_e} \vec{B} \tag{3.4}$$

$$\Delta^2 \vec{B} = \frac{1}{\lambda_L} \vec{B} \tag{3.5}$$

The solution of the equation (3.4) can be written as:

$$\vec{B}(z) = \vec{B}(0) \exp\left(-\frac{z}{\lambda_L}\right) \tag{3.6}$$

Where $\vec{B}(0)$ is the applied magnetic field and $\lambda_L$ has the dimension of the length and is called the penetration depth of the superconductor given by the following relation:

$$\lambda_L = \sqrt{\frac{m_e c^2}{4\pi n_s e^2}} \tag{3.7}$$

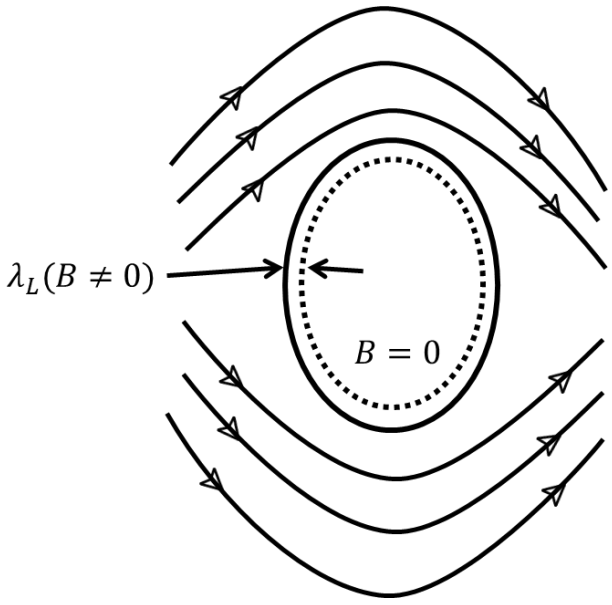


Figure 3.2: Illustration of penetration depth in a superconductor. The magnetic field decays exponentially to zero into the body of the superconductor.

This length gives an estimation of the penetration of the parallel external magnetic field into the interior of the superconductor (see Figure 3.2). For example, for aluminum, $\lambda_L \sim 500Å$, meaning that the externally applied field can enter up to this length within the superconducting aluminum. However, introducing a magnetic field larger than the critical field leads to the loss of superconductivity.

In equation (3.7), we can see that the London penetration depth depends inversely on the super electron density ($\propto \frac{1}{n_s}$). The $n_s$ depends upon temperature according to $\frac{n_s}{n} = 1 - \left(\frac{T}{T_C}\right)^4$.

The penetration depth is observed to be larger than that predicted by the London equations. The coherence length addresses this discrepancy between the experimental observation and theoretical prediction by the London equation. The temperature-independent coherence length is called Pippard coherence length. Table 3.2 compares the London penetration depth and the Pippard coherence length.

Table 3.2: comparison of penetration depth of superconducting materials [45].

| Material | $T_C$(K) | London Penetration Depth $\lambda_L\ (nm)$ | Coherence Length $\xi_0\ (nm)$ | Ratio $(\kappa = \frac{\lambda_L}{\xi_0})$ |
|---|---|---|---|---|
| Al | 1.18 | 1550 | 1600 | 0.01 |
| Sn | 3.72 | 34 | 230 | 0.16 |
| Pb | 7.20 | 37 | 83 | 0.43 |
| Nb | 9.25 | 39 | 38 | 1.02 |

The coherence length depends upon the energy gap of the superconductor. It is expressed mathematically as:

$$\xi_0 = \frac{\hbar v_F}{\pi \Delta} \tag{3.8}$$

Here, $v_F$ is fermi velocity and $\Delta$ is the energy gap of the superconductor.

## 3.3. Ginzburg-Landau theory

The internal energy in the superconducting transition is characterized by entropy (S) and magnetization (M). Studying the thermodynamics of the superconducting phase transition gives insight into different parameters like entropy, latent heat, specific heat capacity, etc. A theory that studies the thermodynamics of this phase transition is the Ginzburg-Landau (G-L) theory, which is based on the theory of second-order phase transition. It assumed that the free energy of the superconductor must depend smoothly on the order parameter $\psi(T)$. This parameter is defined as:

$$\psi(T) = \begin{cases} 0; T > T_C \\ \neq 0; T < T_C \end{cases}$$

The G-L theory for bulk materials shows the heat capacity has discontinuity at the transition temperature. Moreover, the G-L theory for inhomogeneous media defines $\psi$ in such a way that it also depends on spatial coordinate $\psi(r)$. This theory results in the Schrodinger equation with the nonlinear term. This effective nonlinear Schrodinger equation has application to study the response of superconductors to the external perturbation. The GL theory can be used to describe inhomogeneous superconductors like surfaces, interfaces, defects, and vortices. For example, it explains the proximity effect. Suppose a high $T_C$ superconductor (sc) is sandwiched to a low $T_C$ superconductor, which has a thickness less than the Ginzburg coherence length. Furthermore, the Ginzburg coherence length also helps identify the type of superconductor.

The London equation is valid for the slowly varying magnetic field [46]. The Ginzburg-Landau (G-L) theory introduced a global length called the GL coherence ($\xi(T)$).

$$\xi(T) = \frac{\hbar}{\sqrt{|2m^*\alpha(T)|}} \tag{3.9}$$

Where, $m^*$ represents the mass of the particle and $represents$ the expansion coefficient. The ratio between the characteristic length (London ($\lambda_L$) and Pippard ($\xi_0$)) defined the GL parameter [42]:

$$\kappa = \frac{\lambda_L}{\xi_0} \tag{3.10}$$

## 3.4. Types of superconductors

The GL parameter ($\kappa$) determines the type of the superconductor. When $\kappa < \frac{1}{\sqrt{2}}$, the superconductors are called type I superconductors, and when $\kappa > \frac{1}{\sqrt{2}}$ such superconductors are categorized as type II superconductors [47]. In a type I superconductor, when the applied external magnetic field is less than the critical field of the superconductor, the magnetic flux is completely expelled from the bulk of the superconductor called the Meissner effect. In a type II superconductor, there exist two regions, depending upon the applied external magnetic fields, $H_{C_1}$(lower critical field) and $H_{C_2}$(upper critical field). Below the $H_{C_1}$type II superconductor behaves as a type I superconductor. In between the $H_{C_1}$ and $H_{C_2}$, the field enters into the superconductor in the form of vortices. These vortices are called Abrikosov vortices and are quantized as:

$$\emptyset_0 = \frac{h}{2e} = 2.07 \times 10^{-15}\ Wb \tag{3.11}$$

Where, $e$ and $h$, respectively, represent electronic charge and Planck constant.

## 3.5. The BCS Theory

The Ginzburg-Landau theory is the phenomenology theory and successfully explains many fundamental properties of superconductivity. However, it cannot explain the microscopic origin of the superconductivity. Bardeen, Cooper, and Schrieffer proposed a theory in 1952, called the BCS theory, which explains the microscopic property of the

superconductor [48]. The important prediction of the BCS was the existence of an energy gap (2Δ) at the Fermi level in the energy spectrum of the superconductor [45].

The energy level of a normal metal can be illustrated in the Fermi sphere as depicted in Figure 3.3. The discussion here is motivated by Gennes's book (Page 7-9) [44]. In the sphere, the Fermi surface is defined with the energy $\varepsilon_F = \frac{{P_F}^2}{2m}$, where $P_F$ is the Fermi momentum and $m$ is the mass of the electron. Let us consider that we want to fill the available states with electrons of a non-interacting free electron gas. The energy levels at and below the Fermi surface ($P \leq P_F$) will be available for the electron, whereas above it ($P > P_F$) will be empty. Now, we want to excite an electron from a filled state of momentum $P$ to the available empty state of momentum $P'$. This electron-hole pair excitation takes energy:

$$E_{PP'} = \frac{P'^2 - P^2}{2m} \tag{3.12}$$

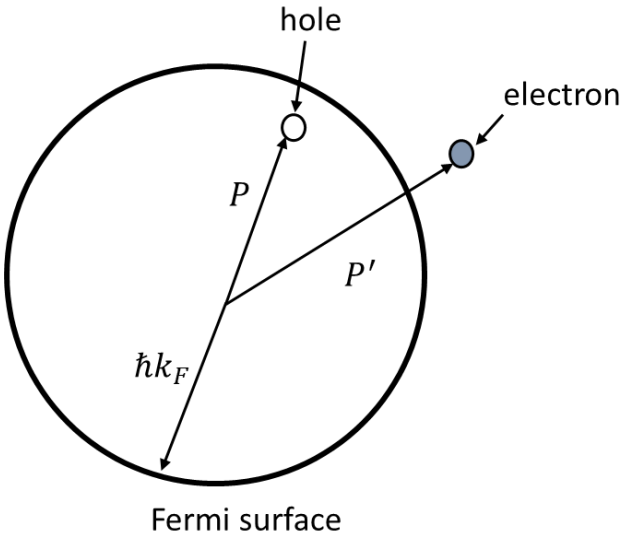


Figure 3.3: The Fermi sphere with the filled state at and below its surface. An electron in the state inside the sphere with momentum $P$ is being excited to the state outside of the sphere that has a momentum of $P'$.

For the two states $P$ and $P'$, numerous low excitations are possible when they are close to the $P_F$. Such excitations can be experimentally observed too. However, in the case of the superconductor, the energy required to excite an electron from the superconducting state was found to be greater than the certain pairing energy 2Δ:

$$E_{PP'} \geq 2\Delta \tag{3.13}$$

This higher excitation energy for an electron in the superconductor phase than the normal metal phase is explained by the BCS theory. The BCS theory, as stated in the Annet book

entitled "*Superconductivity, superfluids and condensates*" (page 128) [45], is built upon three important bases:

1. There exist repulsive force between two electrons in the normal metal due to the strong Coulomb interaction. However, in the superconducting state, an attractive force exists between the bound electrons via the exchange of virtual phonon.

2. The two electrons outside the occupied Fermi surface form a stable pair bound state due to the weak attractive force.

3. A many-particle wavefunction describes, which has the form of a coherent state wavefunction, all electrons near to the Fermi surface that are paired up.

The origin of attractive interaction between the two electrons in the superconducting state can be understood using the Feynman diagram as illustrated in Figure 3.4. A virtual phonon mediates the attractive interaction. The other electron absorbs the phonon released by one electron. Let us consider an electron in the state $K_1,\ \sigma_1$ release a phonon and scattered into the state $K_1 - q,\ \sigma_1$ as shown in Fig. 3.4. This released phonon with wave vector $q$ is then absorbed by an electron in the state $K_2,\ \sigma_2$ and pick up momentum $\hbar q$, thereby scattering into the $K_2 + q,\ \sigma_2$ state [49]. According to the conservation of momentum:

$$K_1 + (K_1 - q) = K_2 + (K_2 + q) \tag{3.14}$$

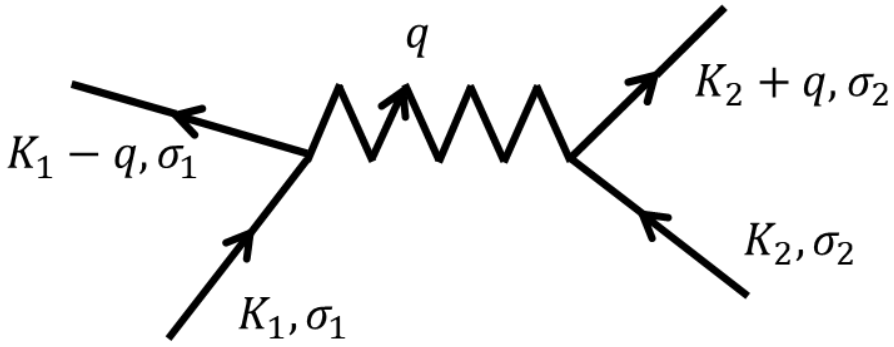


Figure 3.4: Illustrates the attractive interactions between two electrons in the superconducting phase. The origin of this interaction is due to the exchange of phonon between the electrons.

When one electron goes from the state $K_1$ to $K_1 - q$ state, it causes local oscillation of electron density of at the frequency:

$$\omega = \frac{\varepsilon_{K_1} - \varepsilon_{K_1 - q}}{\hbar} \tag{3.15}$$

Where, $\varepsilon_{k_1}$ and $\varepsilon_{k_1 - q}$ are the electron energy in the state $K_1$ and $K_1 - q$ respectively. The electrons that are close to the Fermi surface, as shown in Figure 3.5, within layer $2\Delta k$ take part in the phonon-mediated interaction. For the attractive energy to exist, the energies of the electron that differ from the Fermi energy should be less than the energy $\hbar\omega_D$, where

$\omega_D$ is Debye frequency. Let us suppose the interaction energy between by $V$. We can write the matrix element of the electron interaction energy [50]:

$$V_{kk'} = \begin{cases} -V, & |\varepsilon_k - \varepsilon_F| \leq \hbar\omega_D, \ |\varepsilon_{k'} - \varepsilon_F| \leq \hbar\omega_D \\ 0, & |\varepsilon_k - \varepsilon_F| > \hbar\omega_D, \ |\varepsilon_{k'} - \varepsilon_F| > \hbar\omega_D \end{cases} \quad (3.16)$$

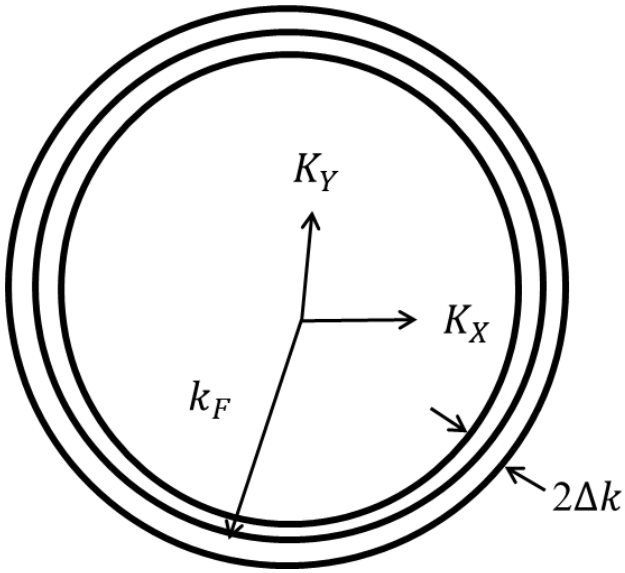


Figure 3.5: According to the BCS theory, only electrons close to the Fermi surface within the gap of $2k$ interact via the exchange of phonon.

The thickness of this layer, $2\Delta k$, is determined by the Debye energy:

$$\frac{\Delta k}{k_F} \sim \frac{\hbar\omega_D}{\varepsilon_F}, \varepsilon_F = \frac{\hbar^2 {k_F}^2}{2m} \quad (3.17)$$

### 3.5.1 Ground-state of a superconductor

In this section, the goal is to discuss the state of a superconductor when its energy is a minimum, that is, when $T = 0$. The derivation here is adapted from the Schmidt book [50].

The arbitrary wavefunction for a superconducting state can be expressed as:

$$\psi = \sum_n a_n \psi_n \quad (3.18)$$

Where,

$\psi_n = \psi_n(r_1, r_2, r_3, \ldots\ldots\ldots, r_N)$ =is a complete function where $n$ runs over a set of values which we assign a number to these functions,

$a_n$ =amplitude of the state $\psi_n$,

$|a_n|^2$ =probability of finding the system in the state $\psi_n$.

Let us consider the Hamiltonian operator $\hat{H}$

$$\hat{H} = \hat{H}_{Kin} + \hat{V} \tag{3.19}$$

The average energy is then found as,

$$\overline{E} = \int \psi^* \hat{H} \psi d\tau \tag{3.20}$$

Using equation (3.19) into (3.20), we get

$$\overline{E} = \overline{E}_{Kin} + \overline{V} \tag{3.21}$$

Where,

$$\overline{V} = \int \psi^* \hat{V} \psi d\tau \tag{3.22}$$

$$= \int (\sum_n a_n \psi_n)^* \hat{V} \sum_m a_m \psi_m \, d\tau$$

$$= \sum_{n,m} a_n^* \, a_m \int \psi_n^* \hat{V} \, \psi_m d\tau$$

$$= \sum_{n,m} a_n^* \, a_m V_{nm} \tag{3.23}$$

is the average potential energy and $V_{nm} = \int \psi_n^* \hat{V} \, \psi_m d\tau$ is matrix element transition from the state $\psi_n^*$ to the state $\psi_m$. The potential energy $\overline{V}$ in the above equation arises from the interaction of electrons via the virtual phonon. There is an attractive interaction between the electrons in the superconducting state close to the Fermi surface, which means potential energy exists between the electrons at $T = 0$ unlike the absence of such energy in the case of a normal metal. The presence of potential energy between the superconducting electrons leads to the reduction of the kinetic energy to fulfill the condition of total negative energy. It is possible to exist such interactions between two electrons with opposite momentum of equal magnitude and opposite spin $(k \uparrow, -k \downarrow)$ called the Cooper pair [51]. The sum in equation (3.23) is the sum of all possible transitions of such kind.

Suppose $\psi$ represents ground state wave functions for all Cooper pairs. Then, one can consider the mutual scattering of two coupled electrons from $(k \uparrow, -k \downarrow)$ to the new state $(k' \uparrow, -k' \downarrow)$ as a transition from the state $\psi_n$ to the state $\psi_m$. Here, the state $\psi_n$ corresponds to all states $(k \uparrow, -k \downarrow)$ full and the state $(k' \uparrow, -k' \downarrow)$ empty. Whereas the state $\psi_m$ corresponds to all states $(k \uparrow, -k \downarrow)$ empty and the state $(k' \uparrow, -k' \downarrow)$ full.

Now, let us suppose $v_k{}^2$ represents a new function of $k$ that gives the probability that the pair state $(k \uparrow, -k \downarrow)$ is occupied. The amplitude of the state $\psi_n$ corresponds to all states $(k \uparrow, -k \downarrow)$ full and the state $(k' \uparrow, -k' \downarrow)$ empty is given by:

$$a_n = \sqrt{{v_k}^2(1-{v_{k'}}^2)}=v_k u_{k'} \tag{3.24}$$

Where, $|u_{k'}|^2 = (1-{v_{k'}}^2)$ is the probability that the state $(k'\uparrow, -k'\downarrow)$ is unoccupied. A similar analogy can be used to calculate the probability of finding occupying of the state $\psi_m$:

$$a_m = v_{k'}u_k \tag{3.25}$$

Putting equations (3.24) and (3.25) in (3.2.13), we get $\overline{V} = \sum_{k,k'} V_{kk'}\ v_{k'}u_k v_k u_{k'}$. Hence, the total energy of the superconductor in the state $\psi_n$ can be written as:

$$E_s = 2\sum_k\ \varepsilon_k {v_k}^2\ + \sum_{k,k'} V_{kk'}\ v_{k'}u_k v_k u_{k'} \tag{3.26}$$

The first term in the equation (3.26) represents the kinetic energy, and the factor of 2 comes from the Cooper pair. The $\varepsilon_k$ term is the energy of the electron in the state $k$ that is measured from the Fermi level and is given by:

$$\varepsilon_k = \frac{\hbar^2 k^2}{2m} - \frac{\hbar^2 {k_F}^2}{2m}$$

$$= \overline{\varepsilon_k} - \varepsilon_F \tag{3.27}$$

We can reveal some properties of the function ${v_k}^2$ in the minimum energy state of $E_s$:

$$\frac{\partial E_s}{\partial {v_k}^2} = 0,$$

By using equation (3.24), we get,

$$2\varepsilon_k\ + V_{kk'}\frac{\partial u_k v_k}{\partial {v_k}^2}\sum_{k'}{}'\ v_{k'}u_{k'} = 0,$$

Using equation (3.16) in the above equation results:

$$2\varepsilon_k - 2V\frac{\partial u_k v_k}{\partial {v_k}^2}\sum_{k'}{}'\ v_{k'}u_{k'} = 0 \tag{3.28}$$

Let's evaluate $\frac{\partial u_k v_k}{\partial {v_k}^2}$ now,

$$\frac{\partial u_k v_k}{\partial {v_k}^2} = \frac{\partial v_k\sqrt{(1-{v_k}^2)}}{\partial {v_k}^2},$$

$$= \sqrt{(1-{v_k}^2)}\frac{\partial v_k}{\partial {v_k}^2} + v_k\frac{\partial\sqrt{(1-{v_k}^2)}}{\partial {v_k}^2},$$

$$= \sqrt{(1 - {v_k}^2)}\,\frac{1}{2v_k} + v_k\,\frac{(-1)}{2\sqrt{(1 - {v_k}^2)}},$$

$$= \frac{1 - {v_k}^2 - {v_k}^2}{2v_k\sqrt{(1 - {v_k}^2)}},$$

$$= \frac{1 - 2{v_k}^2}{2v_k u_k},$$

Now we put the value of $\frac{\partial u_k v_k}{\partial {v_k}^2}$ in equation (3.28):

$$2\varepsilon_k - V\frac{1-2{v_k}^2}{v_k u_k}\sum_{k'}{}' v_{k'}u_{k'} = 0,$$

$$V\frac{1-2{v_k}^2}{2v_k u_k}\sum_{k'}{}' v_{k'}u_{k'} = 2\varepsilon_k,$$

$$\frac{1 - 2{v_k}^2}{v_k u_k} = \frac{2\varepsilon_k}{V\sum_{k'}{}' v_{k'}u_{k'}},$$

$$\frac{v_k u_k}{1 - 2{v_k}^2} = \frac{V\sum_{k'}{}' v_{k'}u_{k'}}{2\varepsilon_k},$$

$$\frac{v_k u_k}{1 - 2{v_k}^2} = \frac{\Delta_0}{2\varepsilon_k} \tag{3.29}$$

Where,

$$\Delta_0 = V\sum_{k}{}' v_k u_k \tag{3.30}$$

The meaning of the prime sign in the summation is that the summation is taken over the states $k$ that are close to the Fermi surface such that the $V_{kk'}$ is non-zero (see equation (3.16)). The value of $\Delta_0$ is similar to that of the interaction energy $V$, which is non-zero in the interval of $2\Delta k$ (see Figure 3.5 for the illustration of such states). The energy $\varepsilon_k$is the energy of the individual electrons in the absence of the energy $V$.

The equation (3.29) can be re-arranged as:

$$\frac{{v_k}^2{u_k}^2}{(1-2{v_k}^2)^2} = \left(\frac{\Delta_0}{2\varepsilon_k}\right)^2,$$

$${v_k}^2 - {v_k}^4 = (1 - 4{v_k}^2 + 4{v_k}^4)\frac{{\Delta_0}^2}{4{\varepsilon_k}^2},$$

$${v_k}^2\left(1 + \frac{{\Delta_0}^2}{{\varepsilon_k}^2}\right) - {v_k}^4\left(1 + \frac{{\Delta_0}^2}{{\varepsilon_k}^2}\right) = \frac{{\Delta_0}^2}{4{\varepsilon_k}^2},$$

$${v_k}^4 - {v_k}^2 + \frac{{\Delta_0}^2}{4{\varepsilon_k}^2}\left(\frac{{\varepsilon_k}^2}{{\Delta_0}^2 + {\varepsilon_k}^2}\right) = 0,$$

$$v_k{}^4 - v_k{}^2 + \frac{\Delta_0{}^2}{4E_k{}^2} = 0 \tag{3.31}$$

Here,

$$E_k{}^2 = \Delta_0{}^2 + \varepsilon_k{}^2 \tag{3.32}$$

The solution of equation (3.29) can be written as:

$$v_k{}^2 = \frac{1 \pm \sqrt{1 - \frac{\Delta_0{}^2}{E_k{}^2}}}{2},$$

$$v_k{}^2 = \frac{1}{2}\left(1 - \frac{\varepsilon_k}{E_k}\right) \tag{3.33}$$

And,

$$u_k{}^2 = 1 - v_k{}^2 = \frac{1}{2}\left(1 + \frac{\varepsilon_k}{E_k}\right) \tag{3.34}$$

The negative sign in the solution of the $v_k{}^2$ is taken because when $k \to 0$, we will have $v_k{}^2 \to 1$ and $\varepsilon_k \to -\varepsilon_F$.

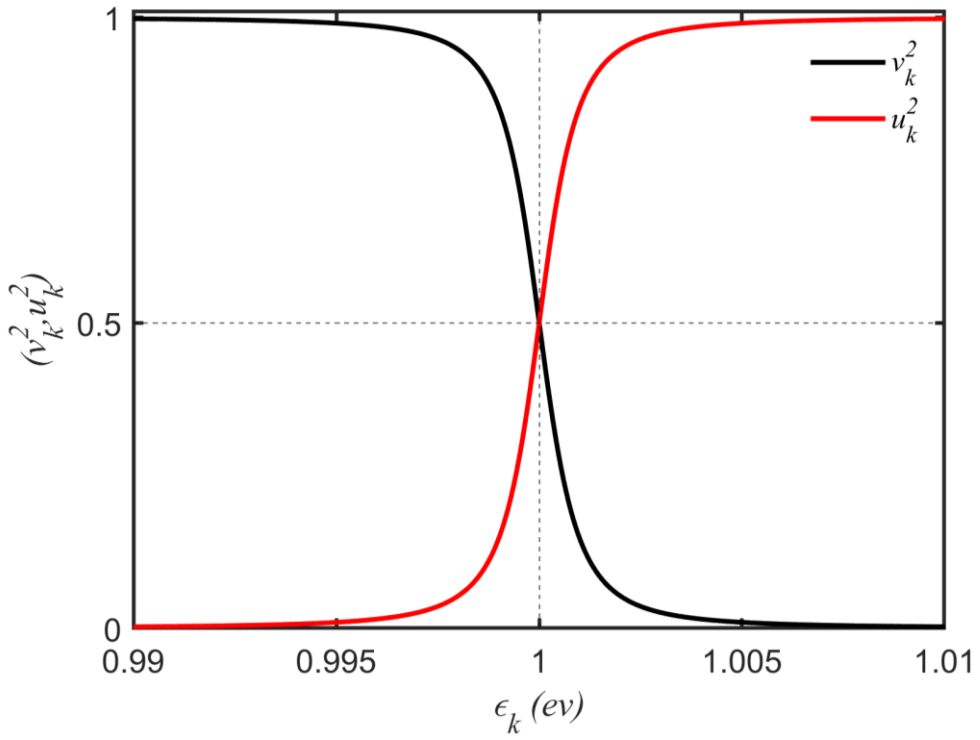


Figure 3.6: Probability that a Cooper pair occupies the state $(k \uparrow, -k \downarrow)$ $(v_k{}^2)$ or does not occupy the state $(u_k{}^2)$. Here, we have used $\varepsilon_F = 1\ ev$ and $\Delta_0 = 1meV$ in the figure [51].

The plot of probability that a Cooper pair occupies the state ($k\uparrow, -k\downarrow$) (${v_k}^2$) or does not occupy the state (${u_k}^2$) is shown in Figure 3.6. For the plotting, $\varepsilon_F = 1\ ev$ and $\Delta_0 = 1meV$ are used. There are three regions in the figure where the slope of the (${v_k}^2$, ${u_k}^2$) plot is different. Those regions are: (a) $\varepsilon_k \ll \varepsilon_F$ (deep within the Fermi surface), (b) $\varepsilon_k \cong \varepsilon_F$ (in or around the Fermi surface), (c) $\varepsilon_k \gg \varepsilon_F$ (far outside the Fermi surface). In the first region (a), the probability of finding the electron is 100 percent. However, if one goes far from the Fermi surface the chances of finding the electron will be zero. In other words, the value of ${u_k}^2$ will be one. Interesting physics happens in the region close to the Fermi surface (c). There is a drastic change in the slope of the graph in this region. Here, the ratio $\frac{\Delta_0}{\varepsilon_F}$ is equal to $10^{-3}$. Meaning that only 0.1 percent of all electrons that are close to the $\varepsilon_F$ participate in superconductivity [51].

### 3.5.2 Energy gap

In this section, the expression of the temperature-independent energy gap ($\Delta_0$) will be calculated and compared with the temperature-dependent energy gap ($\Delta(T)$). By using values of $v_k$ and $u_k$ from equations (3.33) and (3.34) in equation (3.33), we get:

$$\begin{aligned}\Delta_0 &= V {\sum_k}' \sqrt{\frac{1}{2}\left(1-\frac{\varepsilon_k}{E_k}\right)}\sqrt{\frac{1}{2}\left(1+\frac{\varepsilon_k}{E_k}\right)} \\ &= \frac{1}{2}V {\sum_k}' \left(1-\frac{{\varepsilon_k}^2}{{E_k}^2}\right)\end{aligned} \tag{3.35}$$

Using equation (3.33) in the above equation, we get

$$1 = \frac{1}{2}V {\sum_k}' \frac{1}{\sqrt{{\varepsilon_k}^2 + {\Delta_0}^2}} \tag{3.36}$$

If the condition in equation (3.16) is implemented in the equation (3.36) and the summation over $k$ is changed to integration over $\varepsilon$ as,

$$\sum_k{}' \ldots . = \int_{-\hbar\omega_D}^{\hbar\omega_D} \ldots\ldots N(\varepsilon)d\varepsilon,$$

Where $N(\varepsilon)$ is the density of states at the energy $\varepsilon$. Now, replacing the summation in equation (3.36) by the above integration near the Fermi surface, where $N(\varepsilon) = N(0)$ and $\varepsilon_k = \varepsilon$, we get

$$1 = N(0)V \int_0^{\hbar\omega_D} \frac{d\varepsilon}{\sqrt{\varepsilon^2 + {\Delta_0}^2}}$$

$$\frac{1}{N(0)V} = \sinh^{-1}\left(\frac{\hbar\omega_D}{\Delta_0}\right)$$

$$\frac{\hbar\omega_D}{\Delta_0} = \sinh\left(\frac{1}{N(0)V}\right)$$

$$\Delta_0 = \frac{\hbar\omega_D}{\sinh(\frac{1}{N(0)V})} \tag{3.37}$$

As discussed in the earlier paragraph, only a small fraction of electrons that are close to the Fermi surface take part in the superconductivity: $N(0)V \leq 0.3$ [50]. This is called the weak coupling limit. In the weak limit, equation (3.37) can be written as [52]:

$$\Delta_0 \approx 2\hbar\omega_D e^{-(\frac{1}{N(0)V})} \tag{3.38}$$

The derivation of the temperature-dependent energy gap is skipped here. The temperature-dependent energy gap here is given by [49].

$$\frac{1}{N(0)V} = \int_0^{\hbar\omega_D} \frac{d\varepsilon}{\sqrt{\varepsilon^2 + \Delta^2(T)}} \tanh\frac{\sqrt{\varepsilon^2 + \Delta^2(T)}}{2K_B T_C} \tag{3.39}$$

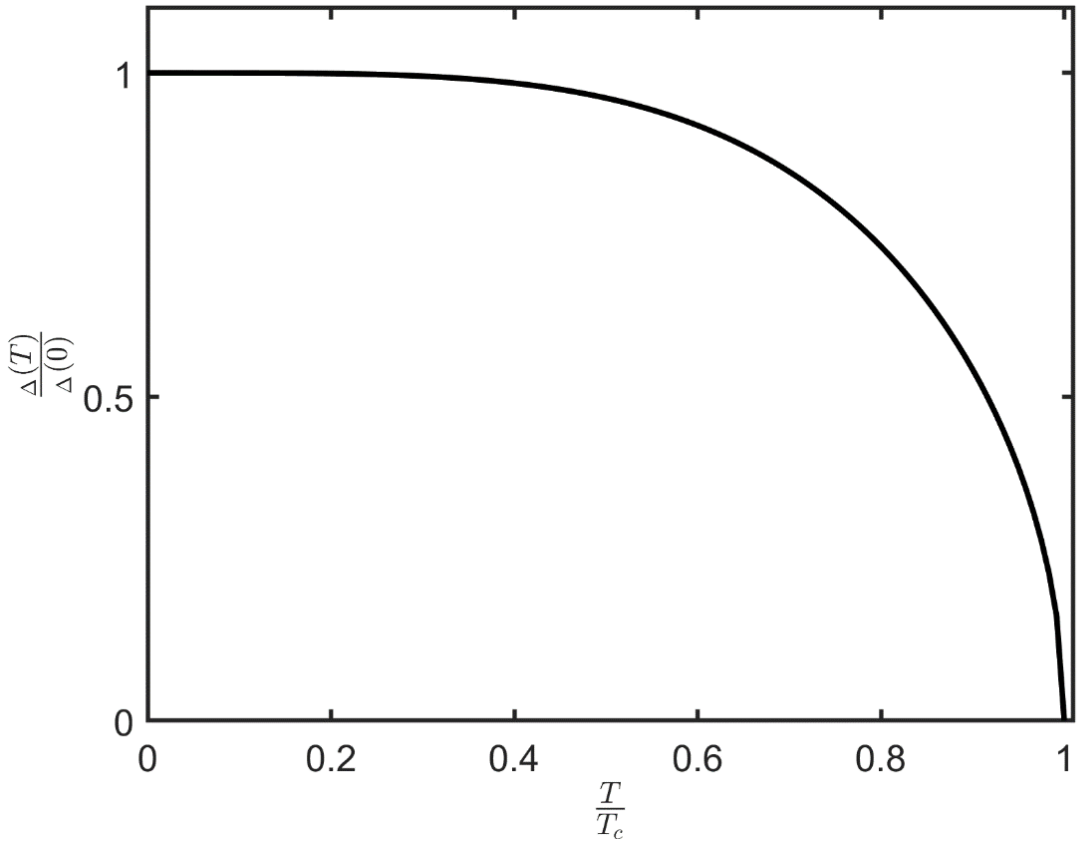


Figure 3.7: The variation of energy gap $\Delta(T)$ compared with $\Delta(0)$ as a function of temperature.

Solution of equation (3.39) yields,

$$\frac{\Delta(T)}{\Delta(0)} \approx \sqrt{\cos(\frac{\pi t^2}{2})} \tag{3.40}$$

Where $t = \frac{T}{T_C}$, here $T_C$ is the critical temperature of the superconductor. Figure 3.7 shows the variation of the energy gap as a function of temperature. The energy gap of the superconductor varies rapidly at the critical temperature of the superconductor ($T_C$). As the temperature drops further down from $T_C$, the more the Cooper pair forms, and their binding energy increases. Hence, the higher value of thermal energy ($K_B T_C$) is required for their excitations [53]. Near $T = 0$, the temperature variation of $\Delta(T)$ is constant and equals to $\Delta(0)$ ($or\ \Delta_0$).

The solution of (3.39) yields:

$$\Delta_0 \approx 1.76 K_B T_C \tag{3.41}$$

Different experiments accurately verify the relation (3.41). Table 3.3 shows examples of variation of energy gap ($2\Delta_0$) for different superconducting materials. From the experiments, one can establish relation $3.0 K_B T_C \leq 2\Delta_0 \leq 4.5 K_B T_C$, with most clustered near the BCS value of $3.5 K_B T_C$ [42].

Table 3.3: Variation of energy gap for different superconducting materials [48].

| Material | $T_C$(K) | $2\Delta_0\ (meV)$ | $\frac{2\Delta_0}{K_B T_C}$ |
|---|---|---|---|
| Al | 1.18 | 0.35 | 3.4 |
| Hg | 4.2 | 1.7 | 4.6 |
| Pb | 7.2 | 2.7 | 4.3 |
| Nb | 9.3 | 3.0 | 3.8 |

The next chapter will discuss what happens when a magnet is put on the surface of the superconducting coaxial quarter-wave microwave cavity. In this chapter, we learned about the macroscopic and microscopic properties of the superconductor. For example, the superconductor exhibits the diamagnetic property. Similarly, there will be a small penetration depth within the superconductor in the presence of the external magnetic field. The BCS theory explains the attractive interaction between electrons bound in the cooper pair. Moreover, the energy gap of the superconductor and its variation as a function of temperature is derived.

# Chapter 4

# Cavity-Magnet System

*"To find yourself, think for yourself."-Socrates*

## 4.1 Introduction

A weak magnet above a superconductor generates a supercurrent on the surface of the superconductor (see Figure 4.1). This supercurrent prevents the entry of an external magnetic field from the interior of the superconductor. The magnetic field associated with this creates a force called the diamagnetic force. It is directed opposite to the applied field. When the opposing diamagnetic force is greater than the gravitational force, the magnet levitates above the superconductor.

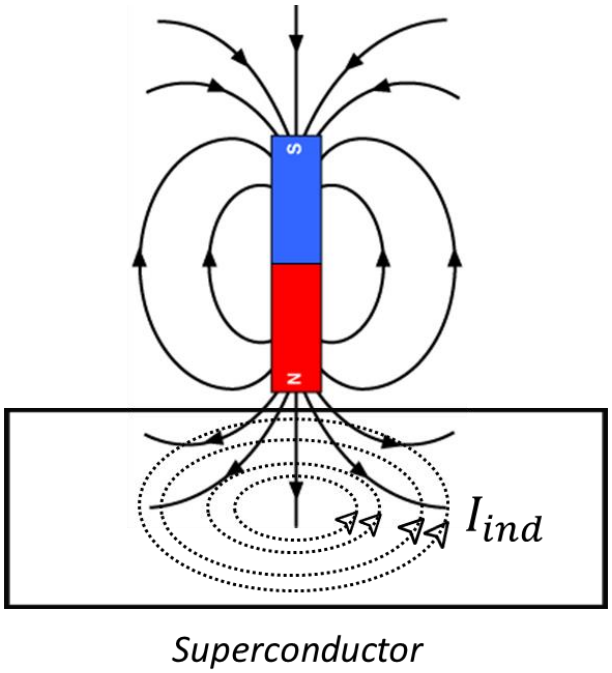


Figure 4.1: A magnet above a superconductor induced opposing current on the surface of the superconductor.

Furthermore, introducing a magnet within a cavity changes its frequency and quality factor. In this chapter, a lumped element model is developed, and FEM simulations are done to characterize frequency shift patterns. A study of the total quality factor of the cavity with the presence of the magnet is also done. Finally, the two-loop model calculates levitation height and studies stable magnetic levitation.

## 4.2 Neodymium Magnets

The magnet that we have used in our experiment is the permanent neodymium magnets of varying strength from 1.22-1.47 T. They are graded according to their remanence ($B_r$) as

tabulated in Table 4.1. For example, the magnet with remanence 1.32 T is called an N42 magnet. The density of the neodymium is $7.4\times 10^{-3}\ {}^{kg}/_{m^3}$. The thermal expansion (0 to 100℃) of the neodymium magnet parallel and perpendicular to the direction of magnetization is, respectively, $5.2\times 10^{-6}\ {}^{1}/_{°C}$ and $-0.8\times 10^{-6}\ {}^{1}/_{°C}$ [54].

Table 4.1: Neodymium magnets classified with their remanence.

| Type of Neodymium magnet | Remanence (T) |
|---|---|
| N35 | 1.22 |
| N42 | 1.32 |
| N50 | 1.44 |
| N52 | 1.47 |

Figure 4.2 (a) shows a sketch of a disc magnet that has a radius of $R$ and thickness of $2b$. The mass of the magnet ($M$) can be calculated using the relation:

$$M = 2\pi R^2 b\rho \qquad (4.1)$$

Where $\rho$ is the density of the magnet. Now, the weight of the magnet can be derived from its mass ($M$) as $W = Mg$. Figure 4.2 (b) shows an example of magnetic field lines of an N50 permanent magnet with $R = 0.5\ mm$ and $b = 0.25\ mm$. Here (0,0) is the center of the magnet.

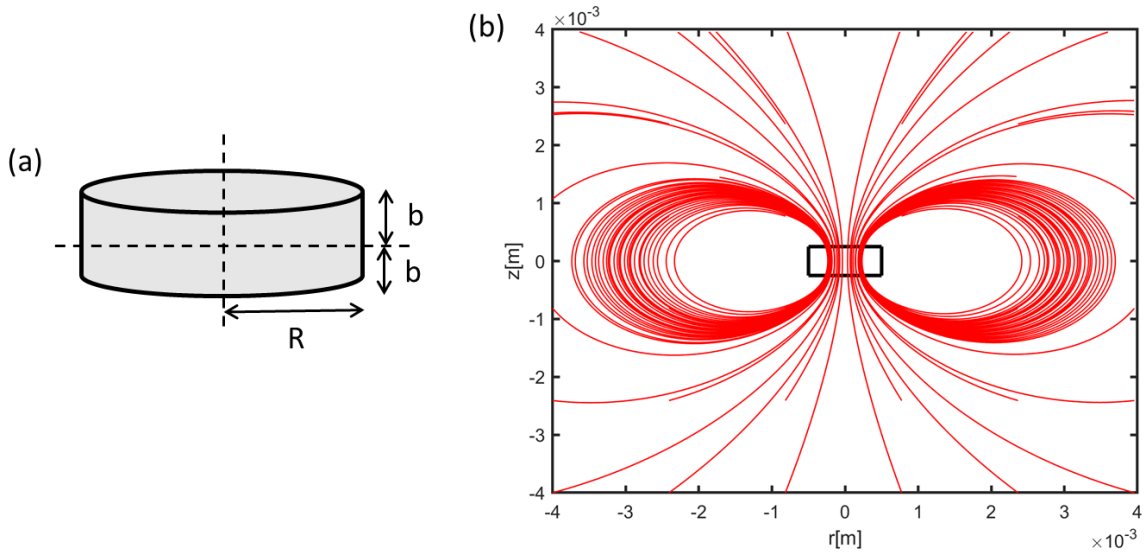


Figure 4.2: (a) A disc magnet of a radius of $R$ and a height of $2b$, (b) magnetic field distribution of an N50 magnet.

A simple approach to calculating a permanent magnet's magnetic field is to consider it as a solenoid (loop of currents). Then the magnetic field through the symmetric axis of the magnet is given by [55]:

$$B_z = \frac{B_r}{2}\left[\frac{Z+b}{\sqrt{R^2+(Z+b)^2}} - \frac{Z-b}{\sqrt{R^2+(Z-b)^2}}\right] \qquad (4.2)$$

Here, $B_r$ is a remanence of the magnet. Equation (4.2) calculates the magnetic field more accurately outside of the magnet than its inside.

Figure 4.3 shows the decay of the magnetic field for an N50 neodymium magnet of a radius of 0.5 *mm* and height of 0.5 *mm* from its surface. The field varies rapidly from the surface to the distance of 1 mm. For the magnetic field calculation, the origin of the coordinate is considered at the center of the magnet. The strength of the magnet reduced approximately half at the surface (~0.5 T) than that at the center of the magnet (1.44 T) and is negligible above 2.5 *mm*.

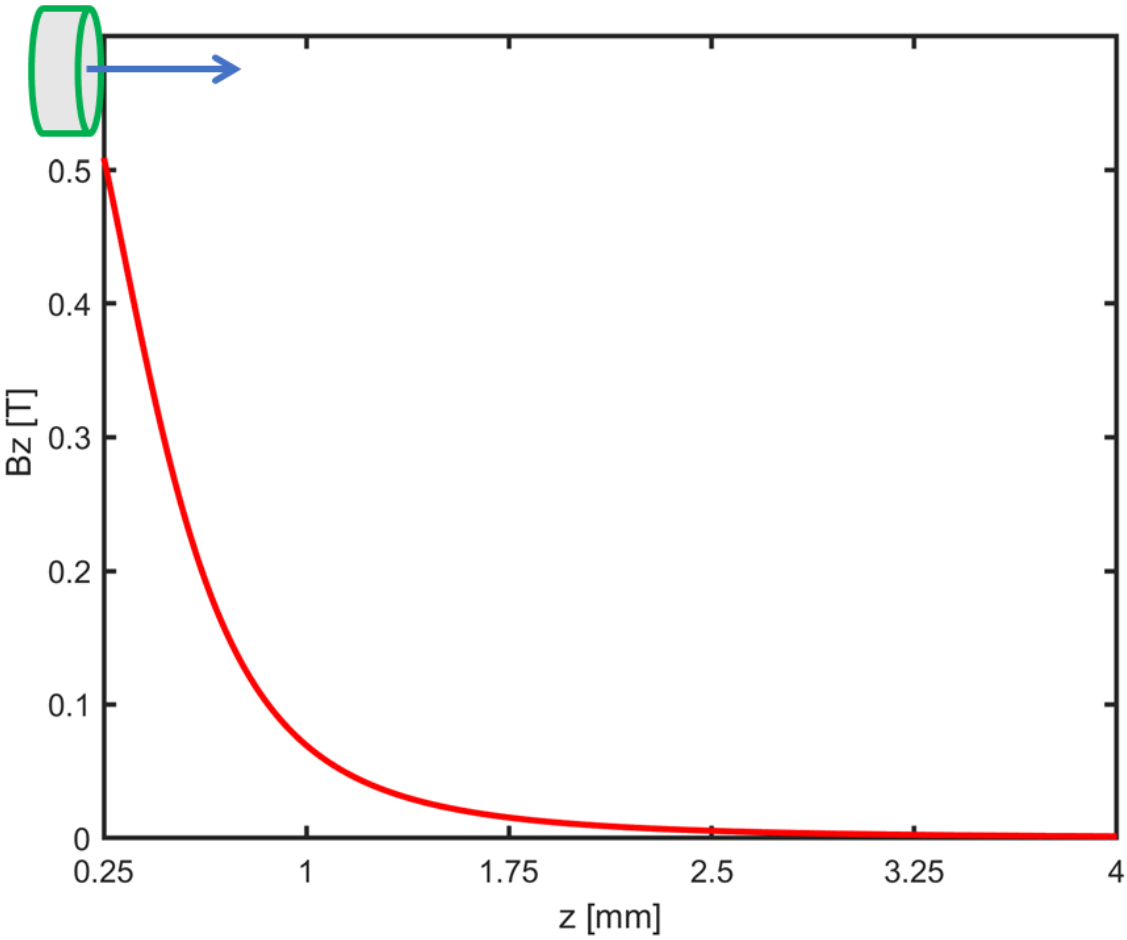


Figure 4.3: Azimuthal magnetic field ($B_z$) along the symmetric axis of a magnet of radius 0.5 mm and height 0.5 mm. The field is calculated from the surface of the magnet.

Another advantage of magnetic field calculation using equation (4.2) will be to calculate the magnetic field on the surface of various magnets. It is important to know the surface magnetic field in the levitation experiments. The strength of the magnetic field on the surface of the magnet affects magnetic levitation. For example, suppose the critical field of a superconductor is 100 gauss, and the field on the surface of the magnet is higher than the critical field. In that case, some part of the superconductor will be normal during the superconducting transition. The effect of such a normal region on levitation will be discussed in the upcoming section. Table 4.2 shows a list of the surface magnetic field of four magnets that we used in our sequence experiment.

Table 4.2: Surface magnetic field for the permanent magnets of dimension 0.5 mm (radius) × 0.5 mm (thickness).

| Magnet | Surface field (T) |
|---|---|
| N35 | 0.43 |
| N42 | 0.47 |
| N50 | 0.51 |
| N52 | 0.52 |

## 4.3. Frequency shift pattern

The frequency, *f*, of a coaxial stub cavity, discussed in section 2, is determined by the height of the stub, *l*, where $f \alpha \frac{4}{l}$ [2]. Any external perturbation within the coaxial region of the cavity changes the shape of the cavity mode and hence its frequency [35]. When a magnet is placed on the surface of the stub it pulls down the frequency of the cavity. The reason is an increase in the effective height of the stub. The amount of downshift corresponds to the interaction of the magnet with the electric field of the cavity mode, which is localized toward the edges of the stub. In this section, two different approaches will be discussed to characterize the frequency shift pattern of the cavity due to the presence of the magnet. First, the lump element model is developed for the cavity-magnet system. Then, different possible scenarios of magnetic levitation and associated frequency shift patterns due to such a phenomenon will be presented using FEM simulations.

### 4.3.1 Lump Circuit Model

An LC circuit can approximate the frequency of an empty cavity without any external perturbation. In the LC circuit model, the frequency of the bare cavity can be expressed in terms of inductance ($L_0$) and capacitance ($C_0$) as:

$$f_0 = \frac{1}{2\pi\sqrt{L_0 C_0}} \tag{4.3}$$

Where,

$$L_0 = \frac{\mu h_s}{2\pi} \ln\left(\frac{r_c}{r_s}\right) \tag{4.4}$$

Here, $r_c$ denotes the radius of the cavity, $r_s$ the radius of the stub, and $h_s$ the height of the stub. For the cavity configuration with a long gap between the stub and open end, the exact expression of capacitance is not known. A similar cavity with the gap reduced in the order of millimeters is called the reentrant cavity. For such cavity, the value of $C_0$ can be found using the relation:

$$C_0 = \epsilon_0 \frac{\pi {r_c}^2}{h} \tag{4.5}$$

A magnet sitting on the surface of the stub changes the frequency of the bare cavity. The lumped circuit model can model the magnetic perturbation within the cavity[56]. In this model, the frequency of the cavity is given by:

$$f = \frac{1}{2\pi\sqrt{L_0 C}} \tag{4.6}$$

Here, *C* is the capacitance of the cavity. For a cavity with a long cylindrical section between the stub and the open end of the cavity, the electric field is concentrated on the coaxial region, and the exact expression for the capacitance is not known [38]. We assume that a magnet placed near the top of the stub ($z < 1\,mm$), where the electric field is strong, changes the effective capacitance of the cavity according to $C = C_0 + C_1$, where $C_0$ quantifies the capacitance of the bare cavity and $C_1$ represents the capacitive contribution of the magnet. The $C_1$ can be modeled as the interaction of the magnet with the energy density of the cavity falling approximately by $e^{-2\beta z}$ into the waveguide section of the cavity, where $\beta = \sqrt{(\frac{2\pi}{\lambda})^2 - (\frac{2.41}{r_c})^2}$, $\lambda$ is the resonance wavelength [3]. Now, using equation (4.3) in equation (4.6), we get:

$$f = \frac{1}{2\pi\sqrt{(L_0(C_0 + C_1))}}$$

$$f = \frac{1}{2\pi\sqrt{(L_0 C_0(1 + C_1/C_0))}}$$

$$f = \frac{f_0}{(1 + C_1/C_0)^{\frac{1}{2}}} \tag{4.7}$$

A Taylor expansion of equation (4.7) yields,

$$(1 + \frac{C_1}{C_0})^{-\frac{1}{2}} = (1 - \frac{C_1}{2C_0})$$

$$f = f_0(1 - \frac{C_1}{2C_0})$$

$$\frac{{f_0}^2 - f^2}{{f_0}^2} \propto \frac{C_1}{2C_0}$$

$$\frac{{f_0}^2 - f^2}{{f_0}^2} \propto e^{-2\beta z} \tag{4.8}$$

### 4.3.2 FEM Simulations

The frequency shift pattern of a cavity-magnet is studied by putting a magnet on the different locations around the stub. The cavity used in the simulations has the same dimensions as discussed in Chapter 2, section 2.3. The magnet is a disc magnet of a diameter of 1 mm and a height of 0.5 mm. Here, simulations for various possible phenomena during the levitation experiment such as magnetic levitation, sliding, flipping, and levitation with an angle of the magnet are studied.

#### I. Levitation

Figure 4.4 shows the colormap of the frequency shift as a function of the radial and vertical position of the magnet. The vertical distance is measured from the magnet's surface to the stub's surface and the radial distance from the center of mass of the magnet. For example, when the magnet is at $(x, z) = (2\ mm, 0.5\ mm)$ this means that the half part of the magnet is on the stub, while the other half is outside the stub at the height of 0.5 mm. Moreover, the frequency of the bare cavity is 11.007 *GHz*. The change in the frequency of the cavity (Δf) is calculated in comparison to the frequency of the bare cavity. The frequency sensitivity refers to the difference in the frequency with respect to the position of the magnet.

In Fig. 4.4, we can divide the cavity into three regions based on the frequency sensitivity: (a) Near the center of the stub ($x < 1\ mm$), (b) Around the stub ($1\ mm \leq x \leq 3\ mm$), and (c) In the gap of the cavity ($x > 3\ mm$). In region (a) the change in the frequency of the cavity is small with the radial and vertical position of the magnet and more so in the region (c). The region (b) is the most sensitive region of the cavity. In this region, the small displacement of the magnet results in a significant change in the frequency. For example, when the magnet at position ($x = 1.9\ mm, z = 0\ mm$) is moved to the positions ($x = 2\ mm, z = 0\ mm$) and ($x = 2.1\ mm, z = 0\ mm$) the frequency sensitivity will be around 200 *MHz/mm*. The frequency sensitivity is even high due to the vertical displacement. For example, when the magnet at positions ($x = 1.9\ mm, z = 0\ mm$), ($x = 2\ mm, z = 0\ mm$), and ($x = 2.1\ mm, z = 0\ mm$) is moved to the positions ($x = 1.9\ mm, z = 0.1\ mm$), ($x = 2\ mm, z = 0.1\ mm$), and ($x = 2.1\ mm, z = 0.1\ mm$) the frequency of the cavity is shifted by the rate of 700 *MHz/mm*.

The change in the frequency (Δf) of the cavity mainly depends upon the interaction of the magnet with the electric field ($E(r, z)$). In addition, with the amount of electric field storage in the space between the magnet and the stub. Remember, the electric field of the coaxial microwave cavity is localized around the circumference of the stub. Hence, region (c) is the most sensitive region in the entire cavity.

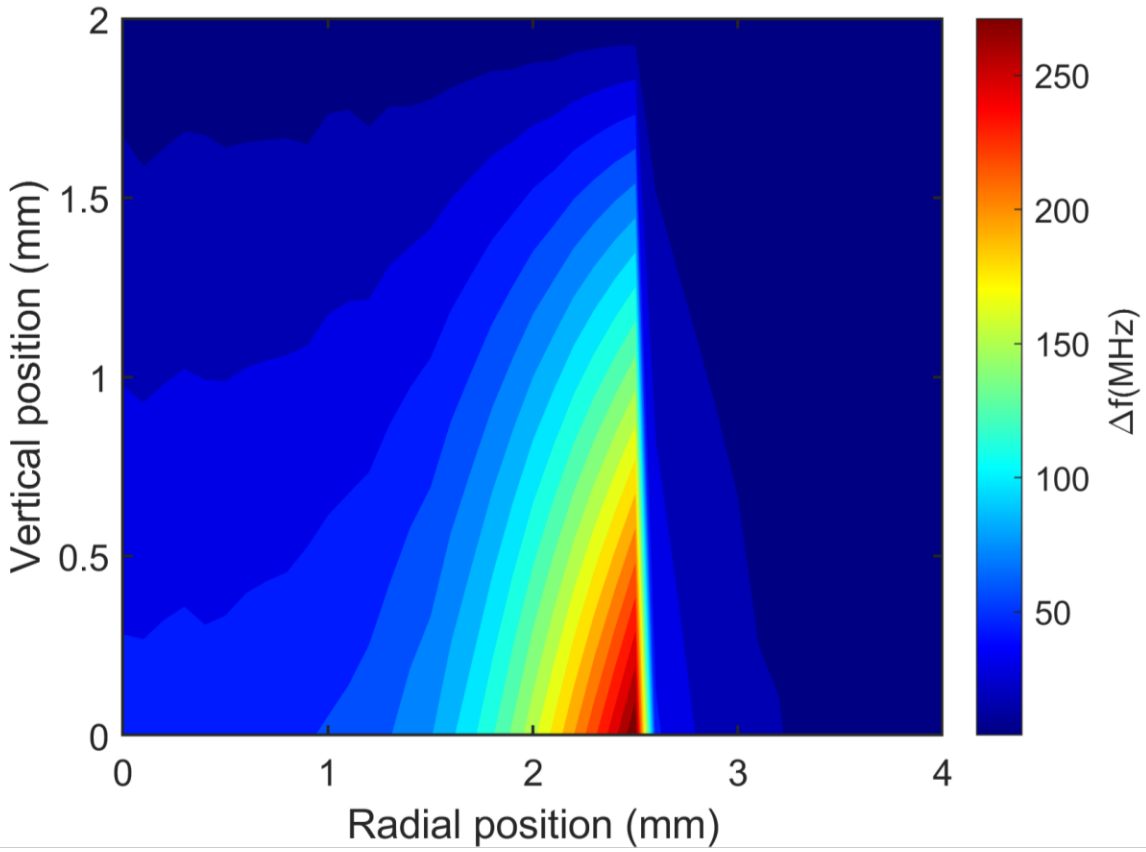


Figure 4.4: Colormap of the change in the resonance frequency of the cavity as a function of the radial and vertical position of a magnet on the stub.

## II. Levitation with an angle

Suppose a disc magnet magnetized along its thickness is placed above a superconductor. It will make an angle with the superconductor during levitation to be in the minimum potential energy state [57]. Figure 4.5 illustrates the tendency of a magnet to change the resonance frequency of the cavity lifting with an angle from the edge of the stub ($x = 2\ mm$). See inset of figure for the example demonstrations of magnetic levitation for angles $0^{\circ}, 45^{\circ}, 90^{\circ}$. On the surface of the stub, even $10^{\circ}$ angle will induce the frequency downshift of 30 MHz. The decreasing trend of the frequency will continue as the angle increase from $0^{\circ}$ to $90^{\circ}$. However, the trend will reverse, and the frequency of the cavity will start to upshift as the angle change from $90^{\circ}$ to $180^{\circ}$.

Magnetic levitation always upshifts the frequency of the cavity, irrespective of position and orientation of the magnet on the stub. The orientation and position of the magnet play the main role in the amount of the upshift. In Fig. 4.5, the frequency sensitivity is largest near the stub ($z{\sim}0.5\ mm$). In this region, the effect of most of the angles on the frequency is distinguishable. As the magnet move farther from the stub ($z > 1\ mm$), the effect becomes indistinguishable.

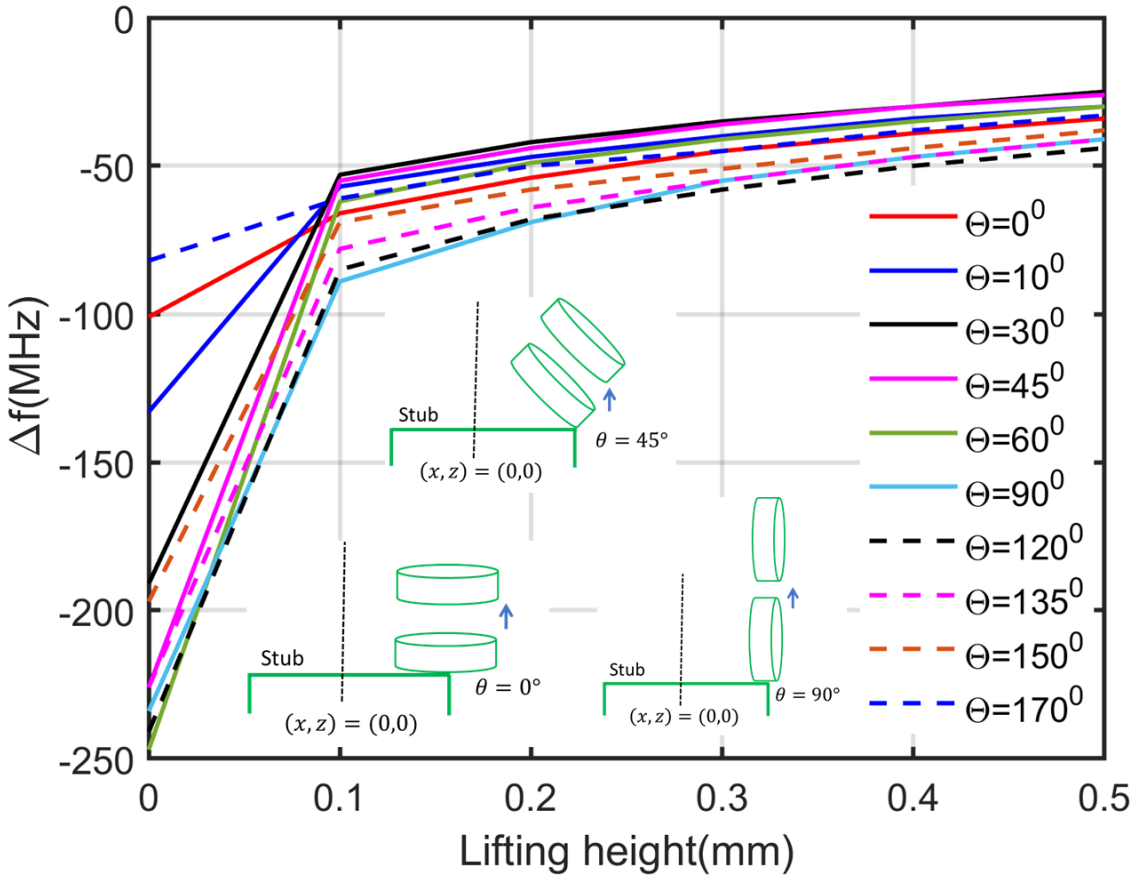


Figure 4.5: FEM simulations show magnetic levitation shifts the cavity frequency towards the bare cavity frequency. This plot identifies the amount and trend of the frequency shift for magnetic levitation for different magnet orientations.

## III. Sliding towards the edge

Now imagine the following scenario: a magnet that is put at the center of the stub slide towards the edge. One question that might arise is what effect this phenomenon has on the cavity's frequency. In fact, a more general question could be the frequency shift patterns due to the sliding of the magnet.

A perfect diamagnet pushes a magnet towards its edge due to the edge effect [58]. Figure 4.6 shows FEM simulations of how the frequency shift as a function of radial position for magnets of several angular orientations, as obtained from the FEM simulations. The magnet remains in contact with the surface of the stub for these calculations. The cavity's resonance frequency decreases when a magnet in contact with the stub slides towards the edge. The amount of such a downshift depends on the orientation of the magnet. The sudden changes in the frequency shift as the radial position increases beyond 1.5 mm are due to the edge of the magnet closest to the stub surface extending past the edge of the stub.

Two different trends of frequency shift are observed at the center and the edge of the stub for the angle less than or equal to 120 degrees and greater than 120 degrees. At the center

of the stub, the frequency downshifts when the angle increases from 0 to 120 degrees. And, when the angle is greater than 120 degrees, the frequency shifts upward. However, the opposite trend of the frequency shift is observed at the edge of the stub. The frequency of the cavity increases as the magnet makes an angle less than or equal to 120 degrees except for 90 degrees. The frequency goes down for an angle greater than 120 degrees. The largest frequency downshift of (Δf=) 382 MHz is observed when the magnet is close to the edge and oriented at 90 degrees, or standing on its edge.

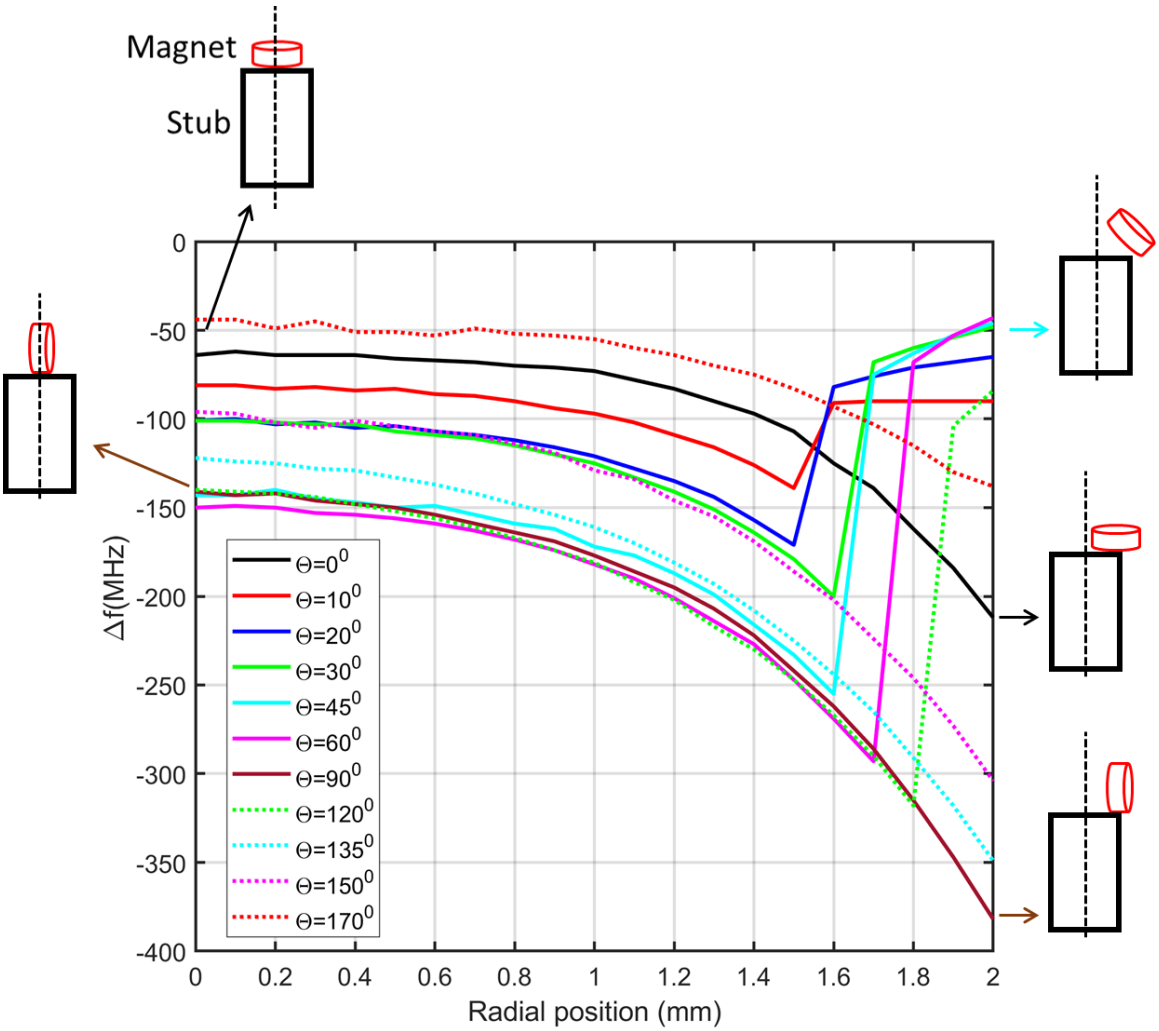


Figure 4.6: Change in the frequency of the cavity as a magnet slides towards the edge of the stub with different orientations. The sketches adjacent to the graphs indicate the orientation of the magnet with respect to the stub.

Table 4.3 summarizes the change in the cavity frequency at different orientations of the magnets at the center and edge of the stub. The arrow in the table shows the amount and trend of the frequency shift at the center and edge of the stub. There is an opposite trend of a frequency shift on those locations of the stubs with orientation less than or equal to 120 degrees and greater than 120 degrees.

Table 4.3: Summary of the frequency change as the magnet, in contact with the stub, slides towards the edge of the stub with different angles.

| Orientation (°) | $\Delta f\|_{x=0\ mm}$ (MHz) | $\Delta f\|_{x=2\ mm}$ (MHz) | Total f change (MHz) | Total f change (%) |
|---|---|---|---|---|
| 0 | -62 | -212 | -150 | 241 (↓) |
| 10 | -81 | -90 | -9 | 11 (↓) |
| 20 | -101 | -65 | +36 | 36 (↑) |
| 30 | -101 | -48 | +53 | 53 (↑) |
| 45 | -143 | -46 | +96 | 67 (↑) |
| 60 | -150 | -43 | +107 | 71 (↑) |
| 90 | -141 | -382 | -241 | 171 (↓) |
| 120 | -140 | -84 | +56 | 40 (↑) |
| 135 | -122 | -349 | -227 | 186 (↓) |
| 150 | -96 | -304 | -208 | 217 (↓) |
| 170 | -44 | -138 | -94 | 214 (↓) |

## IV. Rotation

Another phenomenon to consider during the levitation experiment is the rotation of the magnet. The rotation of the magnet also affects the frequency of the cavity. Figure 4.6 illustrates the effect of magnetic rotating at $x = 1.5\ mm$ on the frequency of the cavity. In these simulations, the center of mass of the magnet is fixed at $x = 1.5\ mm$, and the distance between the magnet and the stub is adjusted so that the magnet is always in contact with the stub. In addition, the rotation of the magnet is done manually.

The rotation of the magnet results in an asymmetry double-well like frequency shift profile (see Figure 4.7). This asymmetry arises because the part of the magnet that is in contact with the stub moves inwards while making the acute angle and it moves outward while making the obtuse angle to maintain the center of mass of the magnet at $x$=1.5 $mm$ (see inset of Fig. 4.6). The center of the well is at 90 degrees. For the acute angle highest shift of $\sim 200\ MHz$ is observed for angles 50, 60, and 70 degrees. In the case of obtuse angle, the maximum of $220\ MHz$ of frequency downshift is observed at 100 degrees and is remains reasonably constant for angles 100-140 degrees. For the angle greater than 140, an increasing trend of the frequency shift is observed.

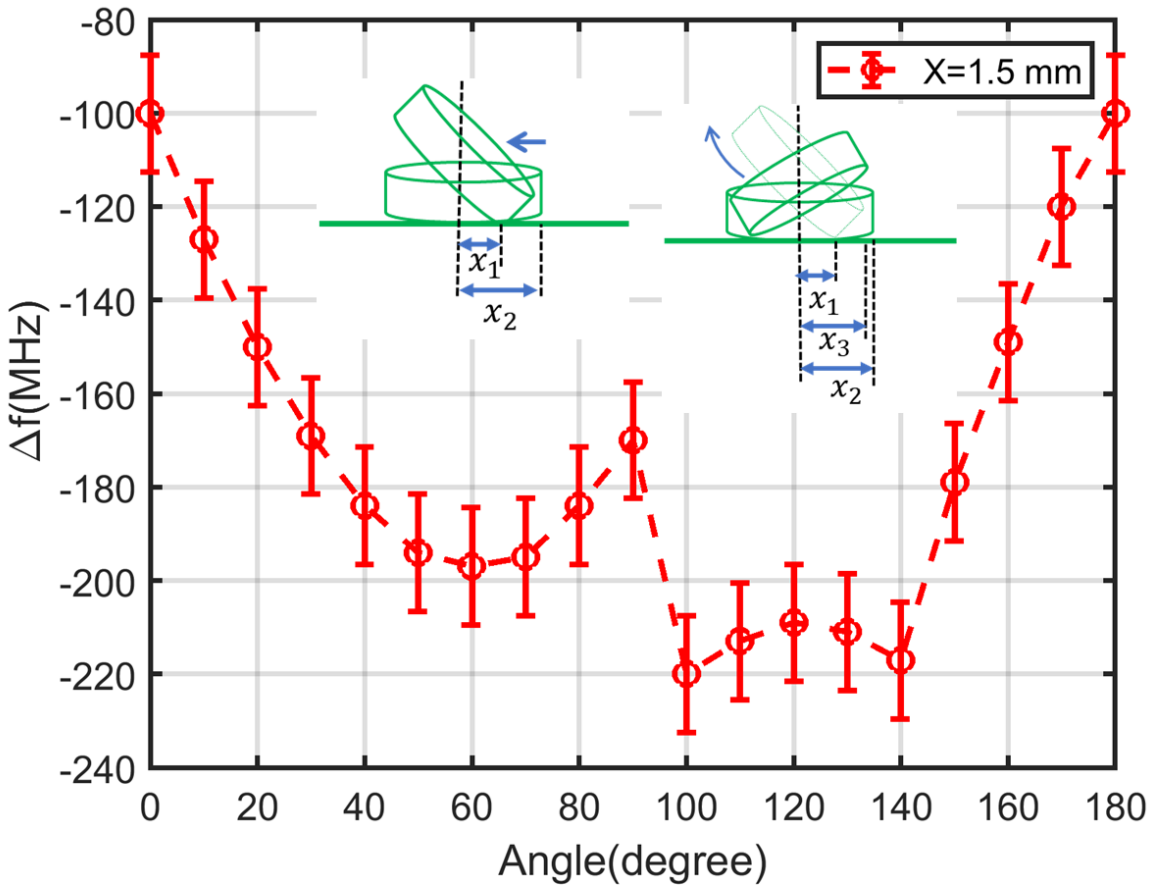


Figure 4.7: Effect of magnetic rotation at the edge of the stub on the frequency of the cavity. The average error bar of 25 MHz is implemented in the graph.

# V. Conclusion

Figure 4.8 generalized shift pattern observed in the FEM simulations. The blue spectra represent the bare cavity frequency. A magnet placed on the stub pulls the frequency of the cavity (orange spectra) down at least by 50 MHz. A magnet, when lifted from the surface of the stub, always increases the cavity's frequency irrespective of its position and angle on the stub (represented by the purple arrow). The effect is drastic at the edge of the stub. The frequency upshift due to magnetic levitation is in the hundred orders larger in magnitude than the frequency upshift when the magnet makes a small angle with the stub (light blue arrow). The frequency goes down when the magnet is pushed off towards the edge of the stub (green arrow).

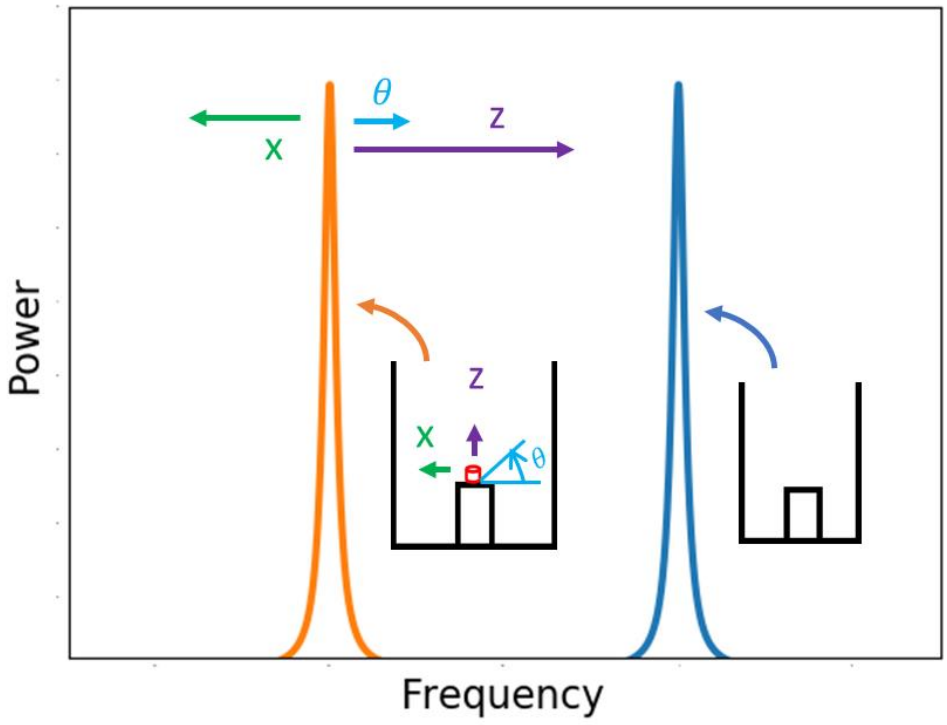


Figure 4.8: Generalized frequency shift pattern for key phenomenon during the levitation experiment.

## 4.4 Quality factor

The quality factor of an empty cavity is discussed in Chapter 2. The surface resistance ($R_s$) is the crucial component to determine the quality factor of the cavity. The surface resistance of the cavity can be divided between two parts: $R_s = R_{\mathrm{BCS}}\,(\mathrm{T}) + R_{\mathrm{Residual}}$. The residual resistance is independent of the temperature. It is dependent upon the input/output coupling, chemical impurity, surface roughness, residual dc magnetic field, etc. [15].

According to the Mattis-Bardeen (M-B) theory, $R_{\mathrm{BCS}}\,(\mathrm{T})$ depends upon the temperature and is approximated as:

$$R_{\mathrm{BCS}}(T) \propto e^{-(\frac{\Delta(0)}{K_B T})}, \tag{4.9}$$

Where $\Delta(0)$ is the energy gap of the superconductor, $K_B$ is Boltzmann constant, and T temperature of the superconducting cavity [59]. The value of $\frac{\Delta(0)}{K_B T_c}$ due to the microwave photon absorption for aluminum is 6 [44].

Figure 4.9 shows the variation of $R_{\mathrm{BCS}}$ as a function of temperature for $\hbar\omega \ll K_B T_c$And $\hbar\omega \ll \Delta(0)$. There is a significant decrease in the surface resistance during the superconducting transition. As the temperature of the superconductor lowers further down, there will be more cooper pair formation. That will lead to a reduction of the surface

resistance. The BCS theory predicts small or no variation of the energy gap below the $\frac{T_c}{2}$. A similar change is seen in the case of the surface resistance as well.

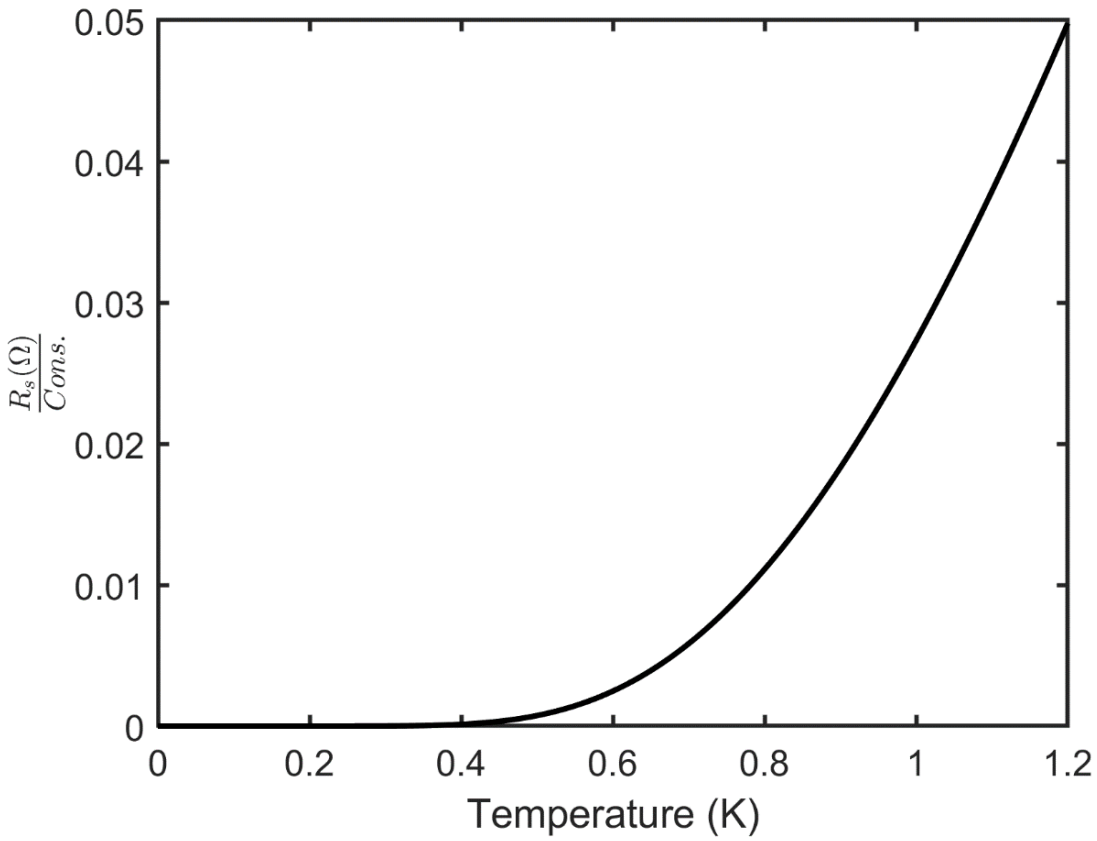


Figure 4.9: Plot of the $\frac{R_{\mathrm{BCS}}}{Constant}\alpha e^{-(\frac{\Delta}{K_B T})}$. Here, the value of $\frac{\Delta}{K_B T_c}$ is equals to 6 [44].

The quality factor of the cavity changes with the presence of the cavity. For an under-coupled cavity, where the contribution of the quality factor is only from the intrinsic quality factor ($Q_{int}$), the presence of a magnet disturbs the mode of the cavity. We have calculated the G-factor 153 using FEM simulation for a cavity with the magnet on the stub, which is 49 percent greater than the G-factor of the empty cavity [41].

Figure 4.10 shows FEM simulations of the G-factor as a function of the position of the magnet on the stub. The effect of the position of the magnet on and above the stub on the G-factor is small. Hence, the contribution of the G-factor in the intrinsic quality factor ($Q_{int}$) due to the magnetic movement is small.

The effect of the magnet and couplers on the quality factor of the cavity can be studied by using the total quality factor. The total quality factor of the cavity is divided between the intrinsic (unloaded, $Q_{int}$) quality factor and external (loaded, $Q_{ext}$) quality factor as $\frac{1}{Q} = \frac{1}{Q_{int}} + \frac{1}{Q_{ext}}$ [33]. The external quality factor includes effects of external contribution such as the coupling (over, under, or critical) of the cavity, and the magnetic perturbations. The

$Q_{ext}$ can be approximated as $\frac{1}{Q_{ext}} \propto \frac{1}{Q_{coupling}} + \frac{1}{Q_{magnet}}$. According to the lump element model, when the external perturbations (such as couplers, a magnet) are introduced into the resonant system the additional resistance ($R_{ext}$) is added in series with the $R_s$ [33]. Hence the external quality factor will be $Q_{ext} = 2\pi f \frac{L}{R_{ext}}$. The total quality factor can be approximated as $Q \propto \frac{2\pi f L}{R_T(=R_s+R_{ext})}$. For a quarter-wave coaxial cylindrical cavity, $L$ is calculated from the expression $\frac{\mu_0 h_{cav}}{2\pi} \ln(\frac{r_{cav}}{r_{stub}})$, where $h_{cav}$ is height of the cavity, $r_{cav}$ radius of the cavity, and $r_{stub}$ is radius of the stub [60].

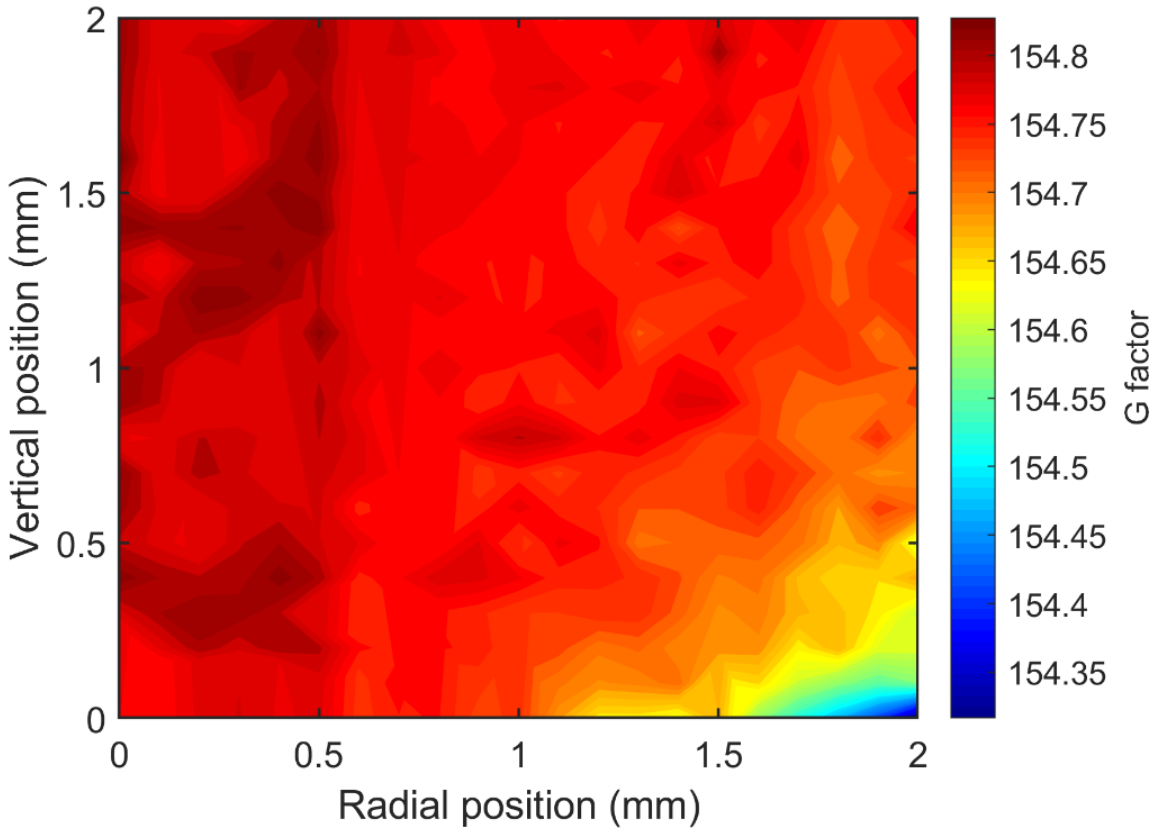


Figure 4.10: Geometric factor of the cavity-magnet system as a function of radial and vertical position of the magnet on the stub.

## 4.5 Levitation Height Calculation

When a magnet is put above a type I superconductor, the magnetic flux is completely expelled from the interior of the superconductor due to the Meissner effect. Here the necessary condition is the applied field is less than the critical field of the superconductor. The boundary condition is that the perpendicular component of the magnetic field will be zero on the superconductor's surface. Based on this boundary condition, different models have been developed to calculate levitation force (or energy). One such model is the mirror method. The mirror method considers the magnet and it's diamagnetic image as a dipole.

However, it does not consider the dimension of either the superconductor or the magnet. A model that is developed by Lugo et al. [61] considered the size of the superconductor. They considered the magnet a point dipole and the superconductor a continuous array of point dipoles. The levitation force (or energy) is then obtained by integrating the dipole-dipole interaction between the real and the image magnet over the volume of the superconductor [61,62]. The main limitation in their calculation is the exclusion of the size of the magnet.

In our study, we have used the two-loop model to calculate the levitation height. This model takes into account the size of both the magnet and the superconductor. The two-loop model calculates levitation height more accurately than the mirror method and the method developed by Lugo et at.

### 4.5.1 Mirror Method

The schematic of the assumption of the mirror method is shown in Fig. 4.11. For the type I superconductor, this model assumes that the magnet on the superconductor has its diamagnetic image inside the superconductor. Both magnets (real and image) move in the opposite direction. The interaction between the magnets is most robust near the superconductor's surface and becomes weaker as it goes farther from the surface.

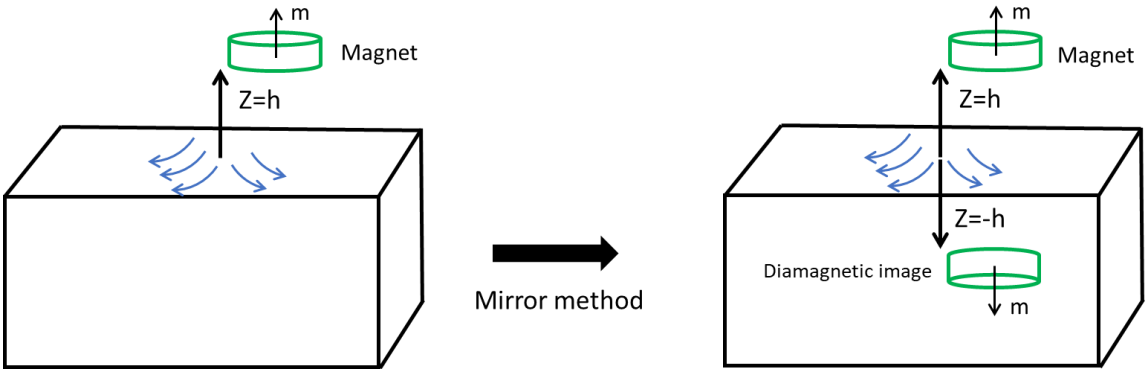


Figure 4.11: The mirror method's schematic view of a magnet at a height h above a superconductor.

The mirror method can calculate the potential energy (or levitation force) calculation. Consider a permanent magnet and its corresponding image as an induced dipole. The potential energy on the magnet due to the induced dipole depends upon the magnetic moment ($\vec{m}$) and magnetic field ($\vec{B}$). Mathematically the potential energy can be written as:

$$\vec{U} = \frac{1}{2}\left(\vec{m} \cdot \vec{B}\ \right) \tag{4.10}$$

We can calculate a magnetic field due to the dipole at the distance z from its center is given by the relation below [63]:

$$\vec{B}(0,\ 0,\ z) = \frac{\mu_0 m}{4\pi}\frac{2}{z^3}\hat{k} \tag{4.11}$$

Substituting the above expression into Eq. (1) results in the potential energy due to the force exerted by the mirror image on the permanent magnet.

$$U(0,0,z) = \frac{\mu_0 m^2}{4\pi}\frac{(1+sin^2\theta)}{(2z)^3} \tag{4.12}$$

Here, $(1+sin^2(\theta))$ takes account of the angle of the magnet with the superconductor and (2z) is the distance between the real and image magnet. The potential energy due to the radially magnetized magnet is half that of the axially polarized magnet. The total potential energy includes the gravitational ($Mgz$) potential energy as well.

$$U_{total}(0,0,z) = \frac{\mu_0 m^2}{4\pi}\frac{(1+sin^2\theta)}{(2z)^3} + Mgz \tag{4.13}$$

The above expression for the potential energy assumes the magnetic field is completely expelled from the superconductor, an infinite plane. The magnet levitates at the point with the least potential above the superconductor [64].

Equation 4.13 is plotted for an axially magnetized N52 permanent neodymium magnet of a radius and height of 0.5 mm in Figure 4.12. Here $\theta = 90°$ is used. The total potential energy near the superconductor is high because of the large repulsion between the magnet and its diamagnet image. As the magnet moves farther away from the superconductor's surface, the potential energy quickly falls off. Its value becomes minimum at 3.8 mm above the superconductor. Hence, the magnet levitates at this minimum energy point.

The levitation force than can be calculated as [64]:

$$F_{Lev}(0,0,z) = -\Delta U_{Lev}$$
$$F_{Lev}(0,0,z) = \frac{6\mu_0 m^2}{4\pi}\frac{(1+sin^2\theta)}{(2z)^4} \tag{4.14}$$

The vertical stiffness can be derived from equation (4.14) as:

$$K_z = -\frac{\partial F_{Lev}(0,0,z)}{\partial Z}$$
$$= \frac{48\mu_0 m^2}{4\pi}\frac{(1+sin^2\theta)}{(2z)^5} \tag{4.15}$$

This will lead to the resonance frequency of:

$$\omega_z = \sqrt{\frac{K_z}{M}}$$
$$\omega_z = m\sqrt{\frac{3\mu_0(1+sin^2\theta)}{8\pi * M}\frac{1}{{z_0}^5}}$$

$$\omega_z = \sqrt{\frac{4g}{z_0}} \tag{4.16}$$

For, an N52 neodymium magnet of mass (M) 2.75 *milligram* and magnetic moment (m) 0.46 *(mA)m*$^2$ levitating at a distance 3.8 *mm* above the superconductor $f_z$ will be ≈11 *Hz*.

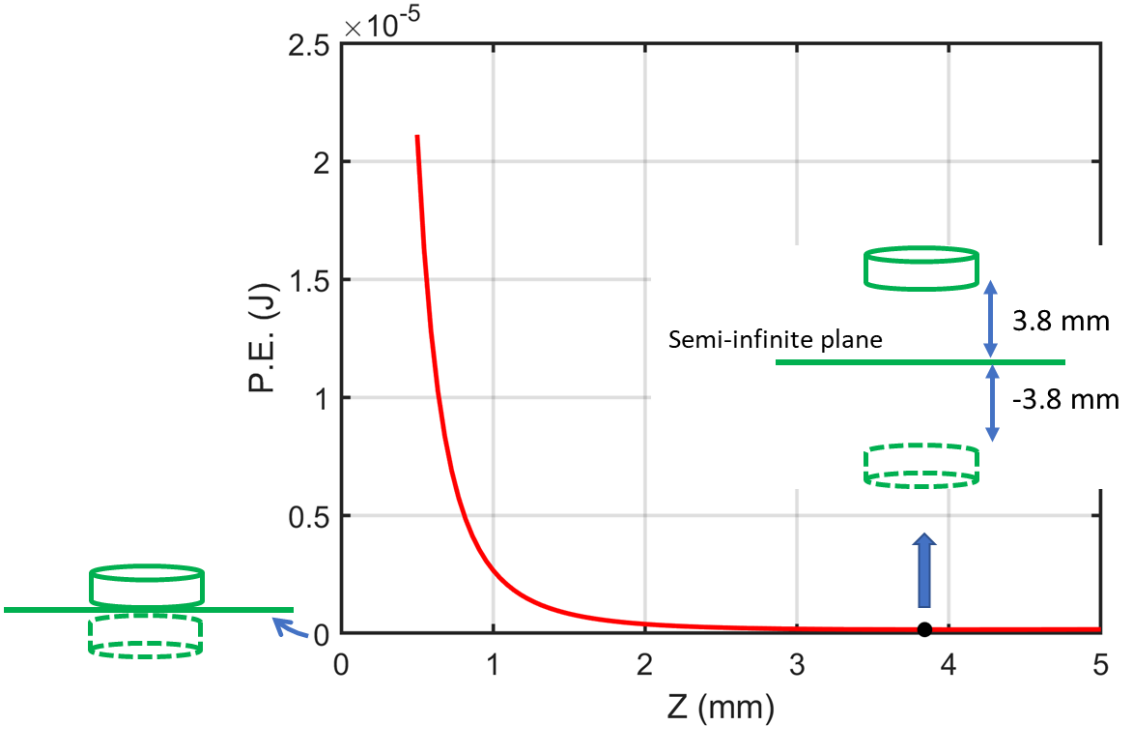


Figure 4.12: Total potential energy as a function of the vertical position of the magnet. The calculation starts from 0.5 mm vertical height. The substantial repulsion between the real and image magnets results in enormous energy in this distance.

### 4.5.2 Finite-Size Superconductor

The main drawback of the mirror method is that it considers the superconductor as an infinite size. The approach that Lugo et al. [61] took considered the size of the superconductor in their calculation. The levitation force due to a superconducting cylindrical of radius R and thickness t, can be written as:

$$F_{Lev} = \frac{\mu_0}{4\pi}\frac{3m^2(1+sin^2\theta)}{32}[f(a)-f(a+t)] \tag{4.17}$$

Where:

$$f(z) = \frac{1}{z^4} - \frac{5R^2+3z^2}{3(R^2+z^2)^3} \tag{4.18}$$

In Figure 4.13, levitation force is calculated as a function of the vertical position of the magnet of the same dimension and strength that have been used for Fig. 4.12 generation. For the size of the superconductor, the dimension of the stub, $R = 2\ mm$, and $t = 5\ mm$,

is used. The levitation force balances the gravitational force at 2.75 mm above the superconductor. This value is 28 percent smaller than the levitation height predicted by the mirror method.

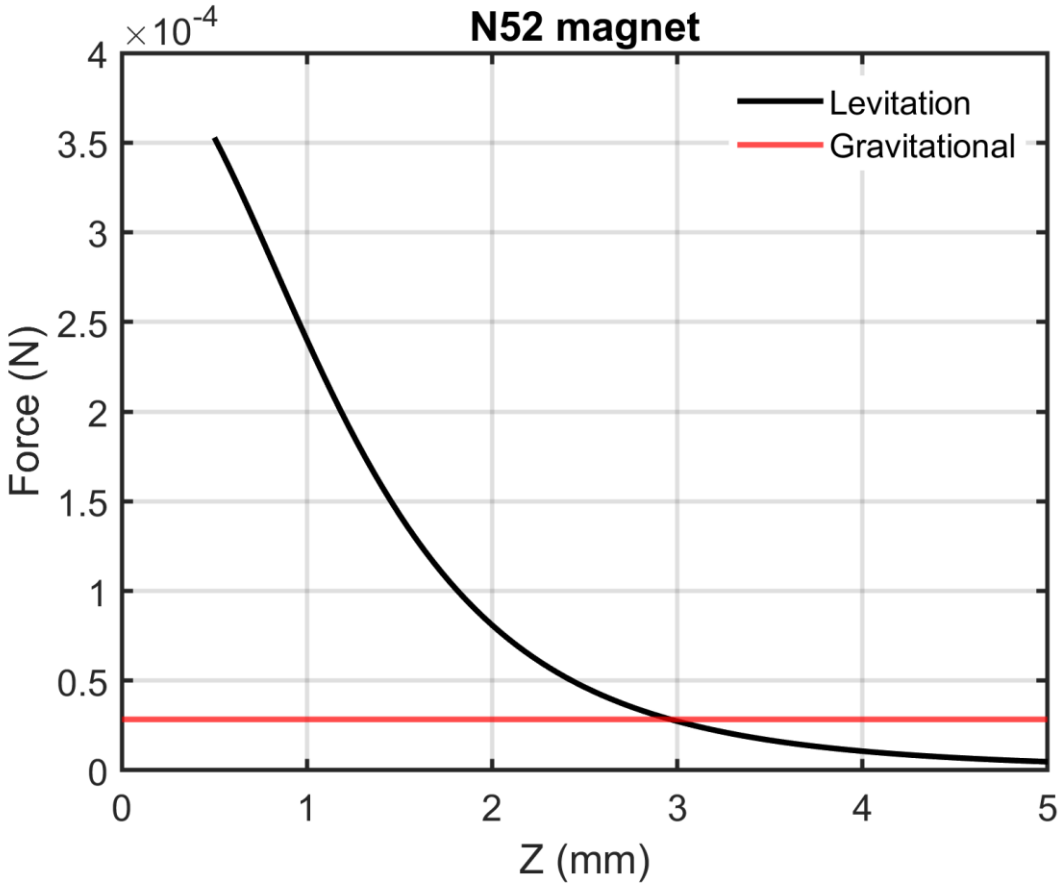


Figure 4.13: Levitation force for a finite-size superconductor. Here, 0.25 mm (half the thickness of the magnet) is subtracted from 3 mm to get levitation height from the surface of the superconductor to the surface of the magnet. The upward levitation force balances the downward gravitational force at 2.75 mm.

### 4.5.3 Two-loop model

In our experiment, the axis of the magnet does not necessarily coincide with the axis of the superconductor. Similarly, the size of the magnet is comparable to the size of the superconductor. Therefore, the methods discussed above result in highly inaccurate levitation height calculations.

We have used a two-loop model to calculate levitation height for the magnetic levitation from the stub of the cavity. As shown in Figure 4.14, the magnet and its image are considered two current loops in this model. Their distance is taken from the center of mass of the magnet. Let us suppose the magnet has a radius and height of $R_M$ and $h$, respectively. Similarly, the superconducting stub has a radius of $R_S$ and thickness of $t$. In the two-loop

model, the magnet is replaced by a loop of current with the same radius as a magnet. Also, a loop of current replaces the image magnet with a radius equal to the radius of the superconductor. The distance between the two loops is now $2Z + h$ instead of $2Z$ between two magnets.

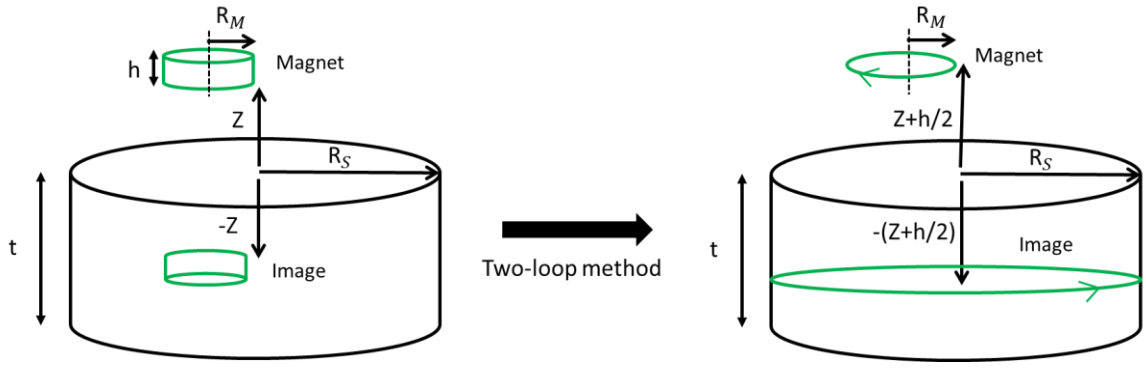


Figure 4.14: Two-loop representation of the magnet and its image. Here, the magnet and its image are replaced by current-carrying loops in the opposite direction.

Now, let's calculate the magnetic field due to the two loops. The vector potential has only an azimuthal component, which is given by the equation:

$$A_{\emptyset} = \frac{\mu_0}{4\pi}[(R_S + r)^2 + z^2]^{\frac{1}{2}} . [\left(1 - \frac{1}{2}k^2\right) . K(k) - E(k)] \tag{4.19}$$

Where:

$$k(r) = \frac{4R_S r}{(R_S + r)^2 + z^2} \tag{4.20}$$

$$r = [(R_M cos\emptyset_2 + y)^2 + (R_M sin\emptyset_2)^2]^{\frac{1}{2}} \tag{4.21}$$

$$R = [{R_S}^2 + r^2 + z^2 - 2R_S r cos\emptyset_1]^{\frac{1}{2}} \tag{4.22}$$

Using, relation $B = \nabla \times A$, we get:

$$B_z = \frac{\mu_0 I}{4\pi[(R_S + r)^2 + z^2]^{\frac{1}{2}}}[\frac{{R_S}^2 - r^2 - z^2}{(R_S - r)^2 + z^2]} . E(k) + K(k)] \tag{4.23}$$

$$B_r = \frac{\mu_0 I z}{4\pi r[(R_S + r)^2 + z^2]^{\frac{1}{2}}}[\frac{{R_S}^2 + r^2 + z^2}{(R_S - r)^2 + z^2]} . E(k) - K(k)] \tag{4.24}$$

$$B_{\emptyset} = 0 \tag{4.25}$$

$$m = \pi I {R_S}^2 \tag{4.26}$$

From the frame of reference of the magnet, the components of the magnetic field will be:

$$B_{r|x'-y'-z'} = B_{r|x-y-z}\cos\left(\tan^{-1}\left(\frac{R_M sin\emptyset_2}{y + R_M cos\emptyset_2}\right) - \emptyset_2\right) \tag{4.27}$$

$$B_{\emptyset|x'-y'-z'} = B_{\emptyset|x-y-z}\sin\left(\tan^{-1}\left(\frac{R_M sin\emptyset_2}{y + R_M cos\emptyset_2}\right) - \emptyset_2\right) \tag{4.28}$$

Now potential energy will be the dot product of the magnetic moment of the magnet () and response field from the image magnet:

$$\vec{U} = \frac{1}{2}\left(\vec{m} \cdot \overrightarrow{B_Z}\right)$$

Using equation (4.23) in the above equation results (we are only taking the magnitude of the potential energy here):

$$U = \frac{\mu_0 Im}{4\pi[(R_S + r)^2 + z^2]^{\frac{1}{2}}}\left[\frac{{R_S}^2 - r^2 - z^2}{(R_S - r)^2 + z^2}.E(k) + K(k)\right] \tag{4.29}$$

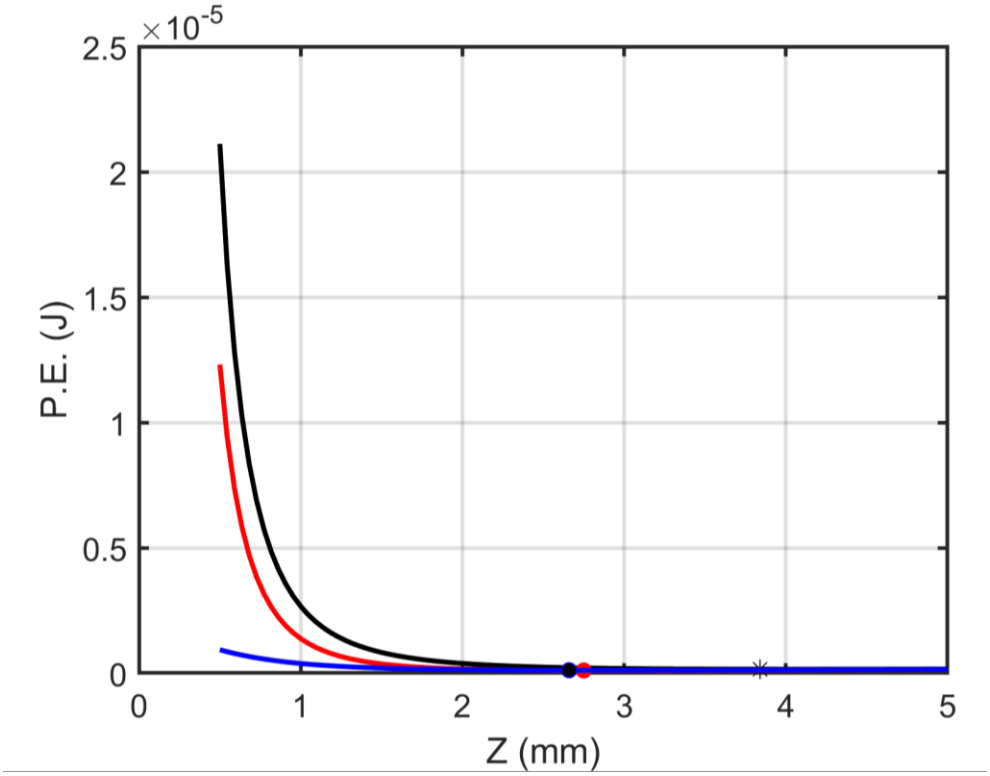


Figure 4.15: Comparison of the potential energy calculated at the center of the superconductor using three models: the mirror, finite-size superconductor, and two-loop model.

The potential energy calculated from the two-loop model is compared with the potential energy calculated by using the mirror method and finite-size superconductor in Figure 4.15. There is a large discrepancy of energy between the energy calculated by the former approach and that calculated from the latter two methods near the surface of the superconductor. The main reason for such a large discrepancy is that the two-loop model more accurately takes account of the size of the superconductor and the magnet. The difference reduced significantly with the increasing vertical position (z) of the magnet.

Furthermore, the two-loop model calculates levitation height more accurately than the other two models. As shown in Figure 4.15 (see three markers), it calculates the levitation height 2.65 *mm*. It is smaller than the value predicts by the mirror method (3.8 *mm*) and the finite SC method (2.75 *mm*). The mirror method and finite-size superconductor overestimate the levitation height, respectively, by 31 and 4 percent.

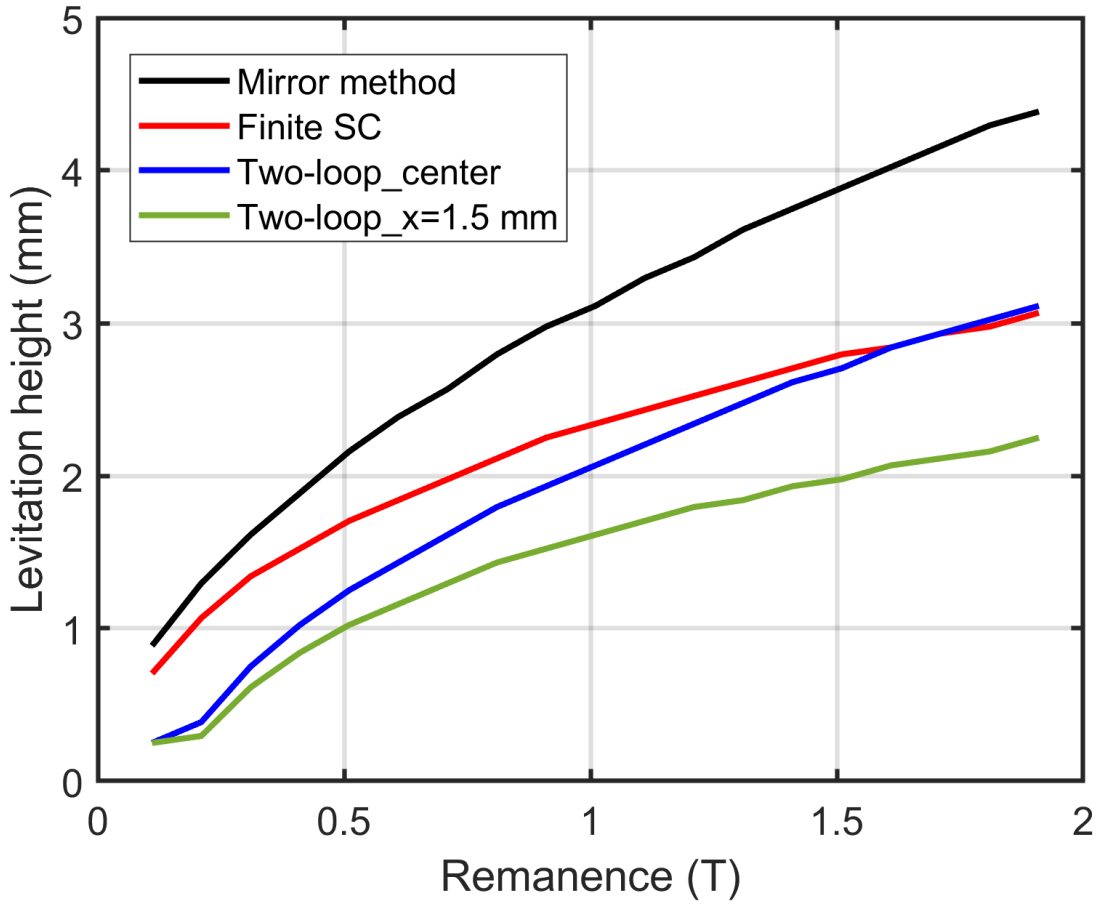


Figure 4.16: Levitation height as a function of remanence of the magnet. Three models (mirror, finite SC, and two-loop) are compared at the center and edge of the superconductor.

Figure 4.16 compares levitation height between the three models as a function of the strength of the magnet. In all three models, a common trend is levitation height increases

with the strength of the magnet. The stronger magnet produces the stronger image magnet. Hence, the larger levitation force results in a larger levitation height.

The significant difference in levitation height calculations between the three models comes from the weaker magnets ($B_r < 1\,T$) at the center of the superconductor. The difference between the finite SC and two-loop model gets smaller as remanence goes higher than 1 T, reaching zero above 1.5 T. However, the deviation of the mirror method calculations always remains with the finite SC & two-loop model.

The fundamental difference between the mirror method and finite SC with the two-loop model appears at the edge of the superconductor. The mirror and finite SC model considers only the coaxial superconductor-magnet case, where the magnet's axis coincides with the axis of the superconductor. However, levitation height is reduced as the magnet moves from the center to the edge of the superconductor. For example, according to the two-loop model, for the magnet with a strength of 1.5 T, the levitation height is reduced from 2.7 mm to 2 mm as we go from the center to the edge of the superconductor. The main reason is the reduction of the response supercurrent at the edge of the superconductor than that at its center. Only the two-loop model takes account of this change.

### 4.5.4 Stable Magnetic Levitation

An example configuration of a 3D cavity that we have used in our experiment is shown in Figure 4.17. This cavity is made from 6061 aluminum, a type I superconductor. A magnet is put on the stub of the cavity. The aspect ratio of the stub and magnet is 4:1 (ratio of the radius of the superconductor to the radius of the magnet). The dimension of the wall and floor of the cavity are large compared to the dimension of the magnet. Due to its large size, the wall and the cavity floor can be considered a semi-infinite plane.

We have implemented a hybrid technique for the potential energy calculation by combining the two-loop and the mirror method. Two- loop model is used for the interaction between the magnet and stub. Whereas in the case of the magnet and wall interaction, the mirror method is used. The potential energy for such a cavity-magnet system will be:

$$U_{total} = U_{two-loop} + U_{Mirror} + U_{Gravitaitonal} \tag{4.30}$$

$$U_{total} = \frac{\mu_0 Im}{2\pi[(R_S + r)^2 + h^2]^{\frac{1}{2}}}\left[\frac{{R_S}^2 - r^2 - h^2}{(R_S - r)^2 + h^2]}.E(k) + K(k)\right] + \frac{\mu_0 m^2}{4\pi}\frac{(1 + sin^2\theta)}{16(d - x)^3} + Mgh \tag{4.31}$$

Here, $2h$ is the distance between the magnet and its diamagnetic image, $I$ is the response supercurrent.

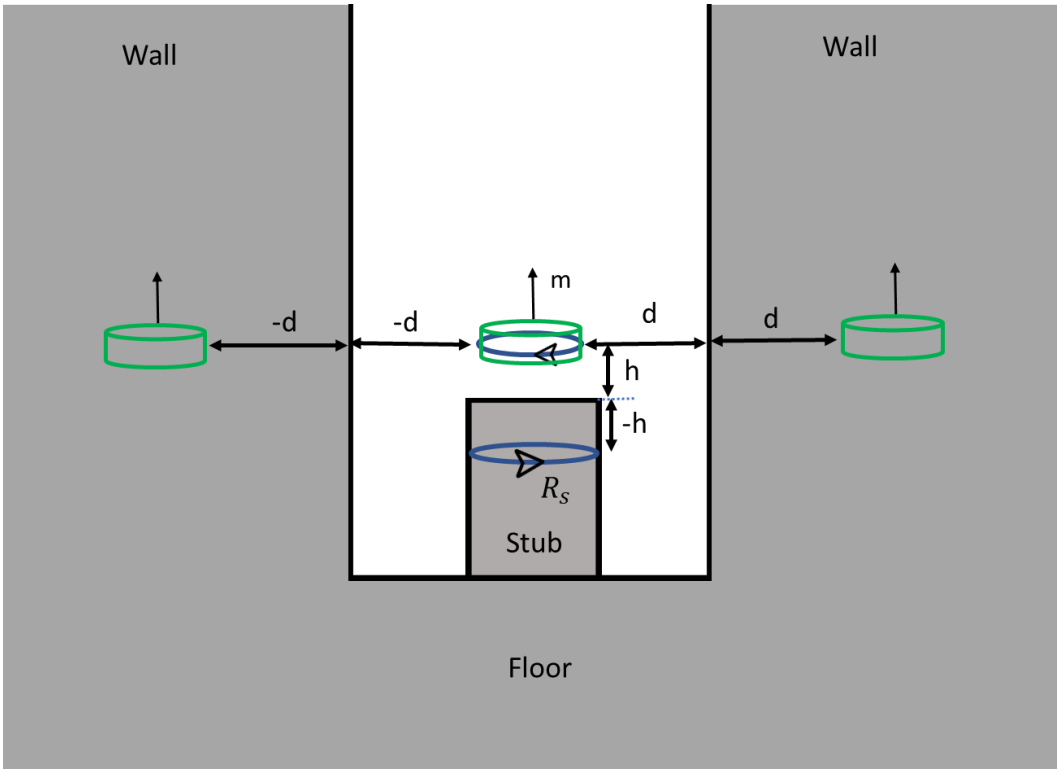


Figure 4.17: A 3D cavity configuration. This configuration has the dimension same as the cavity we are using in our experiment.

Figure 4.18 shows a contour plot of the potential energy of the 3D cavity. The origin of the coordinate is considered at the center of the stub. The calculation is done in the positive direction. The cavity is symmetric. Hence, the nature of the potential energy will be symmetric as well.

In the calculation, the minimum potential energy of the cavity is found, as shown in Figure 4.18, at $(x, z = 3.5\ mm, 2.1\ mm)$. In other words, the minimum potential energy is at the center of the cavity gap. One advantage of knowing this local potential energy minima is that we see a magnet on the surface of the stub will be pushed towards this point when the stub and the cavity go into the Meissner transition. Therefore, it will fall on the bottom of the cavity. There needs to be some external resistance to keep the magnet on the stub [65]. One can fit a plastic sleeve on the stub for that purpose. The drop in quality factor would be the price to pay in exchange for that.

There will be two ways to pursue stable magnetic levitation on a 3D cavity configuration stub. First, one can change the gap of the cavity. The second option will be a modification in the configuration and strength of the magnet. The following sub-section discusses these two ways of achieving stable magnetic levitation.

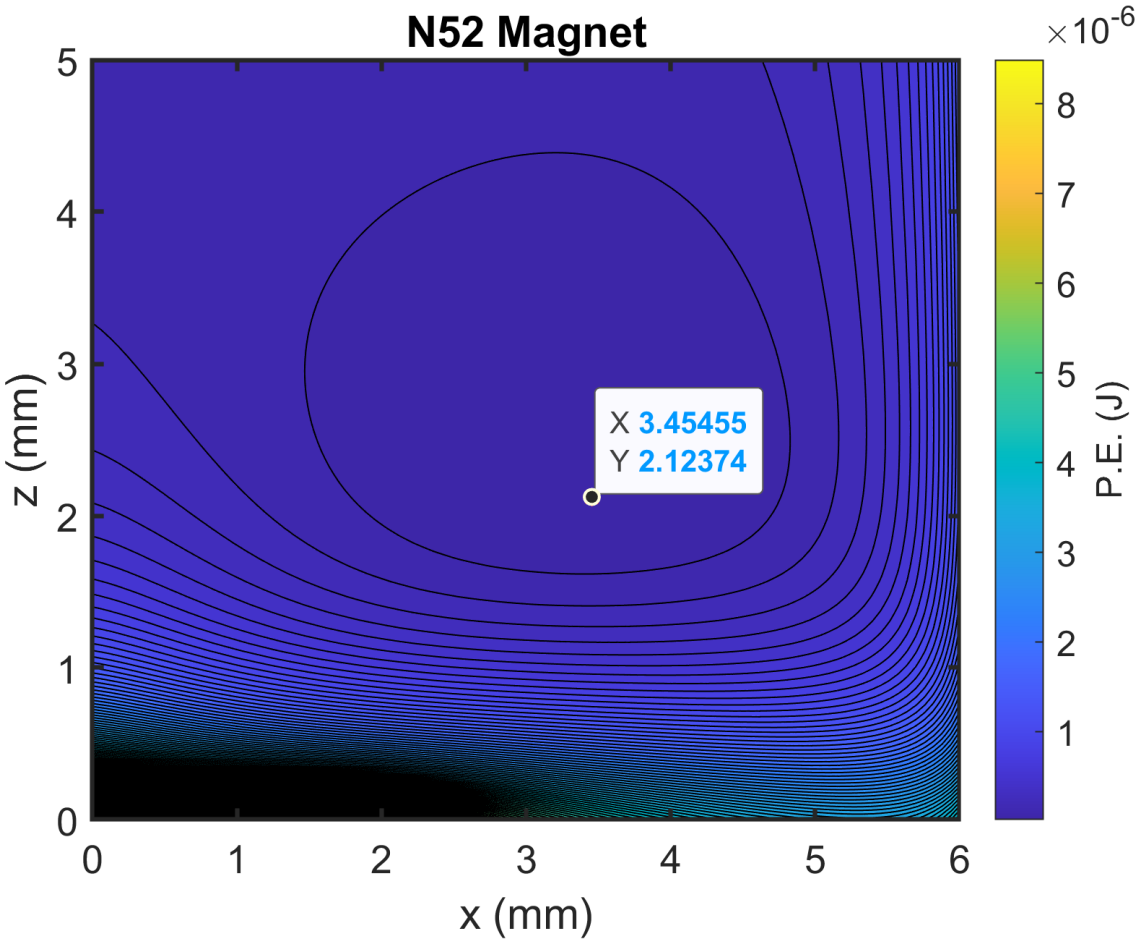


Figure 4.18: Potential energy calculated as a function of radial and vertical position of the magnet. The calculation is done for the positive direction from the center of the cavity.

#### 4.5.4.1 Cavity Configuration

The first option to go for the stable magnetic levitation within a 3D superconducting cavity is to reduce the gap between the stub and the wall of the cavity. The force from the wall to the magnet increase with $\propto \frac{1}{z^4}$ (see equation (4.14)). Figure 4.19 calculates minimum potential in the radial distance for the gap size from 5-2 mm using equation (4.31). When the gap is 3 mm, the magnet on the stub sees the least potential in the center of the stub and the wall. In quest of going into the least energy point, it falls on the gap of the cavity. If the gap is reduced to $\leq$ 2.5 mm, the minimum potential point lies well within the stub. At this gap, the magnet can stably levitate on the stub without falling into the gap.

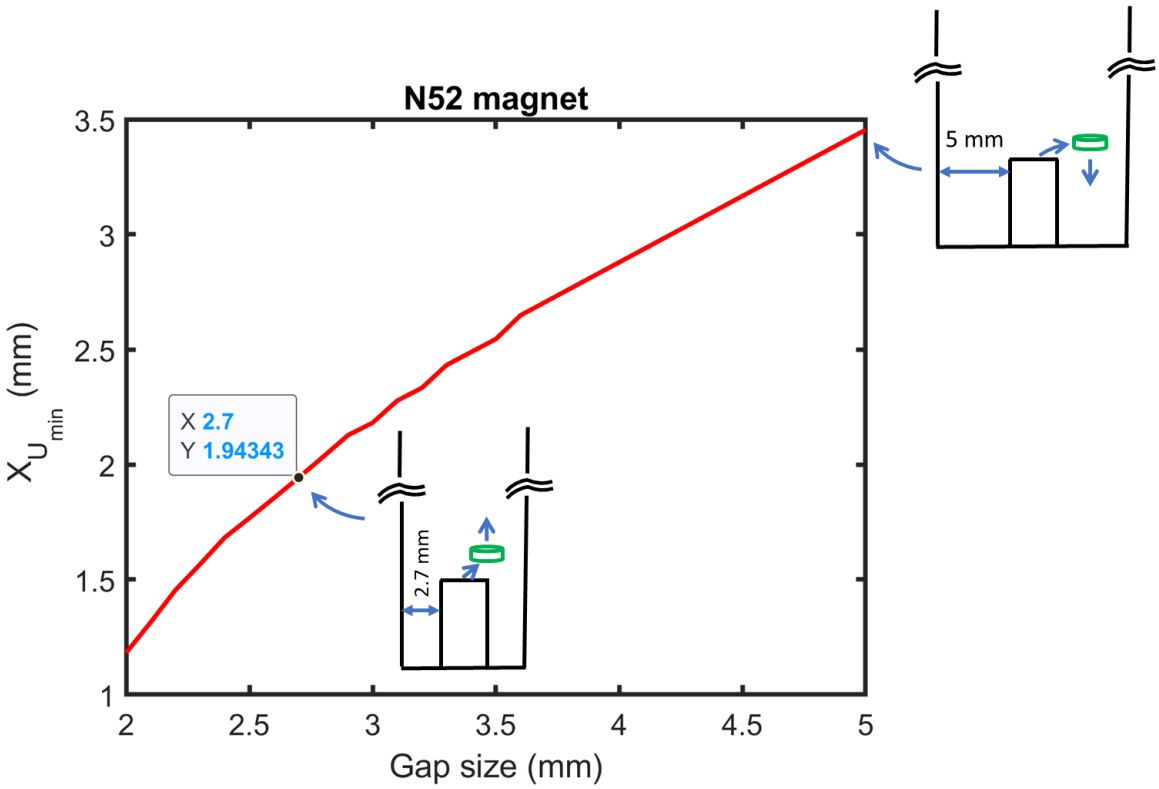


Figure 4.19: Variation in the gap size of the 3D cavity configuration for the stable magnetic levitation.

### 4.5.4.2 Configuration of the Magnet

The magnet's strength, orientation, and size also play a role in stable magnetic levitation. Here, we have studied how each factor affects the levitation. The same size of the magnet, 0.5 mm of the radius and 0.5 mm of diameter, as discussed in the above analysis is used.

#### I. Strength

The strength of the magnet refers to its remanence field. A study of the remanence field effect on the radial and vertical position of magnetic levitation is presented in Figure 4.20. The magnet is axially and radially magnetized. The remanence field is varied from 0 to 2 T.

For both axially and radially polarized magnets, the minimum energy lies on the gap of the cavity. In such a cavity configuration, the magnet then falls on the gap and hence on the bottom of the cavity. Although, the magnet will be pushed towards the gap, the radially polarized magnets have improved location of the levitation. Such magnets moved the radial position from 3.5 mm to 2.5 mm. Remember that the radius of the stub is 2 mm. This point is only 0.5 mm outside of the stub.

In the case of the vertical levitation distance, an increasing trend with the strength of the magnet is seen for both cases of magnetization. The radially polarized magnets have shown

it at the lower height. The reason being induction of a weaker diamagnetic image when the magnetic moment is parallel to the superconducting axis providing a weaker lifting force.

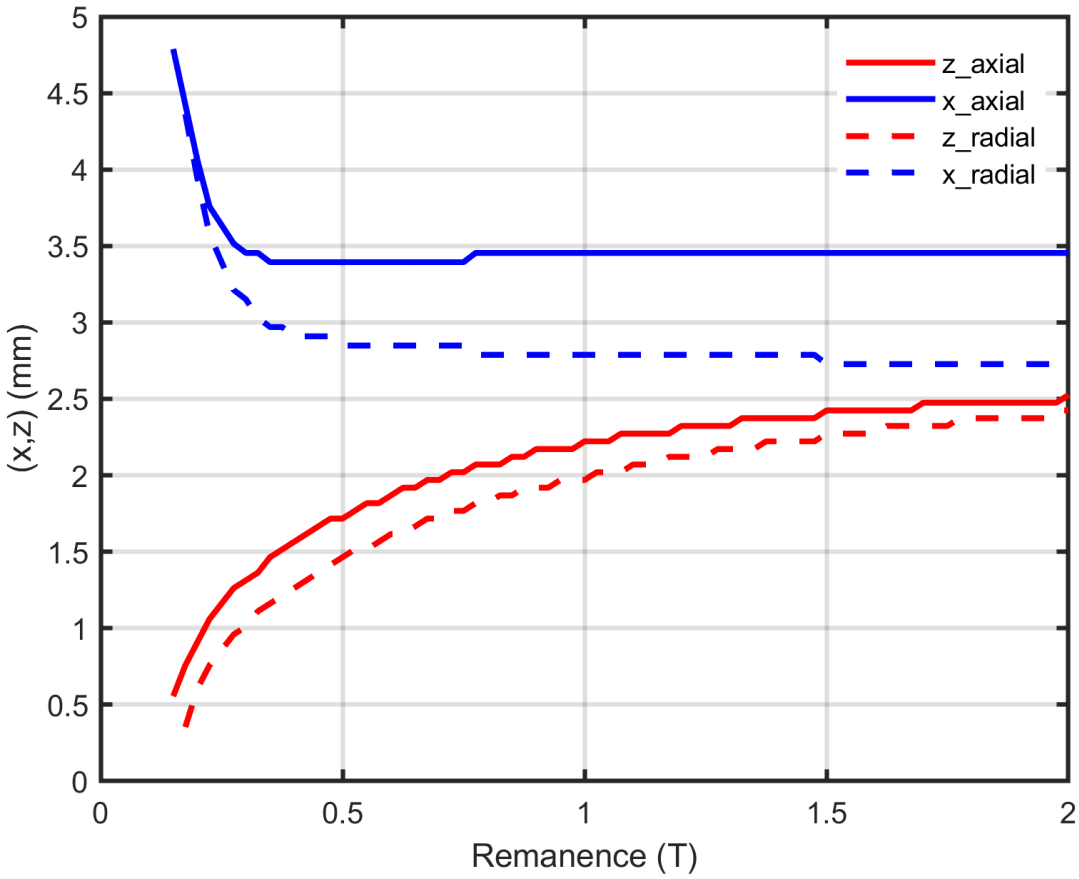


Figure 4.20: Study of radial and vertical position of magnetic levitation for an axially and radially magnetized magnet with strength ranging from 0 to 2 T.

## II. Orientation

The orientation of the magnet is changed from zero degrees to 90 degrees with respect to the stub by keeping the strength of the magnet constant to 1.47 T. The potential energy above the stub is calculated for those angles. The axially polarized magnet is used for the calculations. The vertical and radial position is extracted from the minimum energy state and plotted in Figure 4.21.

As the angle of the magnet is changed from zero degrees to 90 degrees, the radial position of the magnet is shifted from 2.8 mm to 3.5 mm. This is a 25 percent push for a magnet in the radial n from its original position. The angles have less effect on the lifting height. During the flip of the magnet (zero degrees to 90 degrees), the levitation height is changed only by 9 percent.

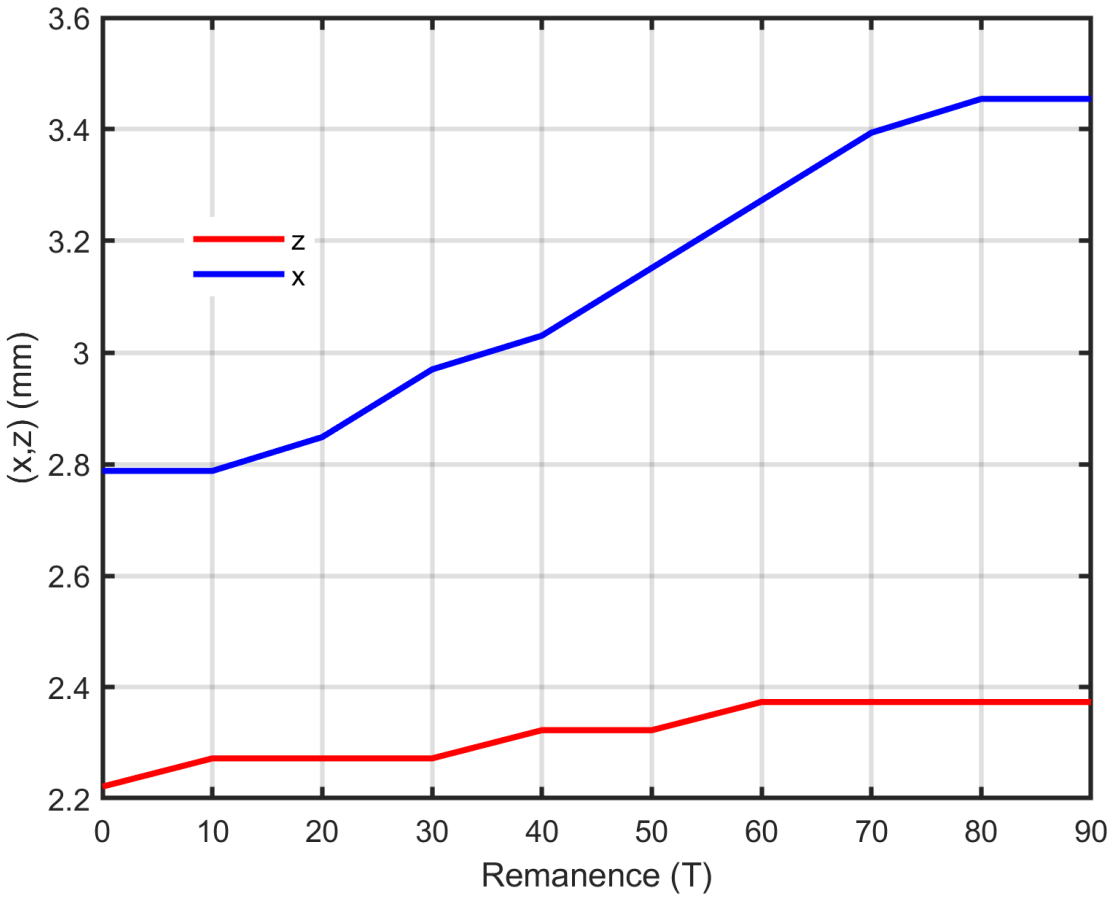


Figure 4.21: Location of the magnet moves when the magnet changes its angle during magnetic levitation. The magnet is N52 and is polarized in the axial direction.

## III. Size

The other important factor to consider for stable magnetic levitation is the size of the magnet. The variation in the radius or thickness of the magnet changes its volume. The volume itself changes with the square of the radius of the magnet and is proportional to its thickness. If the dimension of the magnet is changed by keeping its strength the same, there will be a change in two important factors that determines the levitation force. First, when the volume of the magnet changes, it changes the field on the surface of the magnet too. Second, the volume of the diamagnetic image varies proportionally to the magnet's volume.

Figure 4.22 shows the radial position of magnetic levitation as a function of the dimension of the magnet. The radius of the magnet is varied from 0.5 mm to 1.5 mm. Similarly, the thickness is varied from 0.5 mm to 0.75 mm. The change in the radial position is seen for the magnet with a larger thickness. For example, suppose the size of the present magnet that has a radius and thickness of 0.5 mm is scaled up to a radius of 1.5 mm and a thickness of 0.75 mm. In that case, the radial position of magnetic levitation will shift towards the stub (2.5 mm) from the center of the gap (3.5 mm).

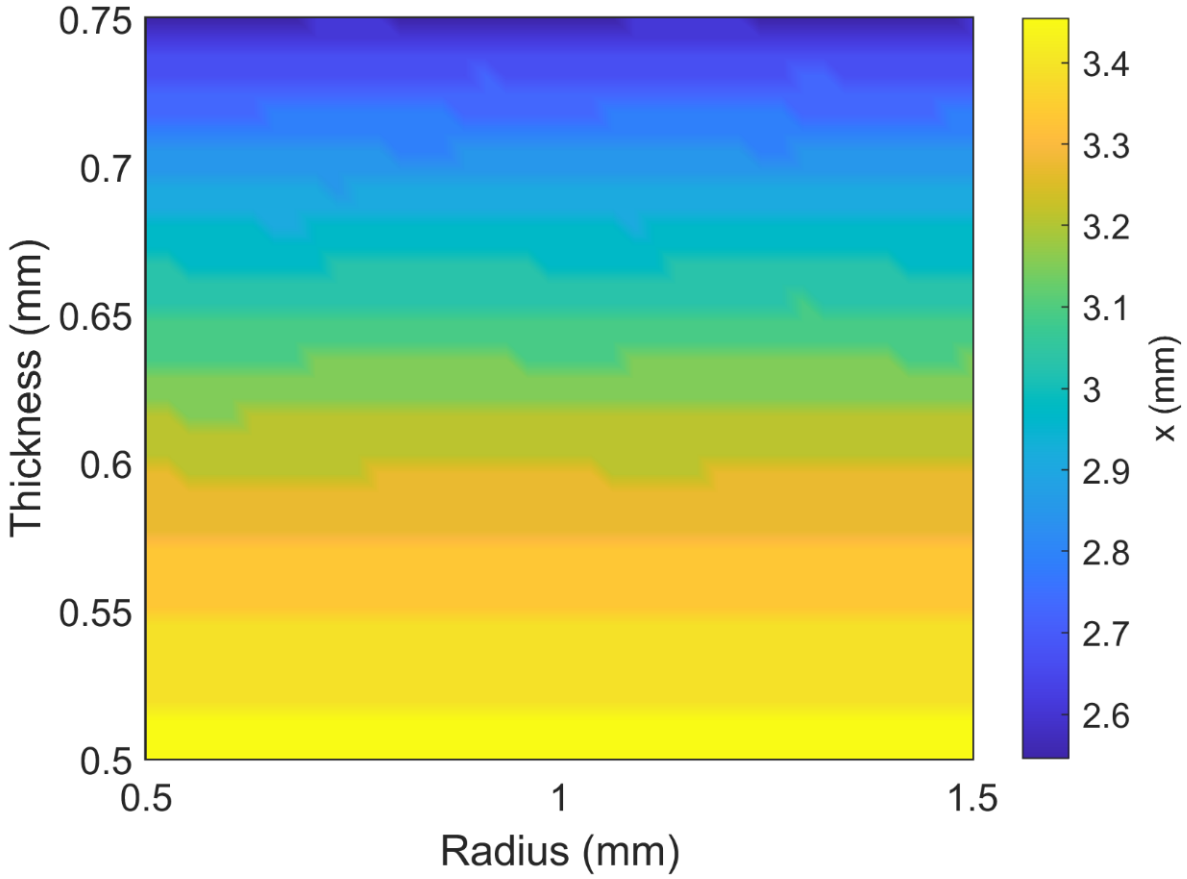


Figure 4.22: The present magnet's dimensions (0.5 mm of a radius and thickness) are scaled up to see its effect on the radial location of magnetic levitation. The strength of the magnet is kept constant at 1.47 T.

## 4.6 Superconducting-Normal Region

A strong magnet sitting on the surface of a superconductor creates a normal region beneath its surface. The normal region extends to the point where the field of the magnet is less than the critical field of the superconductor [66]. For example, the critical field of the superconducting aluminum is 100 gauss. As shown in Figure 4.23, a strong N52 magnet sitting on the top of the stub makes some part of the stub normal, while the rest is superconducting. The critical field of the superconducting aluminum increases as the temperature, $T$, falls according to $B_c(T) = B_0(1 - \frac{T^2}{{T_c}^2})$, here $B_0 = 0.01$ T is the critical field maximum of aluminum at zero temperature and $T_c$ is the zero-field transition temperature. The normal region shrinks as the superconductor gets colder. The depth of the normal region is referred to here as a normal depth.

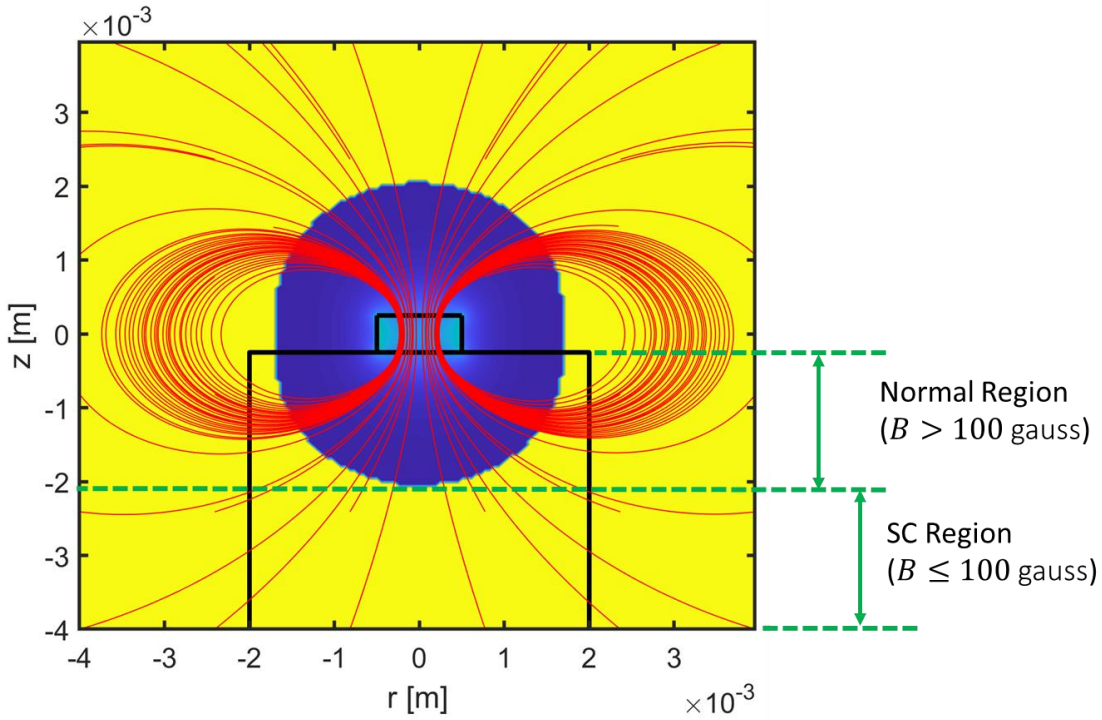


Figure 4.23: The onset strong magnet field creates a normal region below the stub, represented by the blue color. The magnet divides the stub into a superconducting and a normal region.

Figure 4.24 compares the normal depth with the levitation height as a function of the remanence of the magnet. The normal depth is extracted using equation (4.2). For a given strength of the magnet, the intersection between the line $y = 0.01$ T and equation (4.2) is considered as the normal depth. For the levitation height, the two-loop model is used. The magnet is axially magnetized in both calculations.
An intersection between the depth of the normal region and the levitation height is seen for the magnet of strength 0.23 T. The normal depth of the magnet weaker than 0.23 T is greater than the levitation height. There will be no magnetic levitation in this range of the weaker magnets. For the magnet stronger than 0.23 T, the levitation height is greater than that of the levitation height. The diamagnetic image will be created outside of the normal region for these types of magnets. Therefore, the real image experiences force from its image magnet. When the upward pushing levitation force is greater than the downward acting gravitation force, the magnet lifts from the surface of the superconductor.

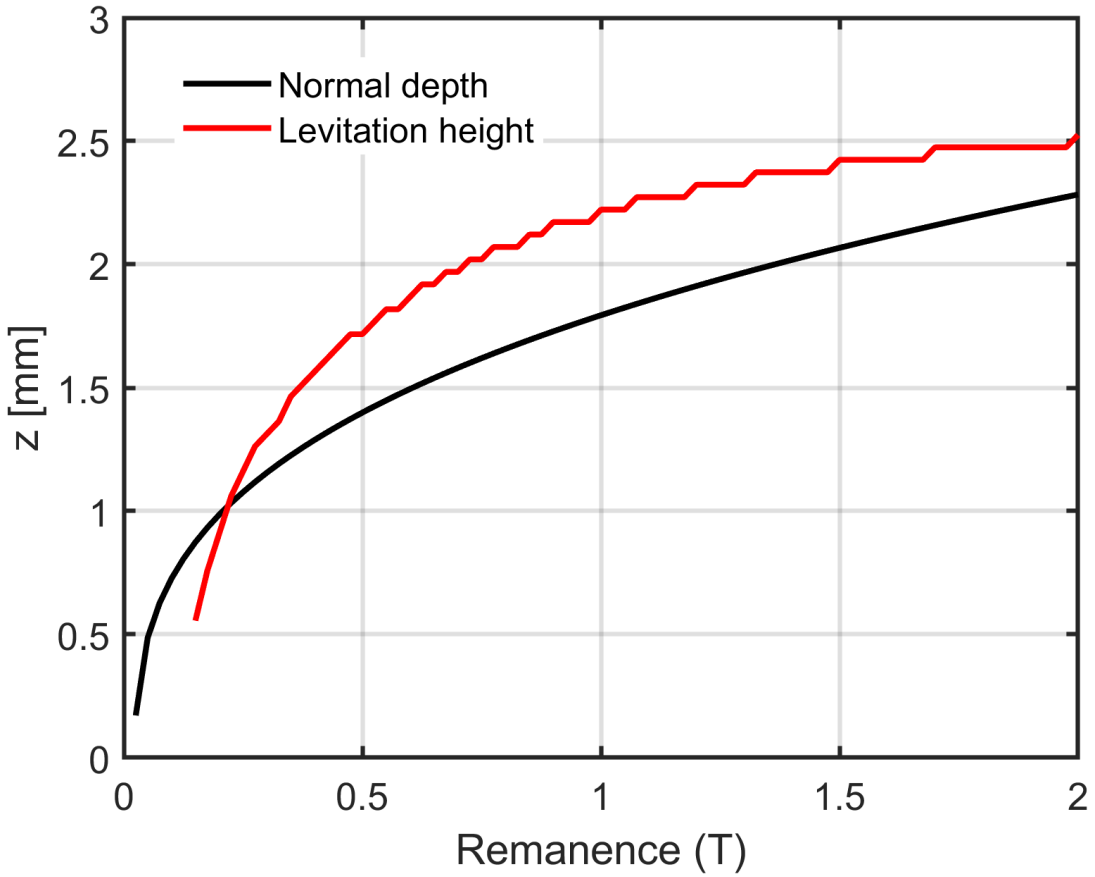

Figure 4.24: The normal depth and levitation height are compared for the range of magnets from 0-2 T. The normal depth is considered where $B > 100$ gauss for a superconducting aluminum at 1.2 K.

# Chapter 5

# Results and Discussions

*"Give, even if you only have a little."*-Buddha

Part of the work presented in this section is published in IEEE Transactions on Applied Superconductivity [57] and some part of it is also submitted for publication [5].

## 5.1 Room Temperature Measurements

### 5.1.1. Introduction

To understand the expected frequency shifts when levitation occurs, the resonance frequency of the cavity is measured as a function of the position of a magnet in the cavity at room temperature. Figure 5.1 shows a schematic of room temperature measurements. Measurements are taken by putting a magnet inside a capillary tube and by sealing its end by a tape and factoring out the effect of the capillary. The capillary tube with the magnet is positioned at different coordinates inside the cavity by the translational stage of the micrometer. The magnet was held in a dielectric capillary and its position was controlled using micrometer stages.

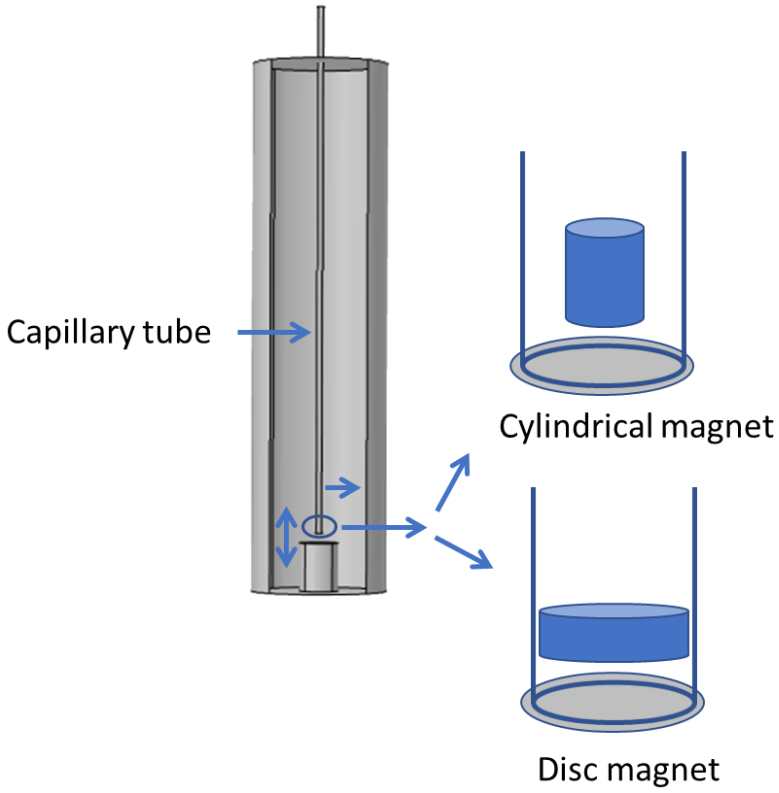


Figure 5.1: Schematic of the room temperature measurements. The measurements are performed on and around the stub and bottom of the cavity. Two types of magnets are used

in the experiment: a cylindrical and disc magnet. The disc magnet is the same that is discussed in the previous chapter. The cylinder magnet has a radius of 0.375 mm and a height of 1 mm.

### 5.1.2. Cylindrical Magnet

The stub is scanned by moving the magnet inside the capillary tube in the radial direction. The change in cavity resonance as a function of the magnet's lateral position is illustrated in Figure 5.2. Each curve represents a different vertical position, and the horizontal axis is the radial distance from the cylinder's axis. The origin of the coordinate is the center of the stub. The cavity resonance is more sensitive to the magnet's position when it is located above the stub (|x|<2.5 mm) than above the gap (|x|>2.5 mm) with the region of highest sensitivity near the stub's edge (|x|~1.5 mm). We attribute the asymmetry in the frequency shift with x to machining imperfections.

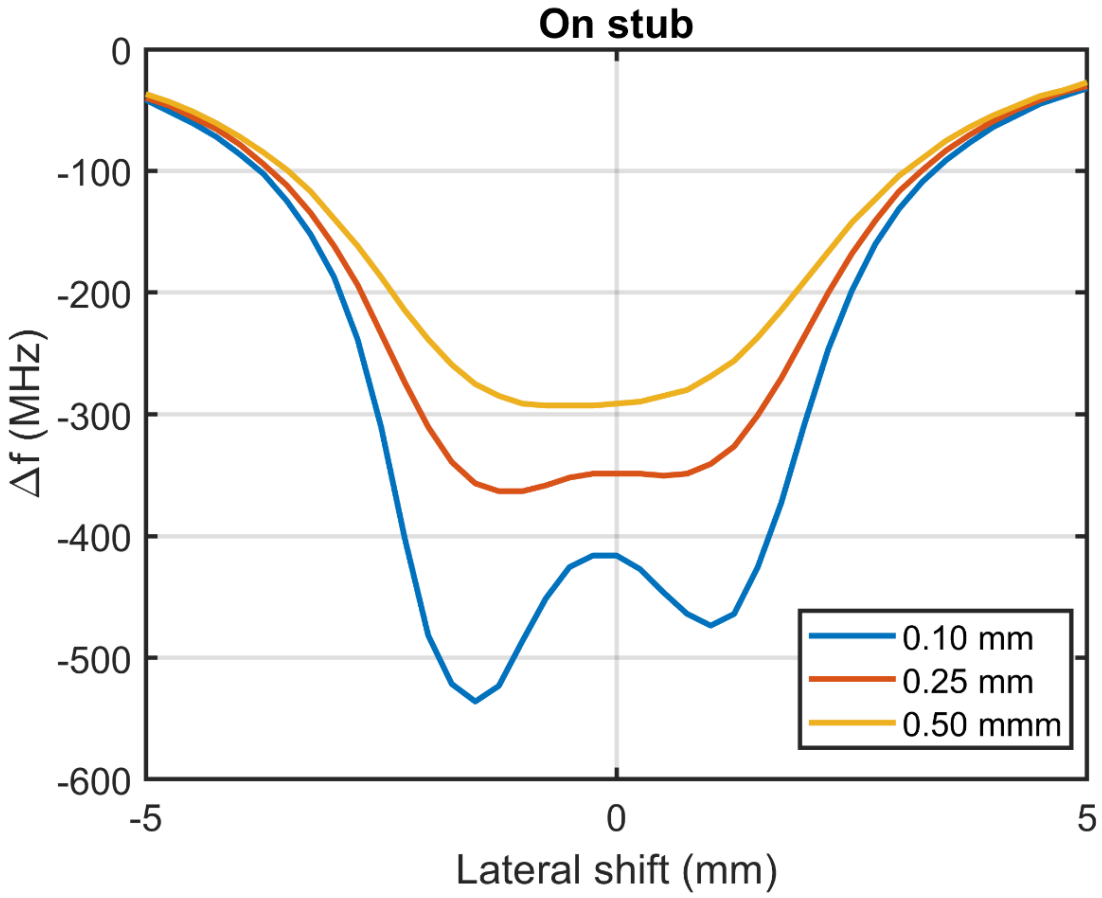


Figure 5.2: A cylindrical magnet with a height of 1 mm and a radius of 0.375 mm is placed at different positions above the stub to measure sensitivity of the cavity. The magnet was held in a dielectric capillary, and its position was controlled using micrometer stages.

Figure 5.3 shows the resonance frequency shift as a function of the height of the magnet measured with the end of the stub being 0 mm. In particular, we expect the magnitude of

the frequency downshift to be between -100 MHz and -200 MHz when the magnet is in contact with the surface of the stub. The resonance frequency comes within 5 MHz of that of the bare cavity once the magnet height is greater than 3 mm. We observe stronger coupling when the magnet is located near the edge of the stub because the electric field is concentrated around the perimeter [57].

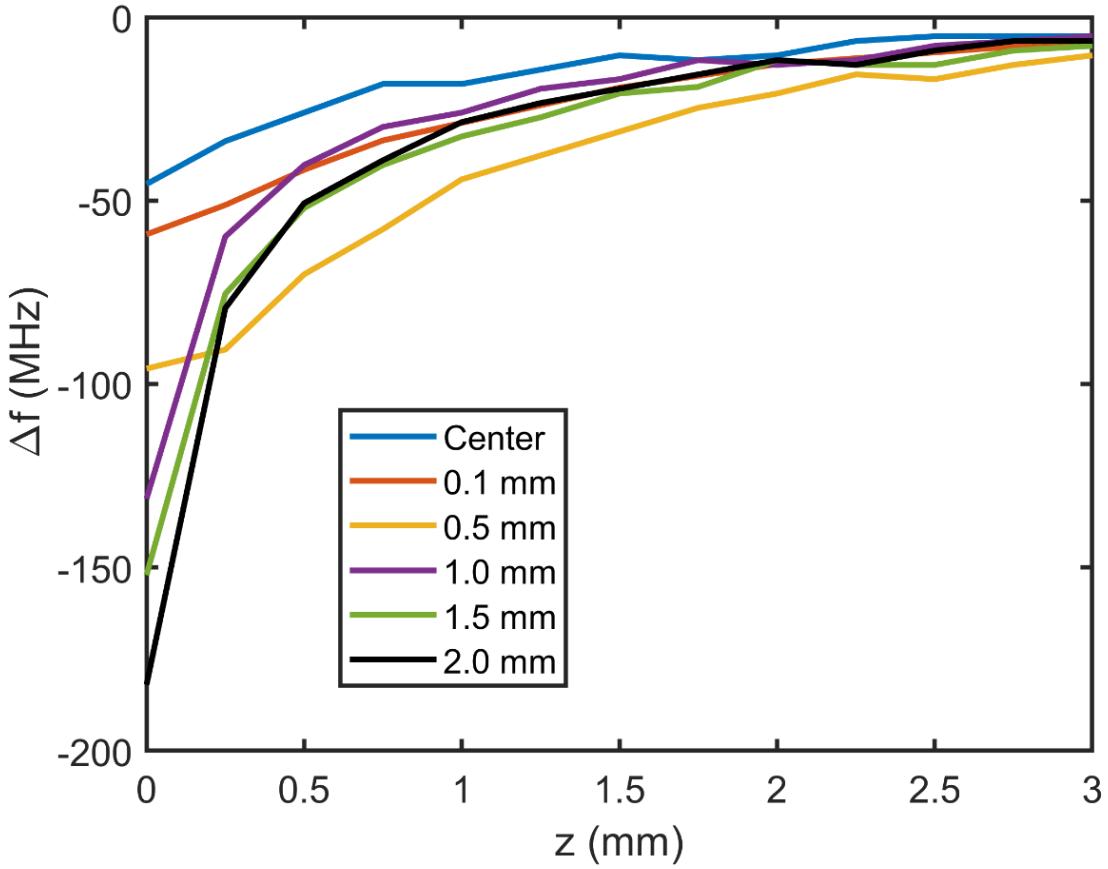


Figure 5.3: The magnet is positioned at different vertical coordinates on the cavity's stub by the translational stage of the micrometer.

Now, the vertical translation of the magnet is done outside of the stub in Figure 5.4. It is moved from 4 mm above the stub to the bottom of the cavity. The magnet on and above the stub has shown a similar frequency shift trend that is seen in the above figure. The trend of frequency shift reversed as the magnet got past the stub towards the bottom of the cavity. The magnet plays the opposite role sitting on the stub and bottom of the cavity. The magnet on the stub increases the effective height of the stub. The frequency of the cavity, hence, downshifts. However, on the bottom of the cavity it tends to raise the floor of the cavity. Thereby reducing effective height of the stub. This, in contrast, results in the upshift of the frequency.

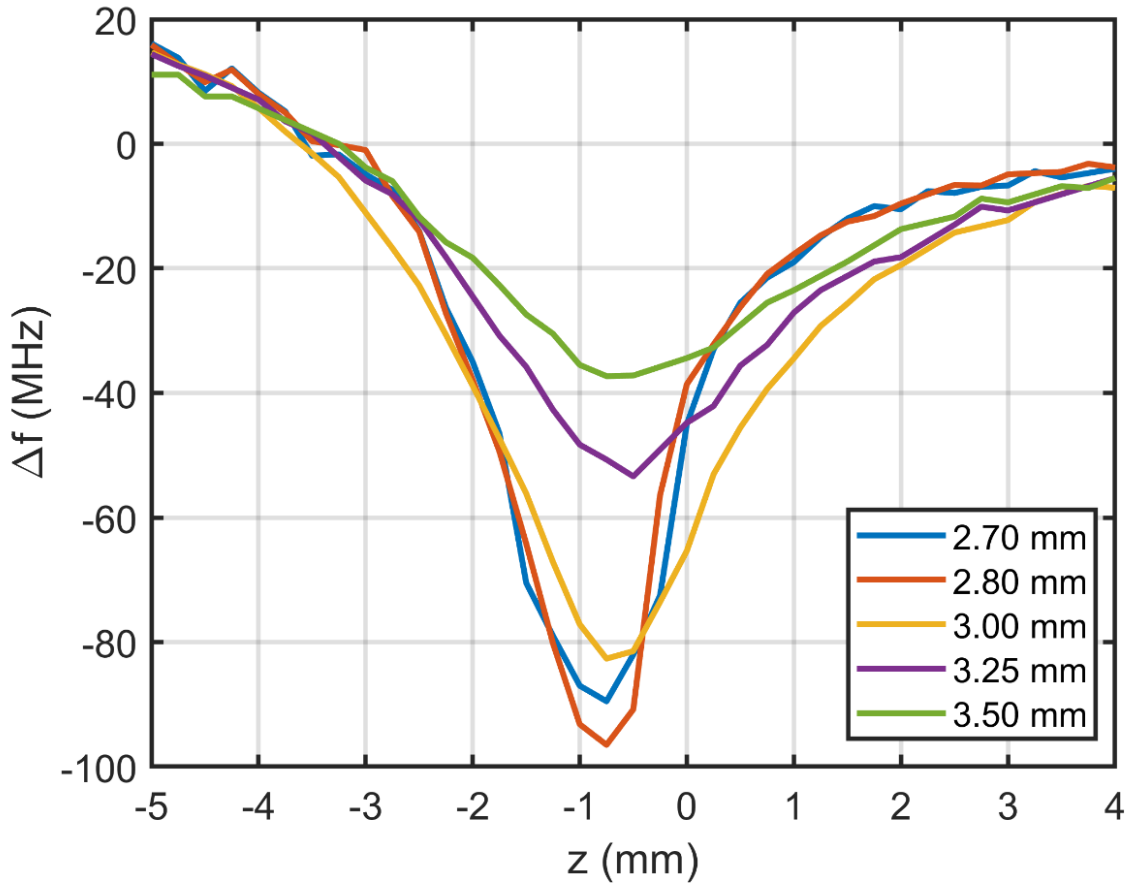


Figure 5.4: The magnet is vertically translated at different locations outside of the stub. The starting position of magnetic translation is 4 mm above the stub, and it ends up on the bottom of the cavity (-5 mm).

Figure 5.5 illustrates the change in the resonance frequency of the cavity in the region between the stub and wall of the cavity. The magnet is laterally moved from the wall towards the stub. According to the trend of the frequency shift, the region can be divided into three parts: (a) $0 \leq z < 2.5$ mm, (b) $z \cong 2.5$ mm, (c) $z > 2.5$ mm.
The first region (a) is the region that lies close to the bottom of the cavity. In this region, the magnet interacts mainly with the rf magnetic field of the cavity. Such interactions result in a frequency upshift from the empty cavity frequency ($\Delta f = 0$). A maximum of 25 MHz frequency upshift is observed when the magnet is on the bottom and close to the stub of the cavity. The region (b) is halfway between the stub and bottom of the cavity. The sensitivity is least in this region among all three regions. The availability of the rf fields is low. In this part of the cavity, one can even hide the magnet without seeing significant changes in the frequency of the cavity. The push of the magnet from the wall towards the stub, in the region (c), turns around the change frequency shift that is seen at the bottom of the cavity. The magnet in this region interacts with the cavity's electric field.

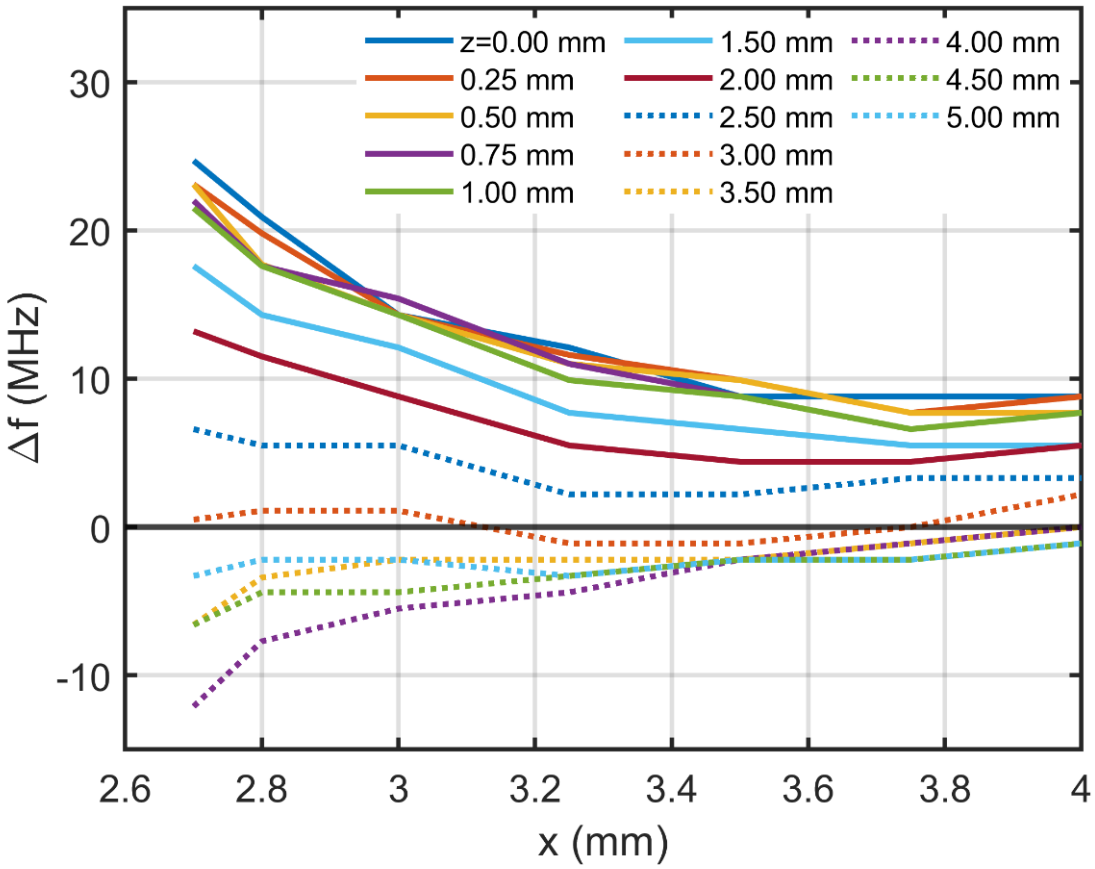


Figure 5.5: The region between the stub and wall of the cavity is probed by the magnet. Here, Δf=0 is the frequency of the bare cavity.

### 5.1.3 Disc Magnet

The frequency shift pattern seen in the above room temperature experiments is confirmed by replacing the cylindrical magnet with the disc magnet. A similar experimental procedure is followed in these measurements [67].

The experimental results as the magnet are radially and vertically translated on the stub is compared with the FEM simulations in Figure 5.6. When the magnet is still in contact with the stub ($z = 0$), lateral movement of the magnet towards the edge of the stub produces a frequency downshift of -50 MHz/mm. According to our calculations, the most prominent height sensitivity is expected for a magnet positioned at the edge of the stub (1.75 mm) where the sensitivity is -400 MHz/mm for levitation heights of 0-0.1 mm. Once the levitation height exceeds z=0.7 mm, the levitation sensitivity no longer depends strongly on the lateral position [5].

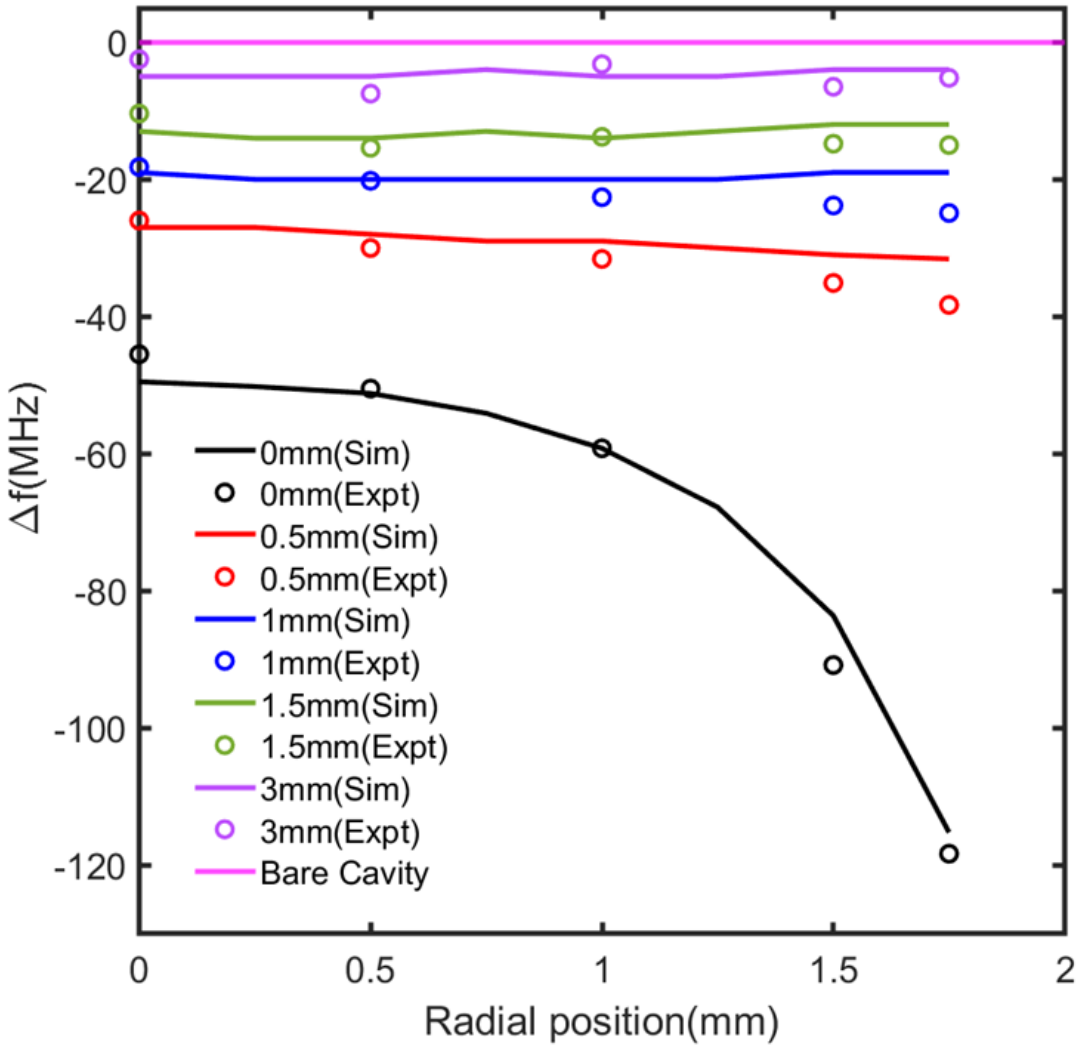


Figure 5.6: The room temperature measurements are done by placing the magnet at different positions on the surface of the stub. The experimental results are compared with the FEM simulations. The frequency change (Δf) is the difference in frequency between that of the bare cavity and the cavity with the magnet.

## 5.2 Low-Temperature Measurements

### 5.2.1. Cylindrical Magnet

Major part of the work presented in this section is published in IEEE Transactions on Applied Superconductivity [57].

We study field-cooled magnetic levitation of a millimeter-scale neodymium magnet within a cm-scale aluminum coaxial-stub SRF cavity. The SRF cavity has a resonance of 10.4 GHz and a loaded Q of 1400 and is fabricated from 6061 (97.9% pure) aluminum. The cylindrical (0.75-mm diameter by 1-mm high) neodymium magnet has a maximum magnetic field of 1.44 T (N50), which is ~140-times greater than the critical field of the

aluminum. Below the critical temperature for superconductivity, the magnet levitates 2.5 mm above the surface of the material and its behavior is monitored by measuring changes in the SRF resonant frequency. Room temperature measurements and simulations of magnet position's effect on the cavity mode support our conclusions. This novel magnet-cavity system provides a means to couple the low-frequency mechanical motion of the magnet with other objects whose quantum states can be probed and manipulated, such as magnons and transmons [68]. Consequently, the system is a promising candidate for studying the quantum mechanics of macroscopic oscillators [31].

The experimental schematic is shown in the Figure 5.7 (b). The cavity and magnet are placed on the base plate of the dilution refrigerator where the temperature can be reduced to ~50 mK, which is below the zero-field critical temperature of aluminum ($T_C$~1.2 K), while the vacuum pressure is held to ~$10^{-7}$ mbar. A pin antenna is coupled to the quarter-wave SRF mode at the stub height inside the cavity, where the electric field is strongly localized. Measurements are performed using a vector network analyzer whose probe signal passes through a circulator, is reflected by the cavity, and the reflection is separated by the circulator. For these measurements the cavity is over-coupled which reduces the loaded Q, but allows us to measure the resonance frequency from room temperature down to 50 mK. The cavity is held in place with N-type cryo grease to ensure thermal conductivity with the cryostat. We conducted a sequence of three experiments. First, the cavity (including a plastic sleeve around the stub whose purpose is to keep the magnet from falling off the top of the stub) is cooled without any magnet present. Here we see the dependence of the cavity resonance frequency as a function of temperature. Second, the magnet is placed within the cavity on the top of the stub where the plastic sleeve keeps the magnet from falling off of the top of the stub. Third, the same magnet is placed at the bottom of the same cavity. In all of these experiments all other experimental conditions remain the same.

The dimension and shape of the cavity are shown in the Figure 5.7 (a). This cavity is made up by 6061 aluminum. It is a coaxial cylindrical cavity with one end open. The outer cylinder has radius and height, respectively, 7 mm and 55 mm. The inner cylinder has radius of 2 mm and height of 5 mm giving a quarter-wave resonance of 10 GHz. In our design, the thickness of the metal on the bottom part of the cavity is 6.5 mm. The cylindrical neodymium magnet (shown in the Figure 5.7 (c)) is 1 mm high and has a radius of 0.375 mm. The N50 magnet has a remanence of 1.44 T (provided by manufacturer) and a mass of 4 mg. Assuming homogeneous magnetization, the magnetic dipole moment is $5\times10^{-4}$ $A.m^2$.

When the cavity is cooled to below its superconducting transition, we expect the magnet to levitate above the surface due to the Meissner effect in Type I superconductors. Figure 5.7 (d) illustrates the expected changes to the resonance frequency of the cavity during levitation experiments. The frequency, *f*, of a coaxial stub cavity is determined by the height of the stub, *l*, where $f \alpha \frac{1}{4l}$. Any perturbation within the coaxial region of the cavity changes the shape of the cavity mode and hence its frequency [35]. When a magnet is

placed on the surface of the stub, it increases the effective height of the stub and hence decreases frequency of the cavity. The amount of this downshift corresponds to the interaction of the magnet with the electric field of the cavity mode, which is concentrated toward the edges of the stub. Conversely, when the magnet is placed on the bottom of the cavity it raises the floor of the cavity. This reduces the effective length of the stub which causes the resonance frequency to increase. As the magnet levitates above either surface of the cavity, the frequency of the cavity shifts towards the frequency of the bare cavity (cavity without any magnet).

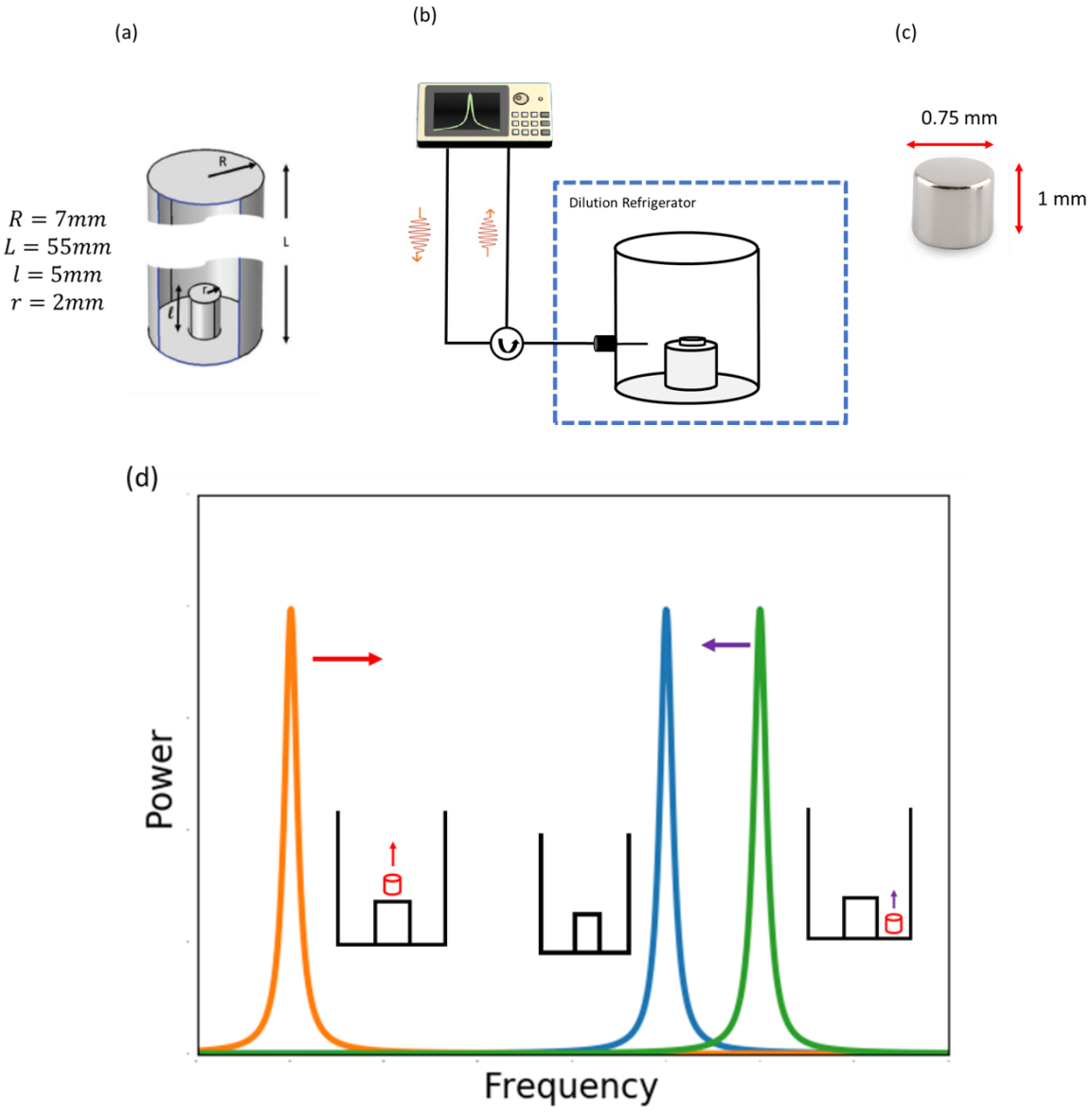


Figure 5.7: (a) This is a schematic of the cavity used in our work. It has a coaxial part, which contains a stub, and a cylindrical part has one open end and is closed at the other. (b) Schematic of the experimental set up. A magnet is placed on the top part of the stub of the coaxial microwave cavity. The cavity is probed by the signal sent from the network

analyzer. (c) The shape and size of the N50 magnet used in our work. It has a maximum field strength of 1. 44 T and surface field of 0.67 T. (d) Expected frequency shift with the position of the magnet. When there is no magnet in the cavity (a bare cavity), the resonance frequency is fixed and given by the blue curve. If the magnet rests on the bottom of the cavity, the cavity resonance frequency is higher than that of the bare cavity as shown by the green curve. As the magnet levitates above the bottom of the cavity, we expect the resonance frequency to shift lower as a function of levitation height (as indicated by the left-pointing purple arrow at the tip of the green curve). If the magnet rests on the top of the stub, its resonance frequency is significantly lower than that of the bare cavity as shown by the orange curve. As the magnet levitates above the stub, we expect the resonance frequency to shift higher as a function of levitation height (as indicated by the right-pointing red arrow at the tip of the orange curve). The sensitivity of the resonance frequency as a function of position depends on the radial position of the magnet. In both cases, as the magnet levitates the resonance frequency shifts towards that of the bare cavity.

Figure 5.8 shows the resonance frequency shift as a function of the gap between the magnet and the tip of the stub. The solid curves are simulations and the symbols are room temperature eexperimental data. In particular, we expect the magnitude of the frequency downshift to be between -100 MHz and -200 MHz when the magnet is in contact with the surface of the stub. The resonance frequency comes within 5 MHz of that of the bare cavity once the magnet height is greater than 3 mm. We observe stronger coupling when the magnet is located near the edge of the stub because the electric field is concentrated around the edge. Finite element calculations (COMSOL Multiphysics) reveal the same trends. In these calculations, the size of the magnet and the cavity are the same as the experimental work. These room temperature measurements and simulations allow us to predict the behavior of the system during levitation experiments.

The frequency of the bare cavity without the magnet is 10.041 GHz at 5K, shifting upward by 5 kHz as the temperature decreases from 5 K to 55 mK (See Figure 5.9)). With the bare cavity frequency as a reference, when the magnet is placed on the stub, the frequency shifts down by 130 MHz to 9.910 GHz. The amount of frequency shift varies with the exact position of the magnet on the tip of the stub with the maximum shift occurring when the magnet is placed near the edge of the stub. For the case of a magnet on the stub, we observed 120 MHz of frequency change as the temperature drops from 5 K to 65 mK, as shown by the solid lines in Figure 5.9 (b). The sudden frequency shift at 650 mK is consistent with levitation due to expulsion of the magnetic field from the material below the magnet. As the temperature drops below 100 mK the frequency shift approaches -12 MHz. Our measurements are consistent over several heating and cooling cycles. We also report measurements for the case where the magnet is placed in the bottom of the cavity. The variations in the cavity resonance frequency are smaller, but still measurable. At 5 K the difference between frequency of bare cavity and cavity with magnet on the bottom is +11 MHz. As temperature is reduced to 57 mK the frequency difference drops to +5 MHz.

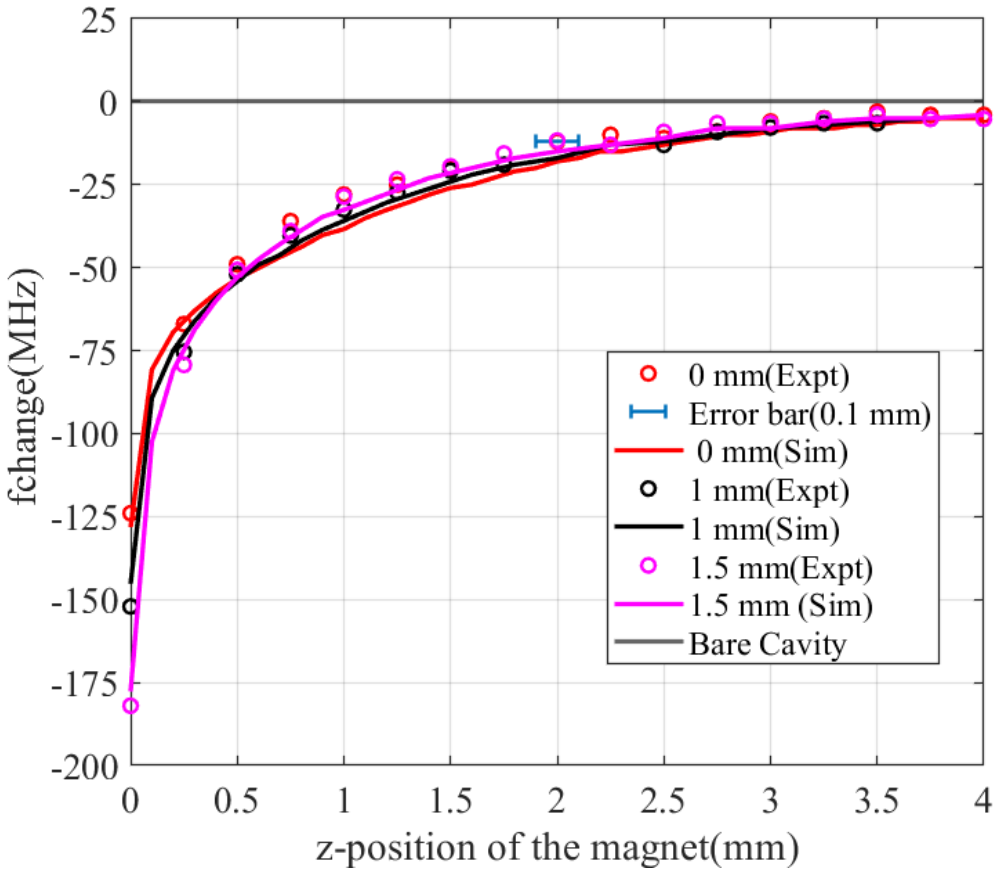


Figure 5.8: The room temperature data obtained from procedure describe in above section 5.1.1. is compared with the FEM simulations. The error bar is same for all experimental data.

The neodymium permanent magnet has a maximum magnetic field (remanence) of 1.44 T and a surface field of 0.67 T. When the magnet rests directly on the surface of the aluminum, the magnetic field strength at the interface is larger than the critical field of the aluminum 100 gauss at 1.2 K. This creates a normal conducting region having a depth of 1-2 mm directly below the magnet. As the temperature drops, the critical field increases and the normal region becomes thinner. Below 650 mK there is sufficient lift due to the Meissner effect to offset the gravitational force and levitate the magnet. Once the magnet begins to lift at 650 mK, the normal region shrinks which increases the Meissner force, making magnet jump up to its equilibrium position of 2.5 mm. At this point the magnetic flux is completely expelled from the volume of the superconductor. For the case of the magnet levitated 2.5 mm above the stub, the sensitivity of the resonance frequency to height fluctuations is 10 MHz/mm. For levitation above the bottom of the cavity we expect the sensitivity to be less than above the stub by a factor of 50.

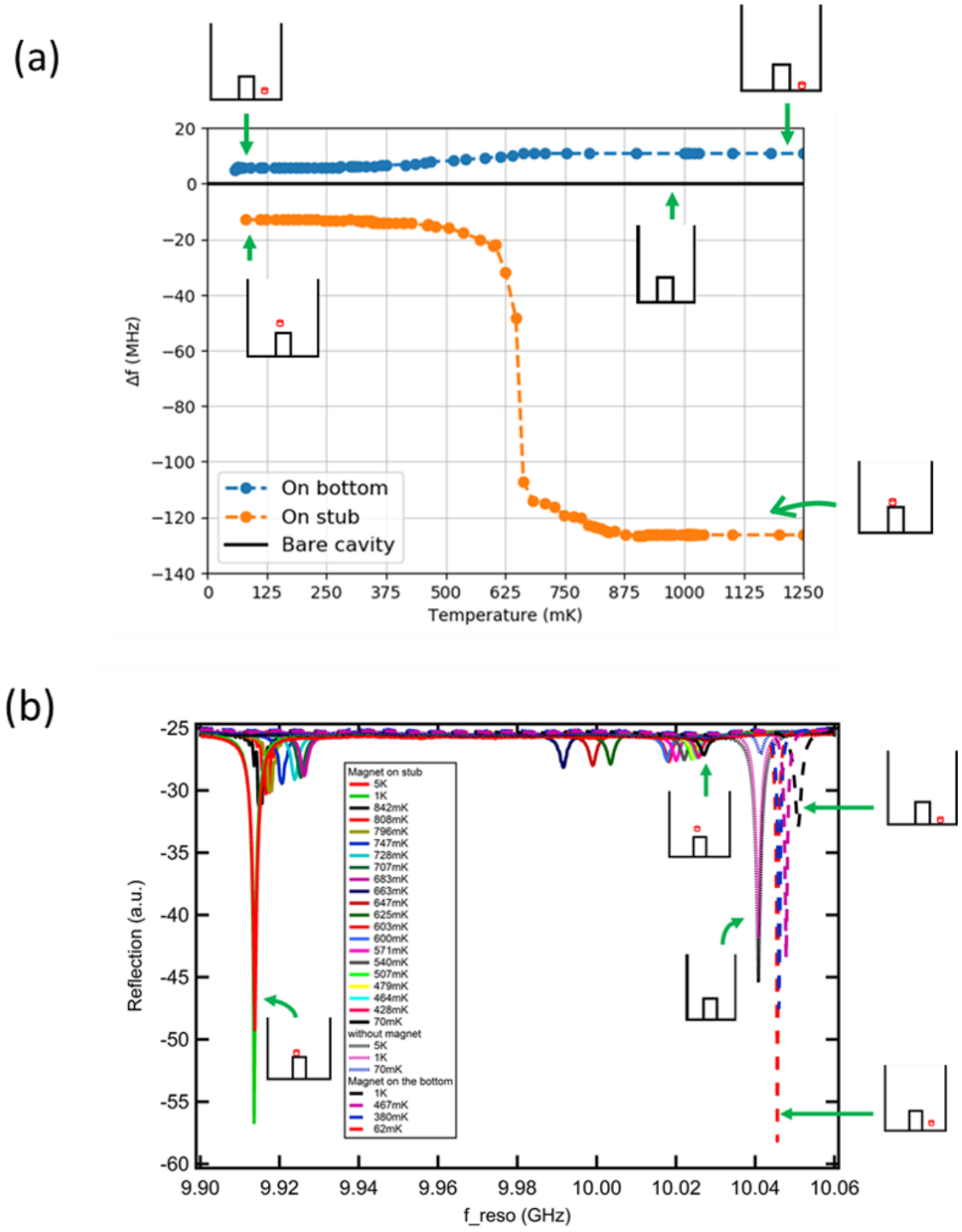


Figure 5.9: (a): Cavity resonance frequency shift as a function of temperature. $\Delta f = 0$, represents frequency of the bare cavity. (b): A composite of reflection spectrum measurements for the three cavity configurations and for a range of temperatures. When a magnet is located on the top of the stub and cooled to 70mK, we observe a downward shift in frequency (solid lines) which is reduced from -130 MHz at 1 K down to -12 MHz at 70

mK. When the magnet is located on the bottom of the cavity, the frequency is up shifted and drops from 11 MHz at 1 K to 5 MHz at 50 mK (dashed lines).

### 5.2.2 Disc magnet

Most of this work is submitted for publication [5].

Figure 5.10 illustrates measurements scheme of our cavity-magnet system, which sits in the mixing chamber of a dilution refrigerator at T=30 mK. The refrigerator is pre-cool from room temperature to 5 K and then further cool down from 5 K to 50 mK by using the pulse tube refrigeration technique. In the latter stage of the cooling, the vacuum pressure of the fridge is $10^{-7}$ mbar maintained by the turbo molecular cryo pumping. The spectroscopic measurements are taken by sending a signal from a vector network analyzer HP8720 through SMA cables inside the fridge and into the cavity via an over coupled straight pin couplers. The transmitted signal ($S_{21}$ ($\omega$)) is amplified by a HEMT amplifier (at 4 K) and post amplifiers (at room temperature). Temperature of the system is monitored with the thermometer placed in the mixing chamber of the fridge. N-type cryogenic grease is used to maintain thermal contact between the cavity and the base plate of the dilution refrigerator.

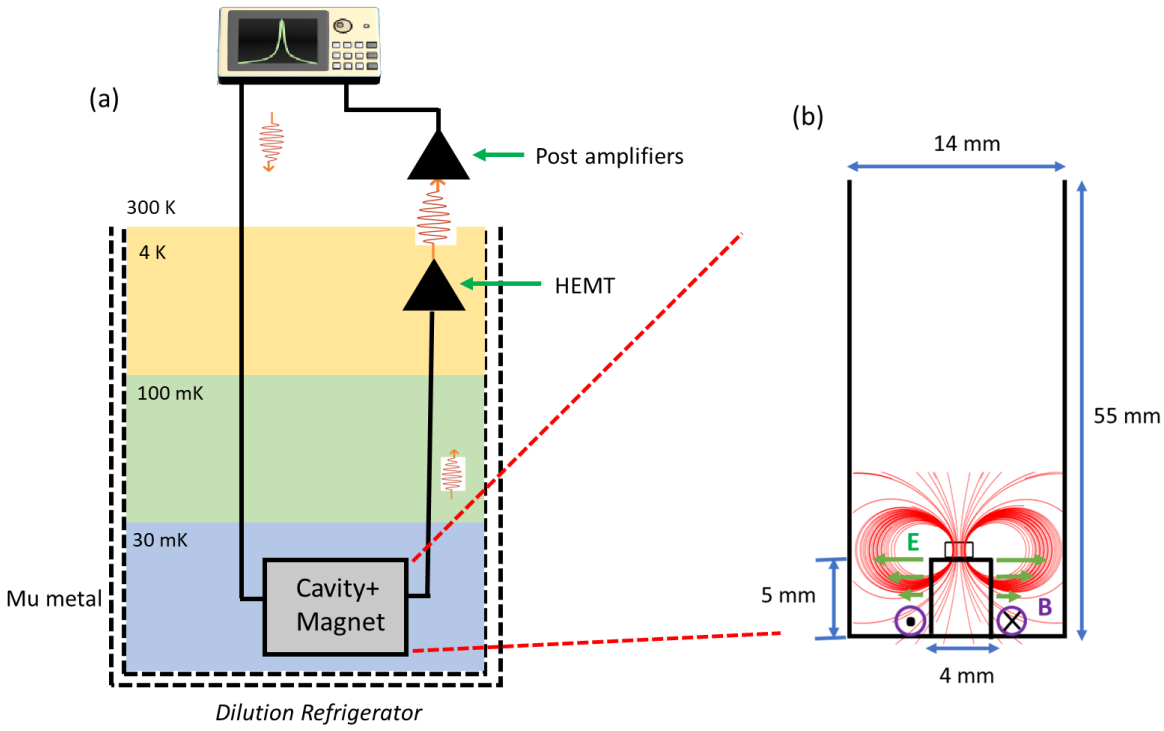


Figure 5.10: (a) Schematic of experimental set up (not in scale). The cavity-magnet configuration is attached to the base plate of a dilution refrigerator. (b) Front view of the coaxial cavity with a magnet on the top part of the stub. The electric field is highly concentrated at the rim of the stub (green arrow) and decays towards the conducting wall of the cavity. $F_Z$: Meissner force, $F_G$: gravitational force.

In the present work we report on new experiments where we varied the magnetic field strength of the levitated magnet. We find that analyzing the cavity's loaded quality factor, Q, along with the resonance frequency provides insight into the movement of the magnet prior to its lifting. When the magnet rests in the most sensitive region of the cavity, near the edge of the stub where the RF electric field is highly concentrated, small fluctuations in the magnet's position are evident in the RF spectrum. As expected, we observed abrupt shifts in the peak position of the RF spectra during the transition to levitation, and the magnet's steady state levitation height is proportional to the square root of the field strength. During the transition a sharp rise in the quality factor as high as 17 % is observed [69]. We compare our measured frequency shifts with finite element simulations, room temperature measurements and a lumped element model. By doing so we confirm that variations in the resonance frequency prior to levitation can be explained by movement of the magnet along the surface of the stub. The increase in Q with falling temperature agrees with theory and with experimental results reported by other group [69,70]. The analysis approach described here enables characterization of magnetic levitation within a microwave cavity when there is no visual access within the sample chamber. It provides an alternative to camera tracing systems, coils or SQUIDs for the observation of levitation, opening up the system's application to precision measurements.

We use identically-shaped neodymium disc magnets with a diameter of 1 mm, a height of 0.5 mm, and with a mass of 2.75 mg. The magnets are classified as N35, N42, N50, and N52 with remanences of 1.22 T, 1.32 T, 1.44 T, and 1.47 T respectively (remanence, provided by the manufacturer). We assume the remanence of the magnets remains constant at low temperature [38]. The corresponding magnetic moments are 0.38-0.46 $(\mathrm{mA})\mathrm{m}^2$, respectively. The magnetic field on the surface of the N35, N42, N50, and N52 magnets are, respectively, 0.43 T, 0.47 T, 0.51 T, and 0.52 T. No external magnetic field is applied inside the cavity other than the field from the magnet.

A transmission $|S21|$ recorded during a typical experiment using the N52 magnet is shown in Figure 5.11 where the temperature drops from 1.25 K down to 50 mK. Three key phenomena are highlighted by shaded regions in Figure 5.11. First, the transmission $|S21|$ gets narrower and the peak power increases. In this region, most of the cavity, except for that region right below the magnet, undergoes the superconducting transition as the temperature of the cavity is below the zero-magnetic-field critical transition temperature. The top of the stub is still normal due to the magnet's strong magnetic field. As the temperature of the cavity drops further, the normal region under the magnet shrinks and becomes a superconductor. During this stage, the magnet is not yet levitated, but likely moving, wobbling or making a small angle with respect to the superconductor. When the magnet moves but is not levitated, ~20 MHz frequency upshifts are typically observed. Finally, when the entire stub is in the Meissner state the magnet lifts from the surface of the superconductor resulting in a large frequency upshift of ~60 MHz.

When the bare cavity (with the plastic sleeve surrounding the stub) is cooled through the superconducting transition of aluminum at 1.2 K we observe a negligible frequency shift

of a few kHz due to a change in the penetration depth. Larger shifts (~20 MHz) due to thermal contraction as the system cools from room temperature are reproducible across all measurements. The bare cavity's resonance at ~5 K is used as the reference frequency for levitation experiments (Δf=0). The absolute resonance frequency of the bare cavity at 50 mK is 10.04 GHz.

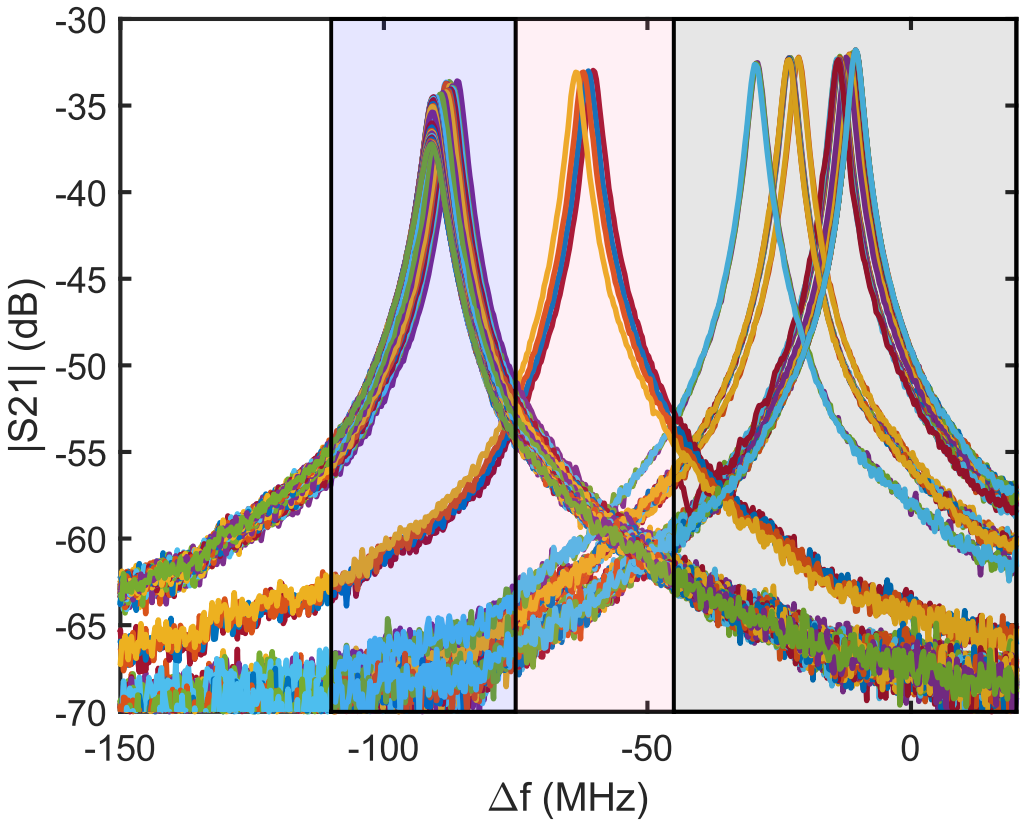


Figure 5.11: An example of how transmission |S21| change as the temperature of the cavity with the magnet goes from 1.25 k- 50 mK. The transmission |S21| presented here are for the N52 magnet.

Figure 5.12 shows the change in resonance frequency (Δf) and Q as a function of temperature between 1.25 K and 50 mK for the four magnets. The magnets are placed on top of the stub but the exact position on the stub is undetermined. Since the stub has minor imperfections, it is not perfectly symmetric and the frequency downshift due to the presence of the magnet varies depending upon the exact position of the magnet. For example, at 1.25 K, the frequency shift due to the N35 (1.22 T) and N42 (1.32 T) magnets is ~120 MHz, but the frequency shift for the N50 (1.44 T) and N52 (1.47 T) magnets is just ~90 MHz.

The changes in the loaded Q of the cavity as a function of temperature provide additional insight into the key phenomena occurring during the experiments. Figure 5.12 (lower panel) shows Q versus temperature for the corresponding measurements shown in the top panel. To obtain Q, the spectra are smoothed, the resonance frequency is located and the

full-width at half-maximum (FWHM) is measured at -3 *dB* from the peak. The quality factor is given by $Q = \frac{Resonant\ frequency}{FWHM}$ [71].

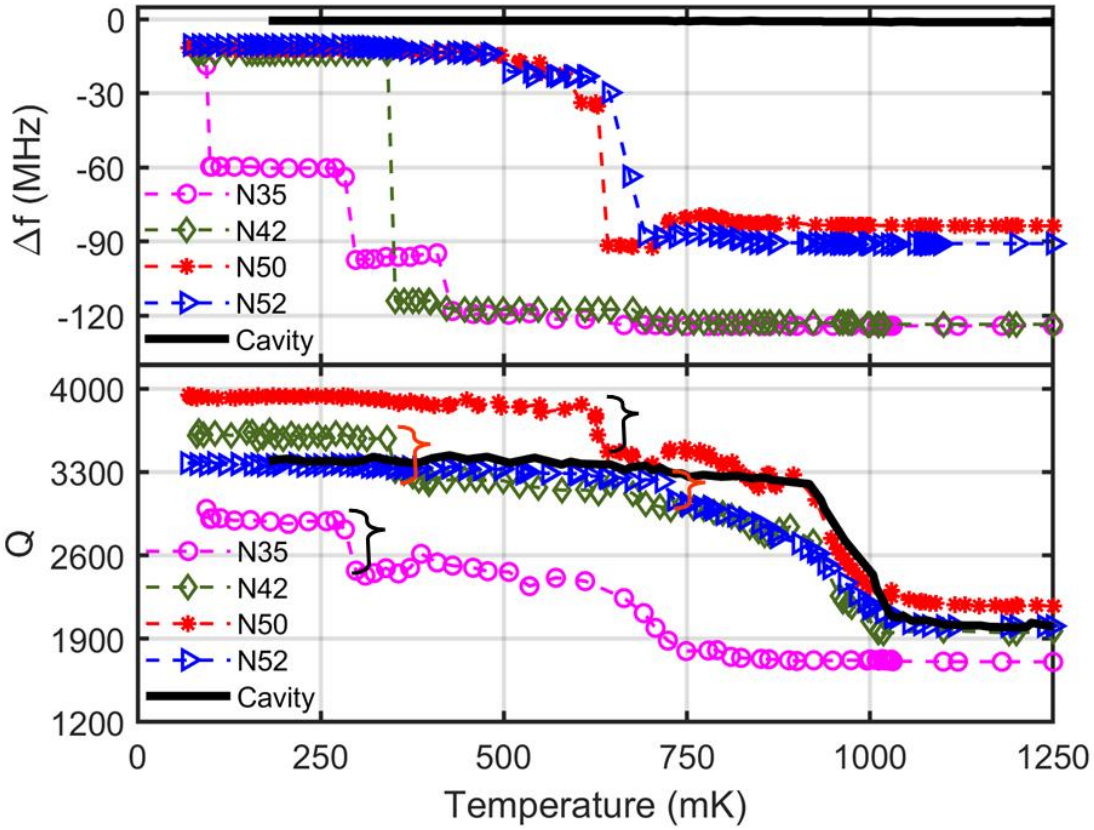


Figure 5.12: (upper panel) change in frequency as a function of temperature for N35, N42, N50, and N52 magnets. Note that stronger magnets exhibit a higher levitation temperature. The lower panel is the total quality factor of the four magnets. A sharp rise in the quality factor due to the Meissner effect is represented by the curly bracket.

In Figure 5.12 (lower panel), we observe that Q starts to increase when the temperature falls below 1.1 K. The zero-magnetic-field transition temperature for pure aluminum is 1.2 K. The transition temperature is lightly less than 1.2 K because of the magnet's presence in the cavity and use of the 6061 (97.9% pure) aluminum. The critical field of the superconducting aluminum increases as the temperature, $T$, falls according to $B_c(T) = B_0(1 - \frac{T^2}{T_c{}^2})$, here $B_0 = 0.01\,\mathrm{T}$ is the critical field maximum of aluminum at zero temperature and $T_c$ is the zero-field transition temperature. As the temperature of the cavity falls below 1 K most of the cavity goes superconducting and the Q of the cavity rises quadratically. For the cavity-magnet system, thereafter the Q deviates from the quadratic dependency when the magnet's position shifts or when the magnet tilts at some an angle with respect to the stub. Sharp increases in the quality factor are seen when the region of

the cavity nearest to the magnet goes into the Meissner state and the magnet levitates. The change in Q factor during Meissner transition is approximately 8 % for the N52 and N42 magnets and 12 % and 17 %, respectively, for the N50 and N35 magnets. No such changes are seen in the case of the empty cavity cooling.

Our observations are consistent with other reported Q vs. temperature studies of SRF cavities. An analysis of the change in Q as a function of temperature for a 3D-printed reentrant cavity is given in [69]. Like our measurements, the quadratic change in Q was observed during the superconducting transition. Similar behavior was observed in the cooling of a 3D superconducting aluminum microwave cavity [72]. The type II superconductor behaves as a type I below their first critical field ($HC_1$). In [70] a ferrimagnetic probe was used to experimentally evaluate the screening of magnetic fields from the walls of a superconducting Nb cavity as it changed to perfect diamagnetism. A sharp rise of approximately 20% is observed during the Meissner transition as the magnetic field decreases.

A summary of the change in the frequency and Q of the cavity due to all possible phenomenon during the magnetic levitation is given in table 5.1. When most of the cavity goes superconducting, there is negligible change in the frequency of the cavity. However, there is a quadratic rise in Q with decreasing temperature. The frequency and Q both increase when the magnet makes an angle with the stub. When the magnet moves towards the edge of the stub, on the other hand, the frequency and Q both decreases. Finally, during the magnetic levitation, the frequency and Q rise abruptly.

Table 5.1: Summary of changes in the resonance frequency and Q during levitation.

| Phenomena | Frequency | Quality factor |
|---|---|---|
| Most of the cavity superconducting | Negligible change ($\approx KHz$) | Quadratic rise (≈ 33%-46%) |
| Magnet makes an angle with the stub | Increases ($\approx 20$ MHz) | Increases (≈ 10%) |
| Magnet pushed towards the edge of the stub | Decreases ($\approx 10$ MHz) | Decreases (≈ 4%-6%) |
| Magnet levitates | Large upshift ($\approx 50 - 100$ MHz) | Sharp rise (≈ 8%-17%) |

The above observations are confirmed in Figure 5.13 by the multiple coolings of each cavity-magnet system. They were performed by warming the dilution refrigerator from base temperature (around 50 mK) to about 10 K (significantly higher than $T_c$ for aluminum), then back down to base temperature to allow us to view the frequency shift that occurs when levitation begins multiple times per experiment. In each cooling cycle, data is recorded as the temperature falls.

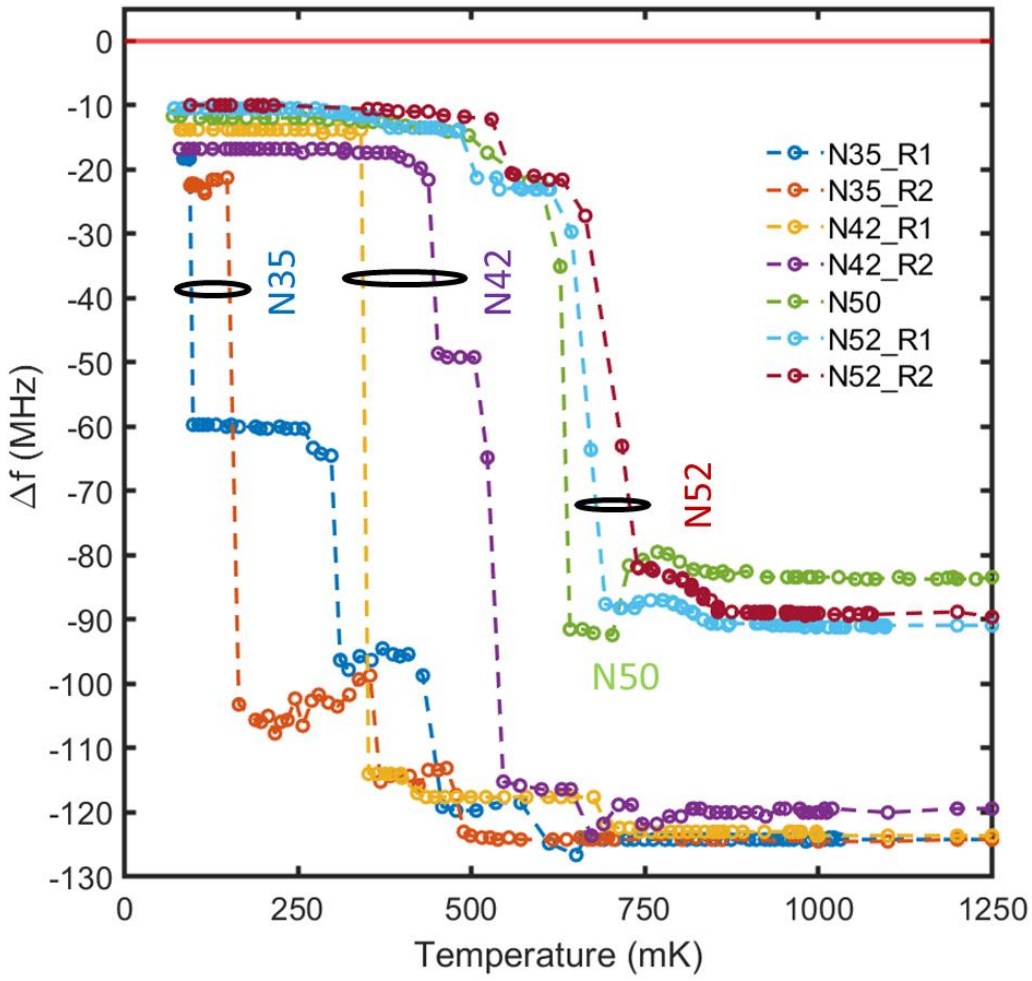


Figure 5.13: Change in frequency as a function of temperature for N35, N42, N50, and N52 magnets. The black ovals group together traces from the same magnet throughout multiple heating and cooling cycles.

In addition, one set of multiple heating and cooling cycles of data for the N42 (1.32 T remanence) magnet is plotted in Figure 5.14. This data is taken during the rapid heating of the system. There is a sharp rise in the fridge's temperature from 50 mK to 500 mK. After that temperature of the fridge stays at 720 mK before bouncing off to 2 K. The fridge warmed up slowly after 2 K.

The frequency shift pattern was consistent for four cooldowns and warm-up of the fridge. The observed phenomenon during the cooldowns can also be verified during the warm-ups. For example, the magnet making an angle with the stub during the cooldowns can be seen during the warm-ups in form of a large dip in the frequency. We also monitor the frequency of the cavity for several days at base temperature and observe that the levitation was stable over this period.

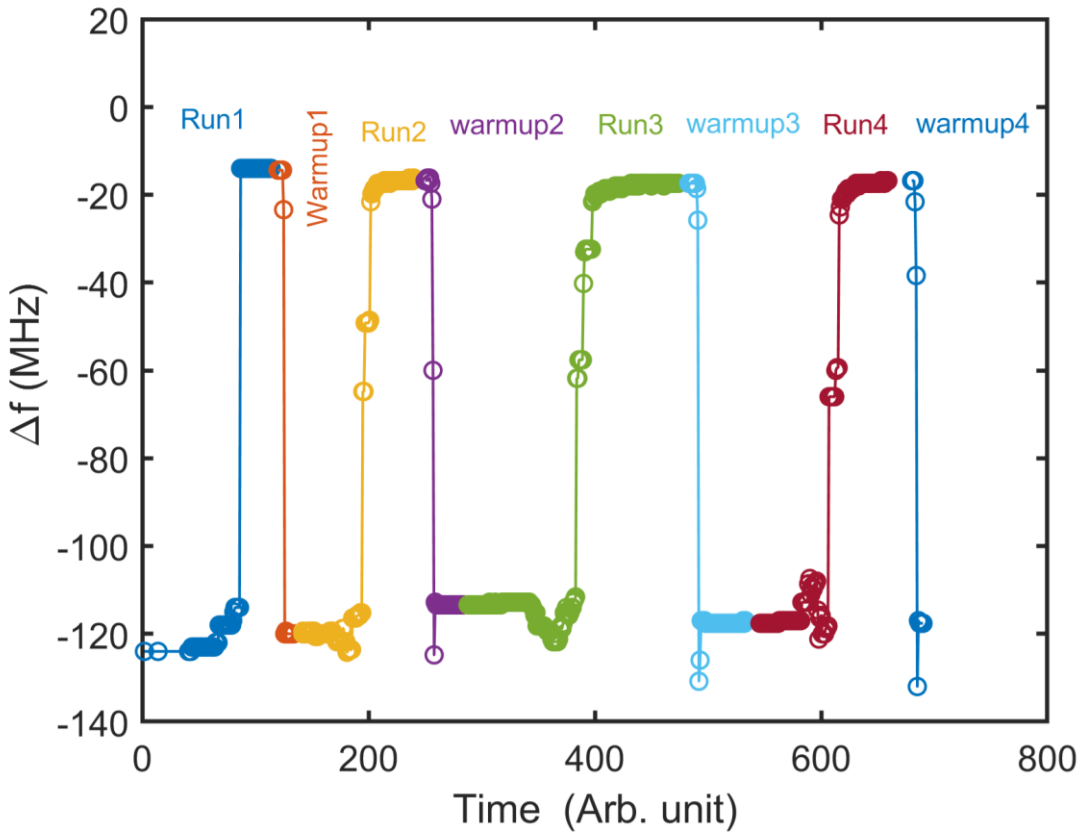


Figure 5.14: Multiple cooling and heating cycles of the fridge for the N42 magnet.

In one of our experiments, we have done control heating and cooling of the fridge. Instead of letting the fridge control the temperature, we have manually set the temperature of the fridge. The first step of the procedure is to the temperature is set in the loops chamber set point on the dilution refrigerator. This, in turn on the chamber heater of the fridge. The fridge adjusted the power of the chamber heater to maintain the set temperature.

The results of the controlled heating and cooling of the N35 magnet are shown in Figure 5.15. The black trace shows automated cooling of the cavity. When the fridge cooled down the base temperature, it was heated up in a controlled manner up to 900 mK (red trace) and cooled down again to 400 mK (blue trace). We have chosen these upper and lower limits of temperature because interesting physics happens in this temperature region.

Hysteresis is observed during the manual heating and cooling of the fridge. The main contributor to such observation is the use of the strong magnet. As discussed in chapter 4.6 Superconducting-Normal Region, a strong magnet on the superconductor creates two regions: a normal and superconducting region. The effect of the normal region is dominant during cool down when the magnet sits on the stub. The superconductor needs to go colder than usual to get rid of this area. However, the heating up breaks the cooper pairs.

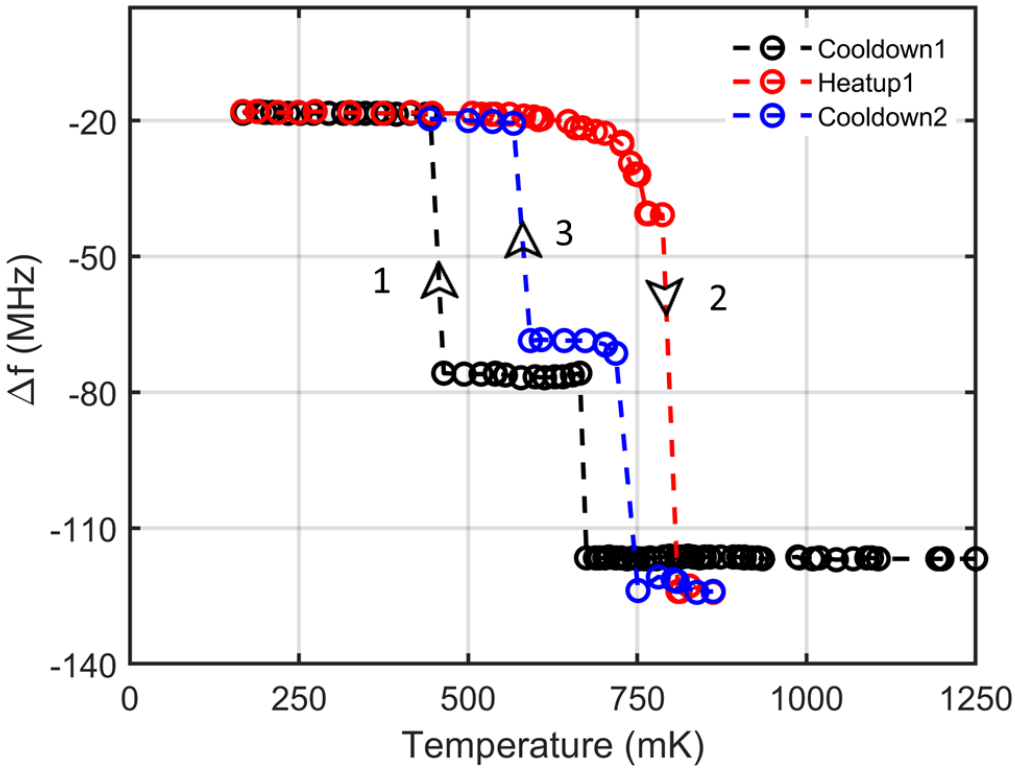


Figure 5.15: Observation of hysteresis in control cooling and heating of the fridge.

To calculate levitation height from experimental results, the frequency shift that is observed in the experimental results (Figure 5.12) is compared with the FEM calculations. One such calculation is shown in Figure 5.16 for the N52 magnet. The minimum frequency shift of 10 MHz is observed in the experiment. The frequency is compared with the simulation result (the solid red line). When compared with the simulation, this value corresponds to a levitation height of 1.8 mm (red dotted line). The same procedure is followed for all four magnets that were used in the experiment.

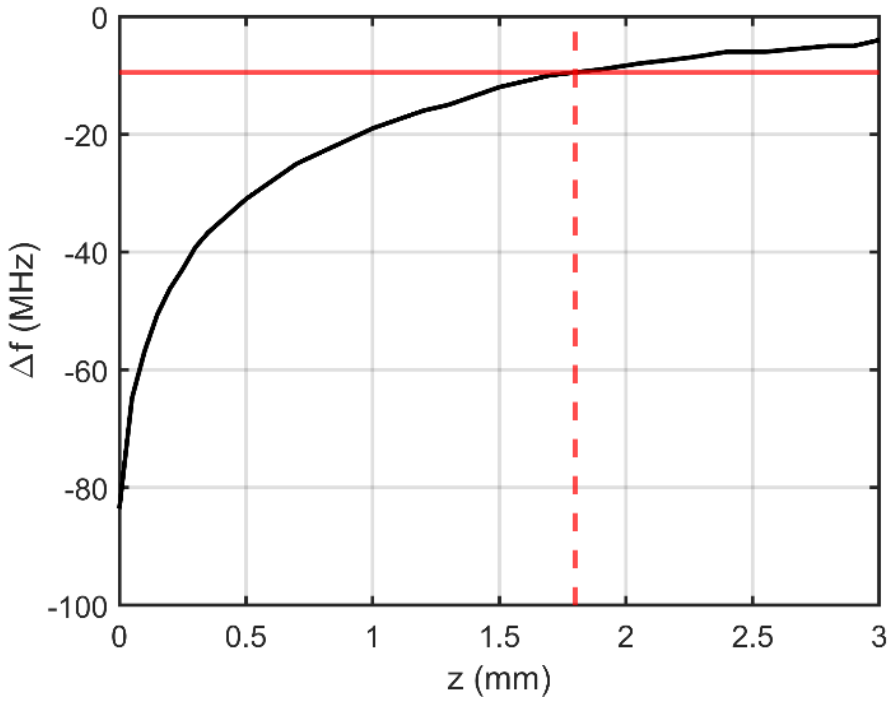


Figure 5.16: The frequency shift observed in the steady state magnetic levitation is compared with the simulation result to calculate the levitation height.

Table 5.2: List of levitation height for the four magnets used in the experiment obtained using above method.

| Magnet Type | Levitation height (mm) |
|---|---|
| N35 | 1.30 |
| N42 | 1.46 |
| N50 | 1.65 |
| N52 | 1.70 |

Figure 5.17 compares levitation height derived from the experimental result and FEM simulations, with the models we have developed by extending the two-loop model [73], and the image method. We also plot a fit of the data to a square-root dependence, which was predicted in equation (4.8). The fit and data support our models used to describe the levitation of the magnet within the cavity and give us confidence in our estimation of the levitation height.

We see that magnets producing a larger magnetic field attains a larger levitation height compared with magnets producing a smaller magnetic field. Our model predicts the levitation height more accurately than the widely used image method. For the N52 magnet multi-loop model overestimates levitation height only by 49%, in contrast to 140% overestimation by the image method. The uncertainty in our measurement of levitation height also decreases as the levitation force increases [74].

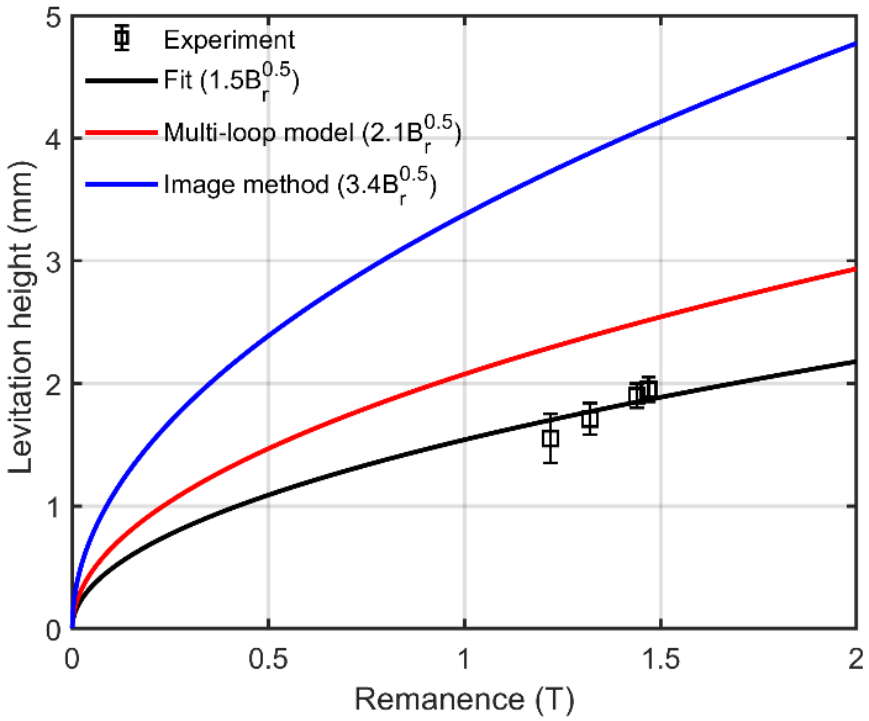


Figure 5.17: Change in the levitation height as a function of remanent field strength of the permanent magnet. The levitation height between the image method, our model, circuit model, and experimental result as a function of remanence.

Figure 5.18 compares the quality factor of an over-coupled cavity with a plastic sleeve around the stub (red dots), the same cavity with an N50 magnet (black dots) on the stub with the under-coupled ideal bare cavity (black line) as a function of temperature. The quality factor of the under-coupled ideal bare cavity is given by M-B theory as $\propto e^{(\frac{\Delta}{K_B T_C}\frac{T}{T_C})}$ ($Q \propto \frac{1}{R_s}$). The energy gap ($\frac{2\Delta}{K_B T_C}$) of the superconducting aluminum is 4.4 [44].

In Figure 5.18, we observe a significant deviation of the quality factor in the experimental measurements from that predicted by M-B theory. One of the main reasons for such an extensive degradation in the quality factor is the extension of pin couplers into the cavity. Consequently, for the cavity with the magnet, the motion and levitation of the magnet are modulated in the total quality. The study of the total quality factor is, hence, strengthening the characterization of magnetic levitation, which is one of the primary purposes of this thesis.

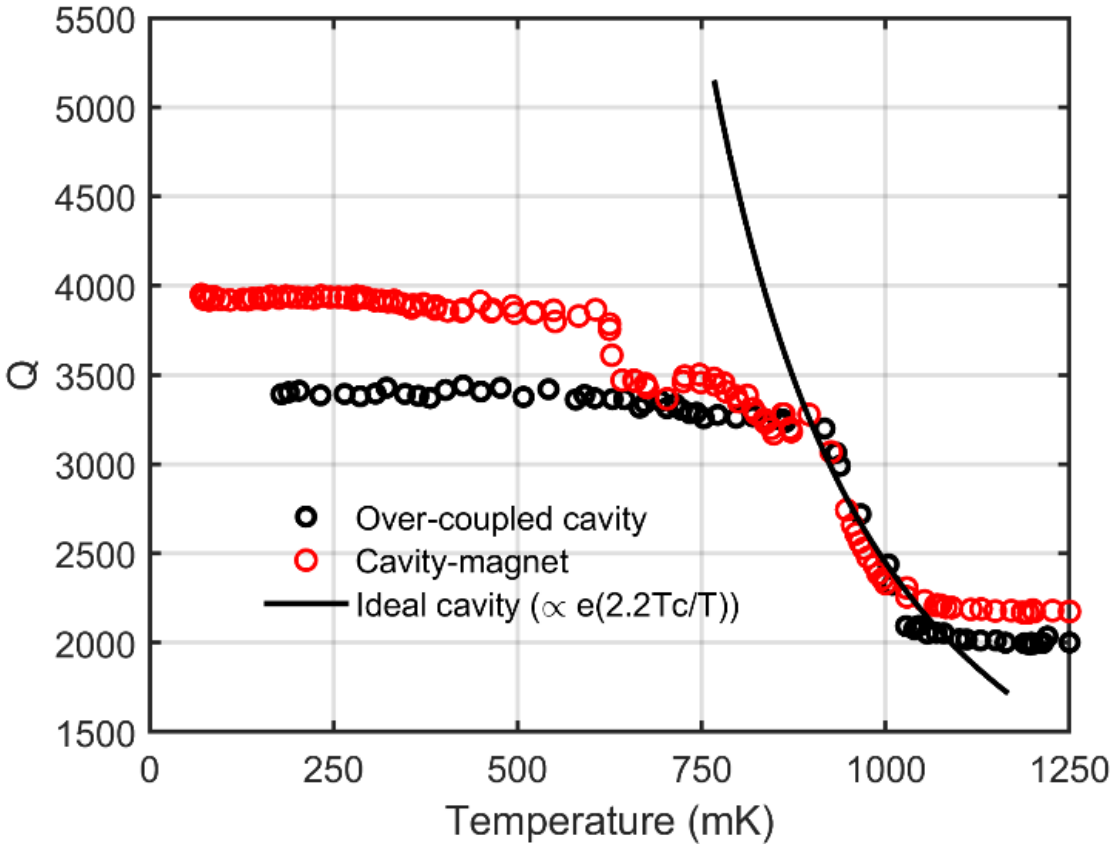


Figure 5.18: Comparison plot of Q between an ideal bare cavity, over-coupled cavity, and cavity with a N50 magnet.

As a final observation, by tuning a signal generator slightly off of the peak of the resonance, to the rising edge, we observe fluctuations in the transmitted signal power. These arise from the motion of the levitated magnet and are in the frequency range of 10-100 Hz, but the ringdown of this signal indicates that the magnet's steady-state motion while levitated is dominated by the presence of friction between the magnet and the sleeve. Modifications to the cavity are needed for stable levitation with high sensitivity to magnet motion without the sleeve in place.

In conclusion, we have characterized the levitation of a magnet within a superconducting microwave cavity for a range of magnet strengths. By analyzing the cavity's loaded quality factor along with the resonance frequency we gain a better understanding of the likely movement of the magnet throughout the experiment. As expected, we observed abrupt shifts in both the position and width of the resonance peak during the transition to levitation, and the magnet's steady state levitation height is proportional to the square root of the field strength. These results provide a baseline of understanding the levitation of magnets within SRF cavities and are instrumental for understanding ongoing experiments where quantum states are probed and manipulated within such cavities.

## 5.2.3 Spherical Magnet

The experiment with a symmetric shape magnet helps us to understand some phenomena seen in experiments with the disc shape magnets (see Figure 5.12). For example, there will be no angle for such a symmetric shape magnet during the levitation. One observation then there will be to watch is whether or not 10-20MHz frequency upshift is seen as seen in Figure 5.12). Curiosity will also be what happens to the intermediate state of the frequency shift. Are they related to the magnetic phenomenon or the property of the superconductor that has been used in the experiment?

We have done an experiment with a spherical magnet in the same experimental setup described in Figure 5.10. The magnet of radius 0.5 mm instead of the disc magnet is placed on the stub (see Figure 5.19 (a)). It has a remanence and mass of 1.47 T (N52) and 3.87 milligram. The mass of the spherical magnet we are using in this experiment is 1.4 times greater than the mass of the disc magnet that is used in the experiment discussed above. Figure 5.19 (b) shows the response of the cavity with the spherical magnet at 50 K. The resonance frequency of the cavity is 9.902 GHz. It has a quality factor of 1612.

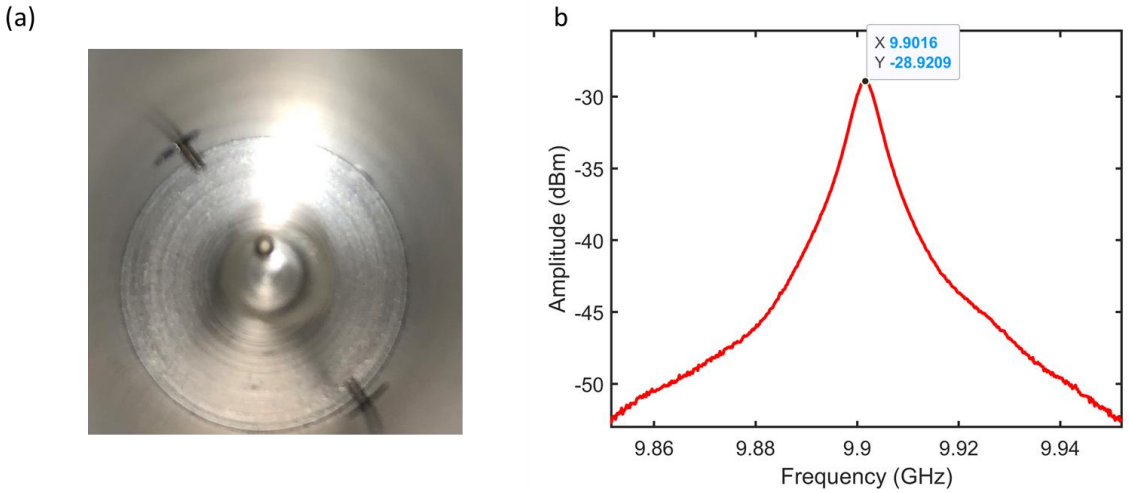


Figure 5.19: (a) Screenshot of a spherical magnet within the cavity ready for the cooldown, (b) microwave spectra of the cavity-magnet system taken at 50 K.

The experimental result of frequency shift as a function of temperature is shown in Figure 5.20. To take the data in a controlled manner. The fridge is let to reach its base temperature first. Then it is heated up approximately by 20-30 mK temperature steps to 950 mK. The same procedure is followed during the cool down. In the experiment, the spectra are taken during the heating and cooling of the fridge. The maximum frequency is extracted from the spectra and is subtracted to the empty cavity resonance frequency.

During the heating up of the cavity, the transition of the superconductor is seen around 790 mK. The phenomenon is identified by the large frequency downshift of 60 MHz. The continuous downshift of frequency is seen above and below the transition temperature. Furthermore, there was a frequency downshift followed by the large upshift (≈760 mK)

during the cool down. The best explanation for such a frequency change is the magnet pushed towards the edge and then levitated.

The intermediate state in the frequency shift is observed around the transition during the warmup and cool down of the cavity. That strengthens the concept of continuous expulsion of magnetic flux during levitation. Furthermore, as seen in Figure 5.15 for the disc magnet, hysteresis is also observed in this magnet type.

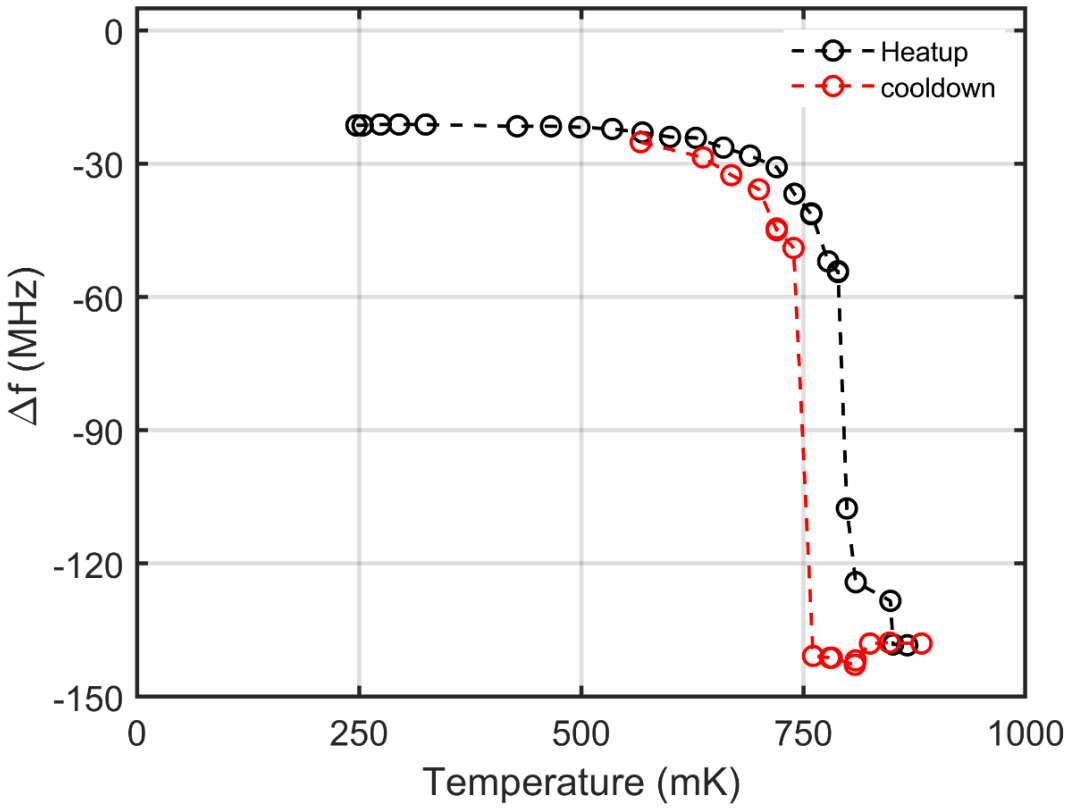


Figure 5.20: The change in resonance frequency of the cavity with an N52 spherical magnet as a function of temperature.

The potential energy landscape is calculated for the spherical magnet within the region above the stub of the cavity in Figure 5.21 using the method described in chapter 4.5.4. Here we assume magnetic moment ($m$) is parallel with the stub. As expected for the large gap cavity, the minimum energy lies at x=2.73 mm and z=1.6 mm away and above from the stub. The minimum energy on the gap explains the push of the magnet during the low temperature. Consequently, the observation frequency downshifts in above Figure 5.20 (see the red trace).

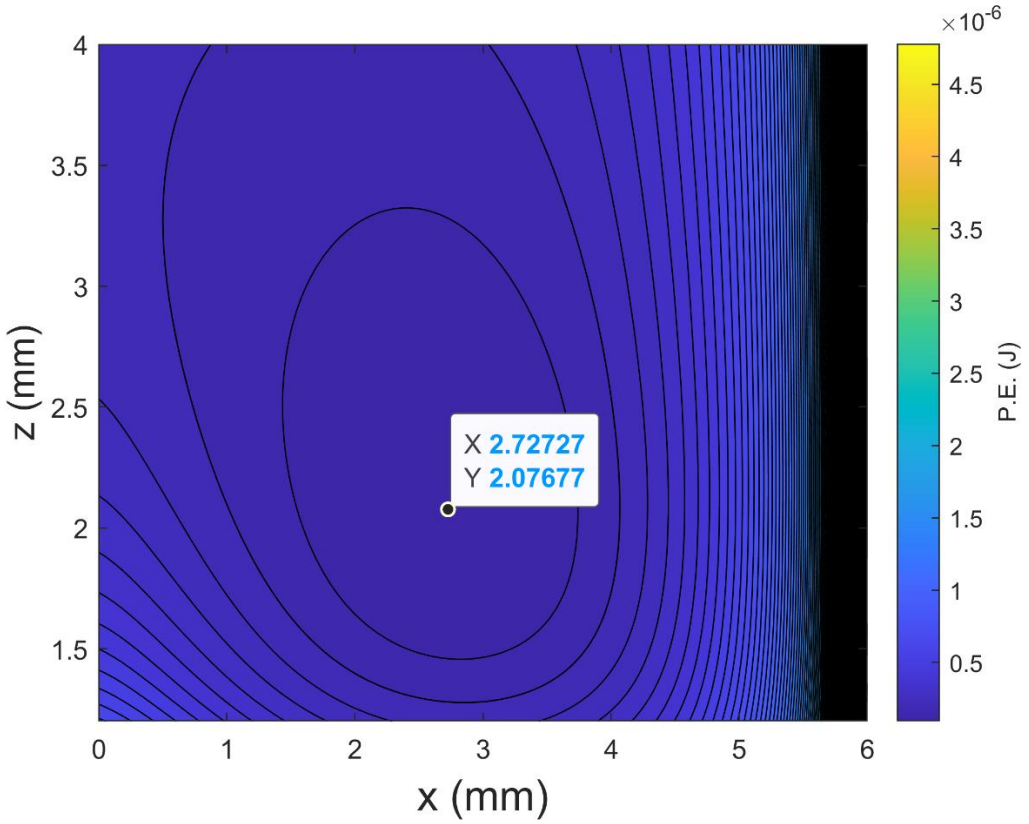


Figure 5.21: Potential energy landscape of the cavity with the spherical magnet, where $m \perp z$. The location of minimum potential on the stub is (x, z= 2.7 mm, 2.1 mm).

With reference to Figure 5.21, the spherical magnet on the stub is pushed only in the two directions when the stub goes into the superconducting state. It will be either moved radially or vertically. Those phenomena will have a drastic opposite frequency shift pattern. The push of the magnet towards the edge will significantly reduce the frequency of the cavity, whereas the vertical displacement shifts up in a large amount.

Figure 5.22 presents the frequency shift for the magnet moving around the stub. The region is the possible place for the magnet to be during the levitation. Since there is no visual access inside the cavity for the low-temperature measurements, comparing the steady-state frequency shift observed in the experiment with the frequency calculated using FEM simulations will give a rough estimation of the levitation location. As shown in Figure 5.20, the steady-state frequency shift is -21.6. When this value is compared with all the results of Figure 5.22, we got x, z= 1.2 mm, 1 mm as the levitation location.

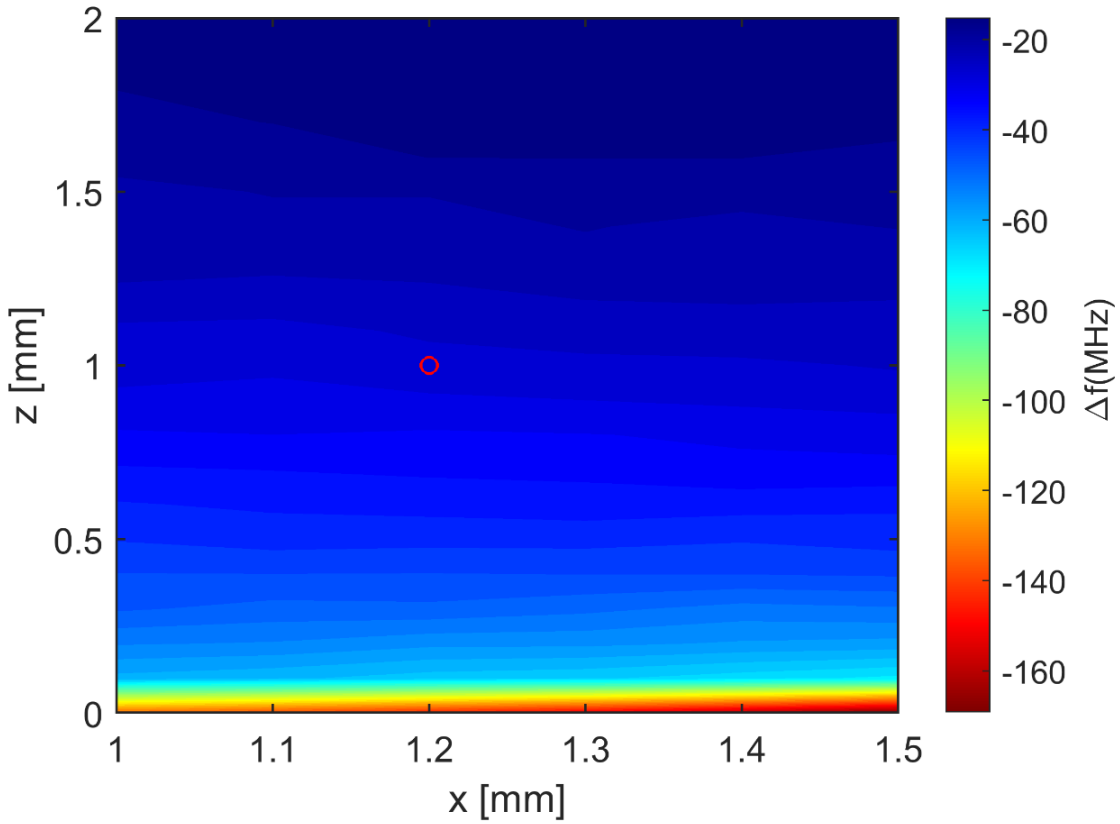


Figure 5.22: Analysis of the frequency change obtained using COMSOL simulations when the magnet is manually placed at different radial and vertical locations on the stub.

## 5.3 Summary

We have experimentally, theoretically, and analytically characterized the levitation of cylindrical, disc, and spherical permanent magnets within a type-1 SRF cavity. We obtain levitation heights of 0.8-1.8 mm for commercially-available neodymium magnets. These levitation heights are in a range where the SRF cavity's resonance frequency varies with magnet position. Levitation temperatures for aluminum cavities range from 100-700 mK, which is obtainable in dilution refrigerator systems. Magnetic levitation is confirmed by the largest shift in the resonance frequency and the sharp rise in the quality factor of the cavity. The experimental results were consistent for multiple heating and cooling cycles of the fridge. Such electro-mechanically coupled systems, if stabilized, can be used to introduce the low-frequency mechanical motion of the magnet with other objects whose quantum states can be probed and manipulated in SRF cavities, such as magnons and transmons [75]. In addition, the levitated high Q mechanical oscillator enables application in ultra-sensing [28,76--79] and gravitational wave detection [80].

# Chapter 6

*"Be stronger than your excuses."*-Bryant McGill

# Outlook

Levitated systems are desirable due to reduced clamping losses and reduced thermal contact. The high Q 3D microwave cavities provide a platform for the coupling of the levitated system. Success coupling opens the path for various fields of research from cavity optomechanical, precision metrology, and even test fundamental physics. Furthermore, similar cavities incorporating Josephson junction qubits are used for quantum information processing, and our work provides the opportunity to include a levitating magnet as a mechanical element within such a system [3], [75].

Our work successfully characterization of magnetic levitation within a microwave cavity. There will be an exciting future project with this system. A few of them will be discussed in this chapter.

## 6.1. Thermally Controlled Magnetic Levitation

One interesting future work would be to study thermally controlled magnetic levitation. The idea here is to ramp up and down the input power, thereby heating and cooling the magnet. One could make a parametric oscillator and sensor by controlling the space between the magnet and superconductor.

Our investigation, shown in Figure 6.1, has shown promising evidence of controlling the distance between the magnet and the superconductor by varying the input power. The power is varied from -5 dBm to 5 dBm at different temperatures during the controlled warm-up of the cavity that is levitated N35 magnet. The red circle on the plot has shown variation in power at that particular temperature. No or small effect is seen during such variation above 700 mK. However, there were 60 MHz of frequency switch 727 mK and 750 mk on such variation. At this temperature, we observed the frequency bounce back as the power was ramped down to its original value (see the onset plots).

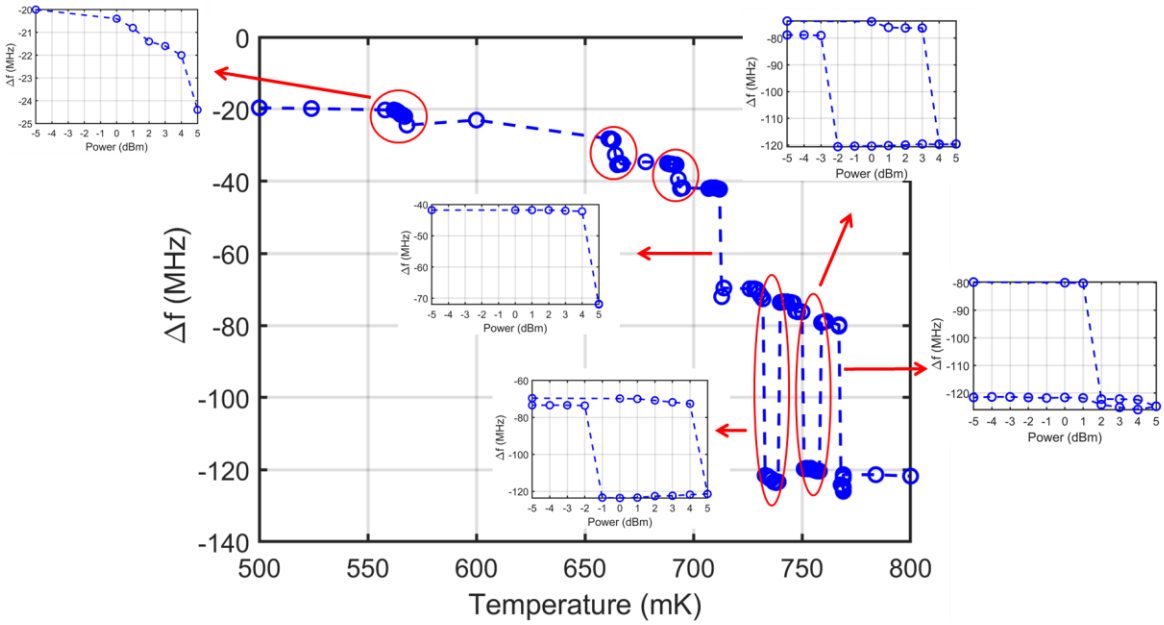


Figure 6.1: Study of control magnetic levitation with the input power. The study is performed at different temperatures during a controlled cavity warm-up with an N35 magnet.

## 6.2. Study of cavity optomechanics

Due to the high mechanical and cavity Q, the cavity optmechanics will be the next promising route of our system. The main limited our system for such study is the limited mechanical and cavity Q. The cavity Q is limited using plastic sleeve to hold the magnet on the stub. Another degradation factor of the Q was extension of the couplers with the body of the cavity to track the spectra on the vector network analysis (VNA). Moreover, the limited resolution of our prevents us to see effect of magnet's motion on the cavity mode.

Upon improving above limitation one can couple and observe cavity opt mechanics in our set up. Figure 6.2 shows screenshot of such coupling. Such a novel macroscopic mechanical system will be capable of sensing and transducing forces, thus allowing for the coupling of disparate classical and quantum systems.

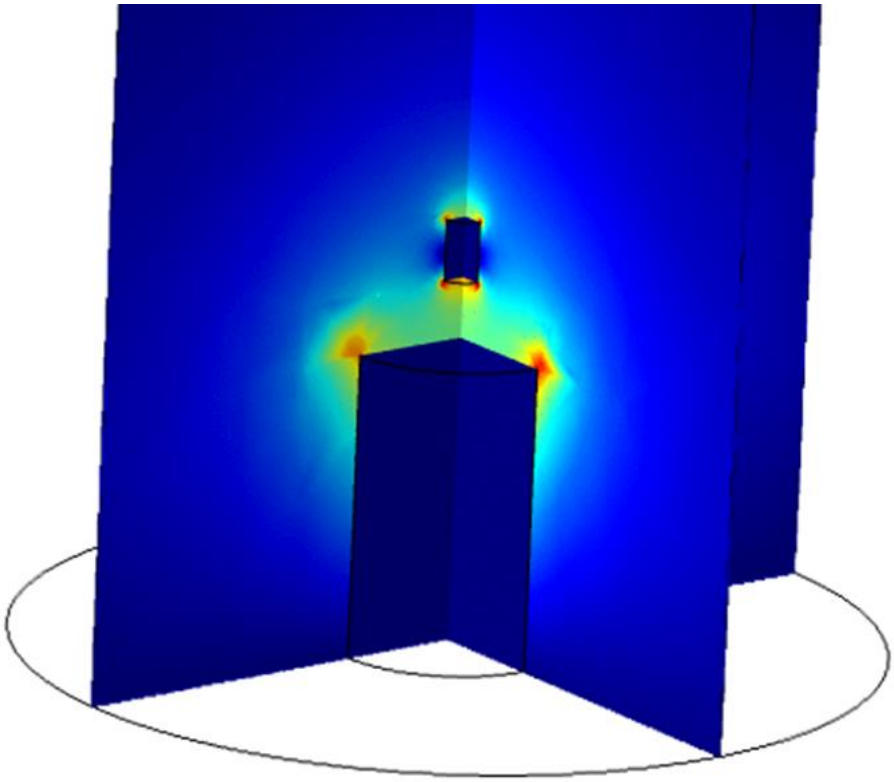

Figure 6.2: A scheme of coupling the mechanical mode with the mode of the cavity.

Bibliography

[1] S. J. Blundell, *Superconductivity: a very short introduction* (OUP Oxford, 2009).

[2] S. Kuhr, S. Gleyzes, C. Guerlin, J. Bernu, U. B. Hoff, S. Deléglise, S. Osnaghi, M. Brune, J. Raimond, and S. Haroche, Appl. Phys. Lett. **90**, 164101 (2007).

[3] M. Reagor, W. Pfaff, C. Axline, R. W. Heeres, N. Ofek, K. Sliwa, E. Holland, C. Wang, J. Blumoff, and K. Chou, Physical Review B **94**, 014506 (2016).

[4] G. Ciovati, P. Dhakal, and A. Gurevich, Appl. Phys. Lett. **104**, 092601 (2014).

[5] N. K. Raut, J. Miller, R. Chiao, and J. E. Sharping, arXiv preprint arXiv:2101.01309 (2021).

[6] N. K. Raut, J. Miller, and J. Sharping, Journal of Institute of Science and Technology **24**, 26 (2019).

[7] J. Sharping, J. Miller, and N. Raut, Bulletin of the American Physical Society (2017).

[8] M. Goryachev, W. M. Campbell, I. S. Heng, S. Galliou, E. N. Ivanov, and M. E. Tobar, arXiv preprint arXiv:2102.05859 (2021).

[9] A. V. Gramolin, D. Aybas, D. Johnson, J. Adam, and A. O. Sushkov, arXiv preprint arXiv:2003.03348 (2020).

[10] S. J. Asztalos, G. Carosi, C. Hagmann, D. Kinion, K. Van Bibber, M. Hotz, L. J. Rosenberg, G. Rybka, J. Hoskins, and J. Hwang, Phys. Rev. Lett. **104**, 041301 (2010).

[11] R. Bradley, J. Clarke, D. Kinion, L. J. Rosenberg, K. van Bibber, S. Matsuki, M. Mück, and P. Sikivie, Reviews of Modern Physics **75**, 777 (2003).

[12] B. T. McAllister, S. R. Parker, and M. E. Tobar, Phys. Rev. Lett. **116**, 161804 (2016).

[13] B. T. McAllister, S. R. Parker, and M. E. Tobar, Physical Review D **94**, 042001 (2016).

[14] M. Aspelmeyer, T. J. Kippenberg, and F. Marquardt, Reviews of Modern Physics **86**, 1391 (2014).

[15] G. Ciovati, *Investigation of the superconducting properties of niobium radio-frequency cavities* (Old Dominion University, 2005).

[16] M. Aspelmeyer, T. J. Kippenberg, and F. Marquardt, Reviews of Modern Physics **86**, 1391 (2014).

[17] V. B. Braginski and A. B. Manukin, Sov.Phys.JETP **25**, 653 (1967).

[18] J. D. Thompson, B. M. Zwickl, A. M. Jayich, F. Marquardt, S. M. Girvin, and J. Harris, Nature **452**, 72 (2008).

[19] A. F. Kockum, A. Miranowicz, S. De Liberato, S. Savasta, and F. Nori, Nature Reviews Physics **1**, 19 (2019).

[20] M. Reagor, W. Pfaff, C. Axline, R. W. Heeres, N. Ofek, K. Sliwa, E. Holland, C. Wang, J. Blumoff, and K. Chou, Physical Review B **94**, 014506 (2016).

[21] K. Cai, P. Parajuli, G. Long, C. W. Wong, and L. Tian, npj Quantum Information **7**, 1 (2021).

[22] A. V. Dixit, S. Chakram, K. He, A. Agrawal, R. K. Naik, D. I. Schuster, and A. Chou, Phys. Rev. Lett. **126**, 141302 (2021).

[23] J. M. Pate, M. Goryachev, R. Y. Chiao, J. E. Sharping, and M. E. Tobar, arXiv preprint arXiv:2004.05983 (2020).

[24] Y. Tabuchi, S. Ishino, A. Noguchi, T. Ishikawa, R. Yamazaki, K. Usami, and Y. Nakamura, Science **349**, 405 (2015).

[25] C. A. Potts and J. P. Davis, Appl. Phys. Lett. **116**, 263503 (2020).

[26] M. Yuan, V. Singh, Y. M. Blanter, and G. A. Steele, Nature communications **6**, 1 (2015).

[27] J. Ahn, Z. Xu, J. Bang, Y. Deng, T. M. Hoang, Q. Han, R. Ma, and T. Li, Phys. Rev. Lett. **121**, 033603 (2018).

[28] J. Ahn, Z. Xu, J. Bang, P. Ju, X. Gao, and T. Li, Nature Nanotechnology **15**, 89 (2020).

[29] T. M. Hoang, Y. Ma, J. Ahn, J. Bang, F. Robicheaux, Z. Yin, and T. Li, Phys. Rev. Lett. **117**, 123604 (2016).

[30] S. J. Blundell, *Superconductivity: a very short introduction* (OUP Oxford, 2009).

[31] J. Gieseler, A. Kabcenell, E. Rosenfeld, J. D. Schaefer, A. Safira, M. J. Schuetz, C. Gonzalez-Ballestero, C. C. Rusconi, O. Romero-Isart, and M. D. Lukin, Phys. Rev. Lett. **124**, 163604 (2020).

[32] C. Timberlake, A. Vinante, F. Shankar, A. Lapi, and H. Ulbricht, Physical Review D **104** (2021).

[33] D. M. Pozar, *Microwave engineering* (John wiley & sons, 2011).

[34] J. M. Pate, L. A. Martinez, J. J. Thompson, R. Y. Chiao, and J. E. Sharping, AIP Advances **8**, 115223 (2018).

[35] *https://doc.comsol.com/5.4/doc/com.comsol.help.rf/RFModuleUsersGuide.pdf*.

[36] B. T. McAllister, Y. Shen, G. Flower, S. R. Parker, and M. E. Tobar, J. Appl. Phys. **122**, 144501 (2017).

[37] B. T. McAllister and M. E. Tobar, J. Appl. Phys. **123**, 226102 (2018).

[38] J. J. Barroso, P. J. Castro, J. P. L. Neto, and O. D. Aguiar, Int J Infrared Millim Waves **26**, 1071 (2005).

[39] D. Kajfez and P. Guillon, Atlanta: Noble Publishing Corporation (1998).

[40] J. M. Pate, *Tunable Microwave Cavities for Macroscopic Cavity Optomechanics* (University of California, Merced, 2020).

[41] J. E. Sharping, J. Pate, J. Parker, J. J. Thompson, L. A. Martinez, A. R. Castelli, and R. Y. Chiao, Journal of applied physics **128**, 73906 (2020).

[42] M. Tinkham, *Introduction to superconductivity* (Courier Corporation, 2004).

[43] J. B. (. Ketterson and S. N. (. Song, *Superconductivity* (Cambridge University Press, Cambridge, 1999).

[44] P. De Gennes, *Superconductivity of metals and alloys* (CRC Press, 2018).

[45] J. F. Annett, *Superconductivity, superfluids and condensates* (Oxford Univ. Press, 2004).

[46] J. M. Ziman, *Principles of the Theory of Solids* (Cambridge university press, 1972).

[47] J. F. Annett, *Superconductivity, superfluids and condensates* (Oxford University Press, 2004), 5.

[48] Poole,Charles P.,,Jr, H. A. Farach, R. J. Creswick, and R. Prozorov, *Superconductivity* (Elsevier Science & Technology, San Diego, 2007).

[49] J. M. (. Ziman, *Principles of the theory of solids* (Cambridge University Press, Cambridge England] ;, 1979).

[50] V. V. Schmidt, *The Physics of Superconductors : Introduction to Fundamentals and Applications*, edited by P. Müller and A. V. Ustinov (Springer Berlin / Heidelberg, Berlin, Heidelberg, 1997).

[51] W. Buckel and R. Kleiner, *Superconductivity : fundamentals and applications* (Wiley-VCH, Weinheim, 2004).

[52] G. Ciovati, *Investigation of the superconducting properties of niobium radio-frequency cavities* (Old Dominion University, 2005).

[53] J. Bardeen, L. N. Cooper, and J. R. Schrieffer, Physical review **108**, 1175 (1957).

[54] *K&J Magnets*.

[55] N. Derby and S. Olbert, American Journal of Physics **78**, 229 (2010).

[56] C. A. Potts and J. P. Davis, arXiv preprint arXiv:2006.01223 (2020).

[57] N. Raut, J. Miller, J. Pate, R. Chiao, and J. Sharping, IEEE Trans. Appl. Supercond. (2021).

[58] F. Hellman, E. M. Gyorgy, D. W. Johnson Jr, H. M. O'Bryan, and R. C. Sherwood, J. Appl. Phys. **63**, 447 (1988).

[59] H. Padamsee, J. Knobloch, and T. Hays, Inc., New York, 199 (1998).

[60] K. Fujisawa, IRE transactions on microwave theory and techniques **6**, 344 (1958).

[61] J. Lugo and V. Sosa, Physica C: Superconductivity **324**, 9 (1999).

[62] H. M. Al-Khateeb, M. K. Alqadi, F. Y. Alzoubi, and N. Y. Ayoub, Journal of superconductivity and novel magnetism **21**, 93 (2008).

[63] D. J. Griffiths and D. F. Schroeter, *Introduction to quantum mechanics* (Cambridge university press, 2018).

[64] A. A. Kordyuk, J. Appl. Phys. **83**, 610 (1998).

[65] J. Miller, N. Raut, D. Zulevic, R. Chiao, and J. Sharping, Bulletin of the American Physical Society (2022).

[66] N. Raut, J. Miller, R. Chiao, and J. Sharping, Bulletin of the American Physical Society (2022).

[67] N. Raut, J. Miller, J. Pate, R. Chiao, and J. Sharping, Bulletin of the American Physical Society **66** (2021).

[68] Y. Tabuchi, S. Ishino, A. Noguchi, T. Ishikawa, R. Yamazaki, K. Usami, and Y. Nakamura, Science **349**, 405 (2015).

[69] B. T. McAllister, J. Bourhill, W. H. J. Ma, T. Sercombe, M. Goryachev, and M. E. Tobar, IEEE Transactions on Instrumentation and Measurement **70**, 1 (2020).

[70] G. Flower, B. McAllister, M. Goryachev, and M. E. Tobar, Appl. Phys. Lett. **117**, 162401 (2020).

[71] M. Fox, *Quantum optics: an introduction* (OUP Oxford, 2006), 15.

[72] D. L. Creedon, M. Goryachev, N. Kostylev, T. B. Sercombe, and M. E. Tobar, Appl. Phys. Lett. **109**, 032601 (2016).

[73] K. Kim, E. Levi, Z. Zabar, and L. Birenbaum, IEEE Trans. Magn. **32**, 478 (1996).

[74] M. D. Simon, L. O. Heflinger, and A. K. Geim, American journal of physics **69**, 702 (2001).

[75] J. Gieseler, A. Kabcenell, E. Rosenfeld, J. D. Schaefer, A. Safira, M. J. Schuetz, C. Gonzalez-Ballestero, C. C. Rusconi, O. Romero-Isart, and M. D. Lukin, Phys. Rev. Lett. **124**, 163604 (2020).

[76] M. Rademacher, J. Millen, and Y. L. Li, arXiv preprint arXiv:2005.14642 (2020).

[77] D. Hempston, J. Vovrosh, M. Toroš, G. Winstone, M. Rashid, and H. Ulbricht, Appl. Phys. Lett. **111**, 133111 (2017).

[78] S. Kolkowitz, A. C. B. Jayich, Q. P. Unterreithmeier, S. D. Bennett, P. Rabl, J. Harris, and M. D. Lukin, Science **335**, 1603 (2012).

[79] M. Rashid, M. Toroš, A. Setter, and H. Ulbricht, Phys. Rev. Lett. **121**, 253601 (2018).

[80] W. A. Prothero Jr and J. M. Goodkind, Rev. Sci. Instrum. **39**, 1257 (1968).